3-2020

CN and C$_2$ Spectroscopy on the Pulsed Ablation of Graphite in the Visible Spectrum

Brandon A. Pierce

**CN and C$_2$ Spectroscopy on Pulsed Laser
Ablation of Graphite in the Visible Spectrum**

THESIS

Brandon A. Pierce, 2d Lt, USAF

AFIT-ENP-MS-20-M-111

DEPARTMENT OF THE AIR FORCE
AIR UNIVERSITY

AIR FORCE INSTITUTE OF TECHNOLOGY

Wright–Patterson Air Force Base, Ohio

DISTRIBUTION STATEMENT A
APPROVED FOR PUBLIC RELEASE; DISTRIBUTION UNLIMITED.

The views expressed in this document are those of the author and do not reflect the official policy or position of the United States Air Force, the United States Department of Defense or the United States Government. This material is declared a work of the U.S. Government and is not subject to copyright protection in the United States.

AFIT-ENP-MS-20-M-111

CN AND C$_2$ SPECTROSCOPY ON PULSED LASER ABLATION OF

GRAPHITE IN THE VISIBLE SECTRUM

THESIS

Presented to the Faculty

Department of Engineering Physics

Graduate School of Engineering and Management

Air Force Institute of Technology

Air University

Air Education and Training Command

in Partial Fulfillment of the Requirements for the

Degree of Master of Science in Applied Physics

Brandon A. Pierce, B.S. Physics

2d Lt, USAF

March 6, 2020

CN AND C$_2$ SPECTROSCOPY ON PULSED LASER ABLATION OF

GRAPHITE IN THE VISIBLE SECTRUM

THESIS

Brandon A. Pierce, B.S. Physics
2d Lt, USAF

Committee Membership:

Dr. Kevin C. Gross
Chair

Dr. Glen P. Perram
Member

Dr. Christopher A. Rice
Member

Abstract

An experimental study was conducted on the pulsed laser ablation of graphite. Optical emissions spectroscopy and gated ICCD imagery were used to characterize the plume dynamics, which are important for laser weapon effects with the increase in variety of tactical missions for laser weapons systems. The dynamics of the graphite ablation have been studied extensively; however, the lack of agreement on the mechanisms warrants further investigation. This research was intended to gain a deeper understanding of the fundamental mechanisms driving these processes.

The shock fronts were analyzed using the ICCD gated imagery with various filters to limit the species being investigated. Initial shock front velocities were on average 1.46 cm/μs using the drag model to fit the shock fronts. The stopping distance of the drag model varied from 0.5 cm to 1.6 cm based on background gas and pressure. Lowering the background pressure by a factor of 10 tripled the stopping distance and increased the initial velocity by 20%. The Taylor-Sedov model was also fit to the shock fronts and yielded on average an $n = 1.74$, suggesting the shock front expansion is between the plane wave ($n = 1$) and cylindrical wave ($n = 2$) limits.

Graphite samples were irradiated with 151 MW/cm^2 and a fluence of 3.8 J/cm^2 using a pulsed KrF 248 nm laser with a pulse width of 25 ns. Optical emission spectroscopy showed the C$_2$ Swan $\Delta v = 0, \pm 1, \pm 2$ sequences and the CN Violet $\Delta v = 0, +1$ sequences. Spectroscopic models were developed to extract the rovibrational temperatures of each molecule for $t = 0 - 10$ μs after laser irradiation in a variety of background gases. The background gases used were Air, Ar, He, and N$_2$ at 10 Torr and also at 1 Torr for N$_2$. For the C$_2$ Swan band, the temperatures ranged between $T_R = 3,700 - 6,000$ K and $T_v = 3,000 - 7,000$ K, respectively. The rotational and

vibrational temperatures for the CN Violet ranged between $T_R = 3,500 - 6,000 K$ and $T_v = 7,000 - 12,000$ K, respectively. The rovibrational temperatures were found to vary with background pressure for the CN Violet system, but not for the C_2 Swan. In general, the rotational temperatures, T_R, and the vibrational temperatures, T_v, were not in equilibrium.

To my wife

Table of Contents

List of Figures

ix

x

xi

List of Tables

CN AND C$_2$ SPECTROSCOPY ON PULSED LASER ABLATION OF GRAPHITE IN THE VISIBLE SECTRUM

I. Introduction

Studying the pulsed laser ablation (PLA) of graphite has multiple important Department of Defense (DoD) applications as well as scientific and industrial applications. The increased variety of tactial missions for laser weapons systems is driving a need in the Department of Defense for understanding a variety of laser-material interactions [1]. Carbon is a particularly important material due to the use of carbon fibers and other carbon based materials in many aerospace systems. Understanding the PLA of graphite will serve as the foundation for understanding more complex carbon based materials. The spectroscopy of the resulting plume is also a high interest area for the DoD due its applicability to the hypersonic community because the radiometric signatures of hypersonics are difficult to simulate in the lab environment [2]. However, the PLA of graphite results in high mach numbers which can be used to study the chemistry in the boundary layer of ablated carbon and background gas, which is also important for thermal protection system design.

A historical review of the mechanisms and processes governing the pulsed laser ablation of graphite as well as the resulting plume will show that there are inconsistent results. Most of the research in this area came from a materials processing standpoint. Many laser based materials processing applications such as coating and thin film deposition [3, 4] and synthesizing nanoparticles and nanostructures [5–7] are driven by the process of ablation. The research helped the industry become more predictive in the processes used to make these various materials [8,9]. However, the fundamental

1

underlying processes were discussed much less. The purpose of this research is to use the plume dynamics and optical emissions spectroscopy (OES) in order to inform on some of the mechanisms driving the pulsed ablation of graphite in the pulsed laser nanosecond regime.

Chapter II of this work will outline a few fundamental principles to shed light on the processes governing the pulsed ablation of graphite in the nanosecond time domain. Diatomic spectroscopy for C_2 and CN as well as shock modeling for plumes will also be detailed here.

Chapter III of this study describes the experiment that was done to obtain the optical emission spectra and gated ICCD images. The models developed in PGO-PHER to simulation the rovibrational temperatures of the species in the plume are also detailed here.

Chapter IV of this study discusses the results of the simulations as well as the shock front model results. The rovibrational temperatures as well as the intensities of various species in the plume are discussed. The results from fitting the Taylor-Sedov mode and the drag model to the shock front data is also presented here.

II. Background

Studying the pulsed laser ablation of graphite requires almost every foundational piece of physics, which is in some ways its beauty. An understanding of optics is required to focus the laser onto the material. The energy transfer into the material requires knowledge of materials science. The laser interaction with the surface as well as the resulting plasma is governed by electrodynamics. The rich spectroscopy is governed by quantum mechanics and statistical mechanics. The propagation of the plume can be partially understood with dynamics. The goal of this background section is to give a glimpse into each complexity that arises when attempting to understand the PLA of graphite. In Section 2.1, the laser material interaction will be discussed along with various properties of graphite. Section 2.2 discusses how the plume propagates into the background medium. Section 2.3 discusses diatomic spectroscopy and some of the notation associated with the field.

2.1   Laser Material Interactions

Clearly one of the greatest innovations in modern history, the laser has continued to have new applications since its inception. The theory was first developed by Einstein in 1917 [10]. Forty years later, Maiman developed the first pulsed laser [11]. Since then, the laser, both continuous and pulsed varients, has continued to be used in a plethora of domains.

It did not take long before pulsed lasers were used for material removal. Pulsed laser ablation is the material removal process for nanosecond and pico-/ femtosecond lasers. It is has a variety of applications including cleaning surfaces (such as artwork) from particultes [12,13], various surgical/medical procedures [14–16], micropatterning of materials [17], chemical analysis (such as Laser Induced Breakdown

3

Spectroscopy (LIBS) or Laser Ablation Molecular Isotopic Spectrometry (LAMIS)), and the deposition of thin films [4, 6, 7, 18]. The pulsed laser ablation of graphite has been extensively studied for various applications; however, pulsed laser deposition (PLD) is often the main area of focus when graphite is involved in order to create various thin films such as diamond-like carbon (DLC) films. The laser material interactions vary significantly based on pulse duration, but for this thesis, the focus will be on nanosecond pulse widths.

When the laser beam reaches the surface of the solid before the plume is ejected, a portion is reflected due to the discontinuity in the index of refraction, while the rest is transmitted into the material. The portion reflected on the surface depends on the polarization and the angle of incidence (The reflection coefficients can be calculated from the standard Fresnel equations [19]). These coefficients depend on surface properties such as smoothness and level of surface oxidation, which can give a range of values. Once in the material, the Beer-Lambert law governs light absoprtion

$$I(z) = I_0 e^{-\alpha z} \tag{1}$$

where I_0 is the intensity just inside the surface, z is the depth, and α is the material's absorption coefficient. This assumes a constant α, but α is typically a function of wavelength and temperature. The absorption coefficient of bulk graphite (Goodfellow, 99.95% purity, pressed from 1–5 lm size crystalline grains) was studied under various conditions including pulsed laser heating and was found to be 15.27 μm^{-1} [20]. A convenient optical parameter to define is the optical absorption or penetration depth, $l_\alpha = 1/\alpha$ [21]. The optical absorption depth is the depth where the intensity drops to $1/e$ (the e-folding length) of its initial value. In the case of graphite at a 248 nm wavelength, $l_\alpha = 1/15.27 = 0.0655$ microns.

In the nanosecond region of pulsed ablation, the laser pulse duration is much longer

4

than the lattice heating time. The thermal properties of the material are therefore important because the material is heated as the laser energy is absorbed. The thermal properties are described by the specific heat per unit mass C_P, the density ρ, and the thermal conductivity κ. For the graphite targets, $\kappa = 140$ W/m K [22]. The heat diffusivity is then defined as $D = \frac{\kappa}{C_P \rho}$ [21], and a characteristic length for heat diffusion can be defined as

$$l_D \approx 2\sqrt{D\tau_p} \qquad (2)$$

where τ_p is the laser pulse duration. The characteristic length describes how much the heat traverses through the material during the laser irradiation. At a temperature of 3500 K, the specfic heat graphite is $C_P = 2135$ J/kg K [23]. With these parameters and a theoretical density of 2250 kg/m^3 [22], the diffusivity is aproximately $D = 2.91 \times 10^{-5}$ m^2/s. The theoretical density is used because the actual density can vary a large amount as shown by Bauer [24]. In fact, most of these material properties vary widely due to porosity and how the graphite was actually manufactured. These values are used to give an estimate. Thus, the characteristic length is $l_D = 1.71$ μm assuming a pulse width of $\tau_p = 25$ ns. For graphite, the phase transition skips the liquid phase and sublimates directly to the gas phase. ΔH_s describes the enthalpy of sublimation, where the energy becomes large enough such that the solid transitions directly from a solid to a vapor. Sublimation is often observed in the pulsed laser ablation of graphite [25]. The enthalpy of sublimation for graphite at $T = 2500$ K is approximately $\Delta H_s = 176$ kcal/mol or 736.4 kJ/mol [26]. The temperature of sublimation for graphite at 1 atm is approximately 3958 K [27]. Table 1 summarizes all of these constants for graphite.

Because the lattice has time to transfer heat, the laser energy is deposited into the region dependent on l_D. Knowing this, an estimated threshold fluence can be

5

Table 1. Various pertinent material properties of graphite

Graphite Material Parameters			
α ($\mu\mathrm{m}^{-1}$)	15.27 [20]	D (m^2/s)	2.91×10^{-5}
l_α (μm)	0.0655	l_D (μm)	1.71
κ (W/m K)	140 [22]	τ_p (ns)	25
C_P (J/kg K) (at T=3500 K)	2135 [23]	T_S (K)	3958 [27]
ρ (kg/m^3)	2250 [22]	ΔH_s (kJ/mol)	736.4 [26]

calculated,

$$F_{th} = \rho H_s l_D \tag{3}$$

where $\rho(\mathrm{g/cm}^3)$ is the density of the material, $H_s(\mathrm{J/g})$ is the heat of sublimation, and $l_D(\mathrm{cm})$ is the diffusion length. A zeroth order assumption would be the ablated mass can be calculated from the volume described by the laser spot size and the diffusion length, l_D. Because the laser spot size is much larger than the diffusion length, there is no transverse heat flow. However, it is known that material redeposition is very common in nanosecond pulsed ablation [18]. Another way to estimate it is using the imagery data. Section 2.2 will detail the plume dynamics; however, this calculation only requires knowing the initial expansion velocity of the plume. Knowing that will yield an estimate for the kinetic energy per particle. Using that and the heat of sublimation can give at least an upper bound on the ablated mass, m_a,

$$m_a = \frac{E_p}{\frac{1}{2}mv_i^2 + H_s}\frac{M}{N_A} \tag{4}$$

where E_p is the energy per pulse of the laser, m is the mass of the particle (i.e. a carbon atom), v_i is the initial plume velocity, H_s is the heat of sublimation in units of energy per particle, N_A is avogadro's number, and M is the Molar mass.

2.2 Plume Dynamics

As the plume is forming, the laser is still on, and an additional high-pressure region is developed from the plume excitation by the laser. Singh describes the dynamics first as a plasma formation, heating, and inital three dimensional isothermal expansion, which is then followed by adiabatic expansion after the laser has terminated [3]. As the plume is expanding into the background gas, a shock front forms. There are various shock models that can be used. One of which is known as the Taylor-Sedov model, which states the position of a shock front can be calculated from [28]

$$R(t) = \xi \Big(\frac{E}{\rho_b}\Big)^{\frac{1}{n+2}} t^{\frac{2}{n+2}} \tag{5}$$

where t is the time delay, ρ_b is the background gas density, E is the energy released during the blast, and ξ is a constant which depends on the specific heat capacity ratio ($\xi = 1.49$ ($n = 1$), $\xi = 1.77$ ($n = 2$), $\xi = 1.15$ ($n = 3$)) [29]. The value of n is either 3, 2, or 1 for spherical, cylindrical, or plane wave shock propagation. In general, Eq. 5 can be fit using the functional form $R(t) = at^b$. Previous research has shown good agreement with shock fronts resulting from pulsed laser ablation [28]. The Taylor-Sedov model is typically valid in the mid-field limit. This occurs when the ablated mass is less than the amount of mass displaced by the expanding shock and when the pressure of the background gas is less than the pressure behind the shock front [29]. This can be captured consisely with the following limits,

$$z_L = \Big(\frac{3m_a}{2\pi\rho}\Big)^{1/3} \ll z \ll \Big(\frac{2E_p}{P_b}\Big)^{1/3} = z_H \tag{6}$$

where m_a is the ablated mass, ρ is the background gas density, E_p is the laser energy of a pulse, and P_b is the background gas pressure.

Another model that can be used to describe the shock front is the drag model.

The drag model states the position of the shock front is described by

$$R(t) = R_s(1 - e^{-kt}) \tag{7}$$

where R_s is the stopping distance and k is the slowing coefficient. It predicts the plume will come to a halt due to collisions with the background gas at some stopping distance. Consider the derivate at $t = 0$ for the drag model,

$$\left.\frac{dR}{dt}\right|_{t=0} = v_0 = kR_s e^{-kt}\big|_{t=0}$$
$$= kR_s.$$

Thus, fitting to this model yields an estimate of the initial free streaming velocity. Velocities on the order of 1 cm/μs are fairly typical [18, 30, 31].

2.3 Diatomic Spectroscopy

The following section details a review of the basic molecular spectroscopy of C_2 and CN. Term symbols, which are a schema for effectively naming states in an organized fashion. Electronic states for diatomic atoms can be described by the term symbol $^{2S+1}\Lambda_{\Omega,(g/u)}^{(+/-)}$ where S is the total spin quantum number, Λ is the projection of the orbital angular momentum onto the internuclear axis ($\Lambda = \sum \lambda_i$), Ω is the projection of the total angular momentum onto the internuclear axis, g/u is the parity (for homonuclear diatomics), and $+/-$ is the reflection symmetry. Figure 1 details the various angular momentum for a diatomic molecule and shows the projections that are included in the term symbols. The selection rules for allowed transitions are as follows: $\Delta\Lambda = 0, \pm 1$, $\Delta S = 0$, $\Delta\Sigma = 0$ (for Hund's case (a)), $\Delta\Omega = 0, \pm 1$, $g \leftrightarrow u$, and $+ \leftrightarrow +(- \leftrightarrow -)$ [32]. The energy levels are described by a combination of electronic,

8
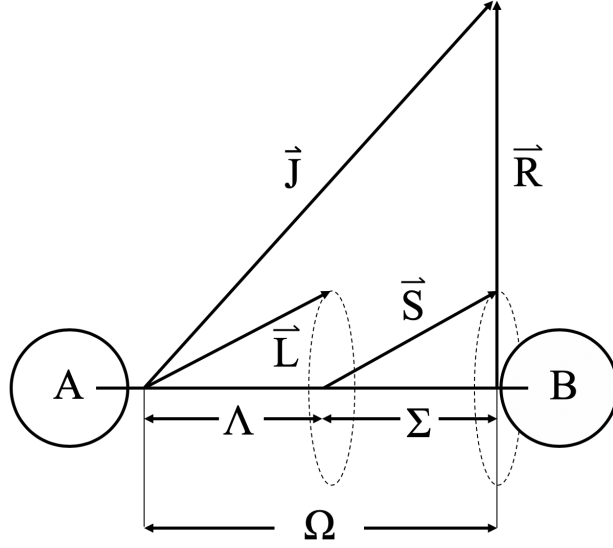
Figure 1. Diagram of the angular momenta present in a diatomic molecule for a Hund's case (a). (Recreated from [32])

vibrational and rotational in the following manner

$$E = T_e + G(v) + F_v(J) \tag{8}$$

where T_e is the electronic energy (the potential minimum), $G(v)$ is the vibrational energy, and $F_v(J)$ is the rotational energy. Each electronic transition is composed of vibrational bands. These vibrational bands are then made up of rotational lines. T_e is simply the energy at $v = 0$ state for a given electronic energy level. The vibrational energy for a particular v is the usual expression [33]

$$G(v) = \omega_e(v + \frac{1}{2}) - \omega_e x_e(v + \frac{1}{2})^2 + \omega_e y_e(v + \frac{1}{2})^3 + ... \tag{9}$$

The vibrational bands with the same Δv form a sequence (i.e., the $\Delta v = 0$ sequence is composed of the 0–0, 1–1, 2–2,... bands). A series of bands that share a similar vibrational level (1–1, 1–2, 1–3, ...) is called a progression. The intensities for different vibrational bands depends upon the strength of the electronic transition,

9

the population in the vibrational levels, and the Franck-Condon factor, which is the squared overlap integral of the two vibrational wavefunctions. Of course, this neglects the rotational structure, but the rotational structure can vary based up what type of transition is occuring.

In the most general case, a non-rigid, vibrating symmetric top can be used to give an equation for the rotational energy:

$$F_v(J) = B_v J(J + 1) - D_v J^2(J + 1)^2 + ... \tag{10}$$

where B_v is the rotational constant for a given vibrational level and D_v is the centrifugal term [33]. It is worth noting that the convention of Herzberg is followed here where the $(A - B_v)\Lambda^2$ term is neglected because it is a constant for a given vibrational level and can thus be included in the band origin [33]. The rotational constant is defined as

$$B_v = B_e - \alpha_e(v + \frac{1}{2}) + \gamma_e(v + \frac{1}{2})^2 + \delta_e(v + \frac{1}{2})^3 + ... \tag{11}$$

The selection rules for allowed rotational transitions are $\Delta J = 0, \pm 1$ ($\Delta J = 0$ is forbidden if $\Lambda = 0$ for both electronic states) [33]. There are thus typically three branches associated with each vibrational transition: the P branch ($\Delta J = -1$), the Q branch ($\Delta J = 0$), and the R branch ($\Delta J = +1$). More specifically, we'll deal with the rotational structure for each transition that is studied during the experiment, namely the C_2 Swan bands ($d^3\Pi_g$ - $a^3\Pi_u$) and the CN violet ($B^2\Sigma^+$–$X^2\Sigma^+$). The rotational structure will depend on how the various angular momenta are coupled together. Hund's cases are used to describe the ways in which different angular momenta in the molecule couple. There are various cases denoted Hund's case (a), case (b), case (c), case (d), and case (e). For the purposes of this thesis, Hund's

10
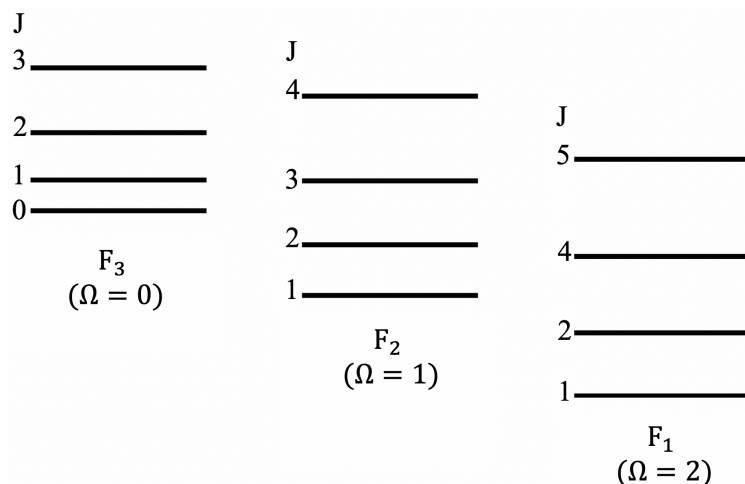
Figure 2. **Energy Level Diagram for** $a^3\Pi_u$ **state of** C_2 **depicting a Hund's case (a) example. (Not to Scale) (Adapted from [34])**

case (a) and case (b) are the only two that need to be discussed in detail. Hund's case (a) is a case in which the electronic motion ($\mathbf{S}$ and $\mathbf{L}$) is coupled strongly to the nuclear axis, but the interaction of the nuclear rotation with the electronic motion is weak [33]. Thus, Λ, Σ and Ω are good quantum numbers. $\boldsymbol{\Omega}$ and the nuclear rotation vector, $\mathbf{R}$, couple to give $\mathbf{J}$. A good example of this is the $a^3\Pi_u$ state of C_2, which is Hund's case (a) at low J [34]. With $\Lambda = \pm 1$ and $\Sigma = -1$, 0, or $+1$, the values of $|\Omega|$ can be 0, 1, or 2. The resulting states are $^3\Pi_0$, $^3\Pi_1$, and $^3\Pi_2$. A qualitative energy level diagram for this is shown in Figure 2. For a case (a) state, the levels are best described as being split into Ω components with a progression of J values within each component.

For Hund's case (b), the electron spin $\mathbf{S}$ is not coupled to the internuclear axis at all, which means $\boldsymbol{\Omega}$ is not well defined. The angular momenta $\boldsymbol{\Lambda}$ and $\mathbf{R}$ combine to form $\mathbf{N}$, and N is a good quantum number. Then, $\mathbf{N}$ combines with $\mathbf{S}$ to form $\mathbf{J}$ as shown in Figure 3. The energy levels are affected by the value of N the most. Then, they split slightly into spin components. An example of Hund's case (b) is the CN $B^2\Sigma^+$ state, and its energy levels are shown in Figure 4.

11
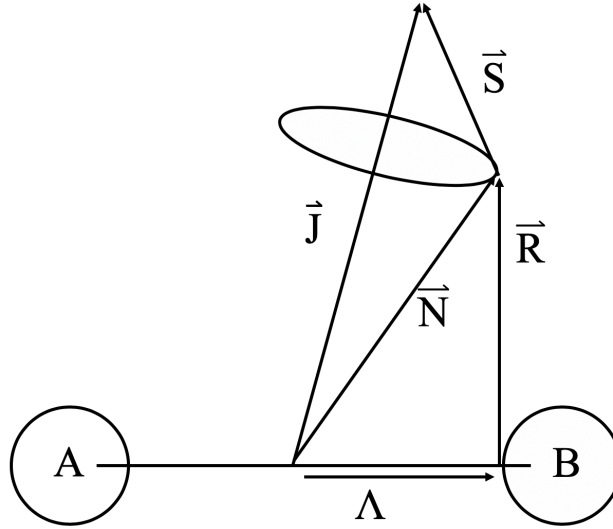
Figure 3. Vector diagram of the angular momenta present in a diatomic molecule for a Hund's case (b). (Adapted from [33])

It is well known that the PLA of graphite produces the molecular species C_2. The most common observed transitions for C_2 during PLA of graphite are from the Swan system, which involves the electronic transition $d^3\Pi_g$ – $a^3\Pi_u$ [35–38]. This system, named after William Swan, is particularly important in astronomy, materials science, and combustion science [39]. The swan system has been observed in comets, the Sun, carbon stars, K-, M-, and S-type stars, brown dwars and even extrasolar planets [41–45]. In the material science domain, the C_2 Swan system is often used as a diagnostic for the production of carbon nanotubes as well as thin film productions [4, 6, 7, 46, 47]. The Swan system is also used in combustion science because it found in flames. It helps in studying various hydrocarbon flames and modeling processes [48–50]. The $d^3\Pi_g$ electronic state is located 19,378.5 cm^{-1} above the $a^3\Pi_u$ state as shown in Figure 5. The upper electronic state has a smaller equilibrium internuclear distance than the lower state as shown in Table 2, which details all the equilibrium constants for the upper and lower states. Thus, we can expect band heading to occur in the P branch.

12
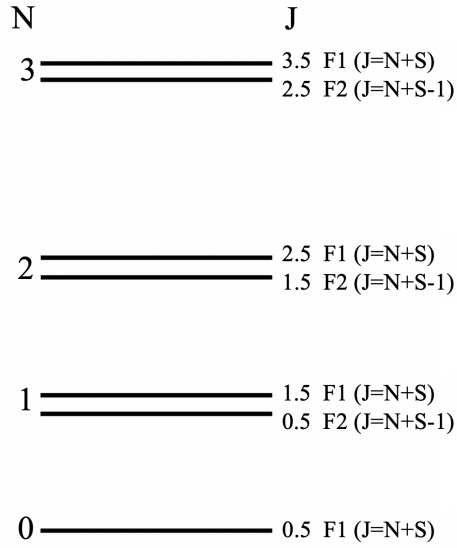
Figure 4. Energy Level Diagram for $B^2\Sigma^+$ state of CN depicting a Hund's case (b) example. (Not to scale) (Adapted from [34])

Figure 5. Potential energy surfaces for the $a^3\Pi_u$ and $d^3\Pi_g$ electronic states of C_2. The $v = 0 - 2$ vibrational states are shown for each state. (Adapted from [40])

There are also transitions that occur from the emission of CN in the UV-VIS-NIR. In the PLA of graphite, the most commonly observed transition is the CN Violet

Table 2. Equilibrium constants (in cm^{-1}) for a$^3\Pi_u$ and d$^3\Pi_g$ states of C$_2$. (Adapted from [51])

Spectroscopic Constants	$a^3\Pi_u$	$d^3\Pi_g$
T_e................................	...	19378.46446(30)
ω_e	1641.341(23)	1789.094(21)
$\omega_e x_e$	11.6580(58)	17.367(15)
$\omega_e y_e$	-0.00083(41)	-0.1360(36)
$\omega_e z_e$	...	-0.04878(25)
B_e	1.63235(4)	1.75542(9)
α_e	0.01657(3)	0.0196(1)
γ_e	-0.000027(5)	-0.00013(4)
δ_e	...	-0.000082(3)
$r_e(\mathring{A})$	1.311946(16)	1.265122(32)

Table 3. Equilibrium constants (in cm^{-1}) for X$^2\Sigma^+$ and B$^2\Sigma^+$ states of CN. (Adapted from [52])

Spectroscopic Constants	$X^2\Sigma^+$	$B^2\Sigma^+$
T_e.................................	...	25752.590(12)
ω_e.................................	2068.68325(99)	2162.223(30)
$\omega_e x_e$..............................	13.12156(45)	19.006(22)
$\omega_e y_e$..............................	-0.005426(74)	-0.1346(65)
$\omega_e z_e$..............................	-9.82(40)E-5	-0.03673(85)
$\omega_e \eta_e$..............................	...	0.001430(37)
B_e.................................	1.8997872(28)	1.96797(41)
α_e.................................	-0.0173802(27)	-0.01881(18)
γ_e.................................	-2.235(69)E-5	-0.000643(16)
δ_e.................................	-6.64(48)E-7	...
$r_e(\mathring{A})$............................	1.17180630(86)	1.15133(12)

(B$^2\Sigma^+$–X$^2\Sigma^+$) [5, 35, 38, 53–56]. In addition to thin film deposition applications, the CN Violet system is also used extensively in astronomy, as it is a useful probe of C and N abundances and isotope ratios [57–59]. CN spectroscopy was also used to measure the temperature of the cosmic background [60, 61]. Due to its wide use, the spectroscopic data has been well studied. The B$^2\Sigma^+$ electronic state lies 25,752.6 cm^{-1} above the X$^2\Sigma^+$ ground state [52], as its energy level diagram shows in Figure 6. Once again, the upper state has a lower equilibrium internuclear distance as shown in Table 3, so band heading in the P branch is expected for the sequences of interest.

Transitions between energy levels occur with the selection rules previously stated.
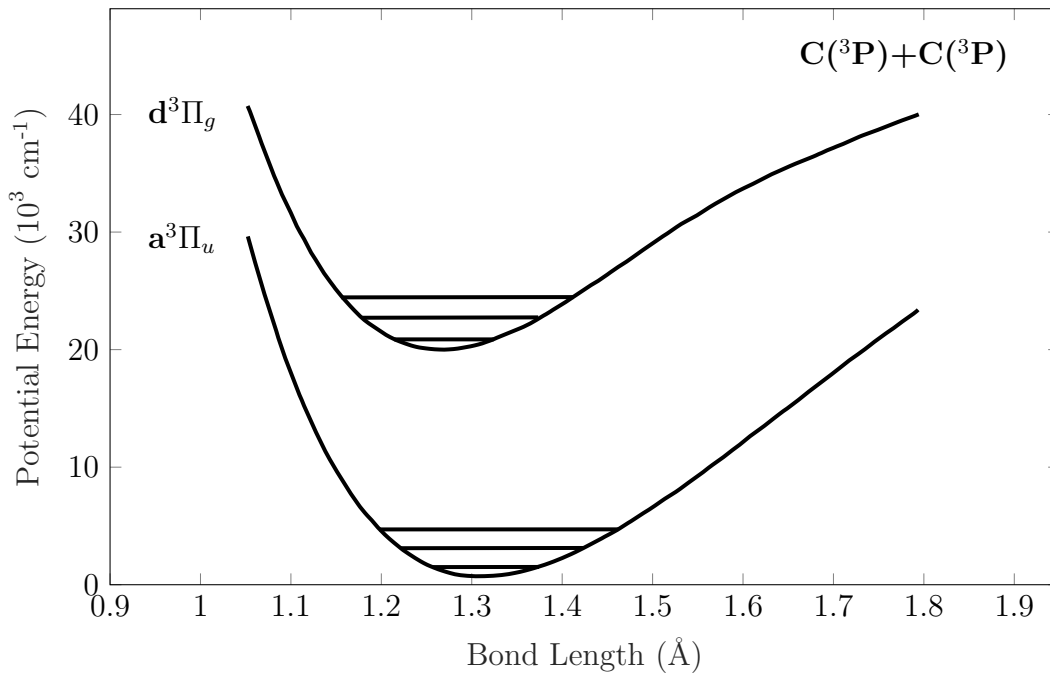
14
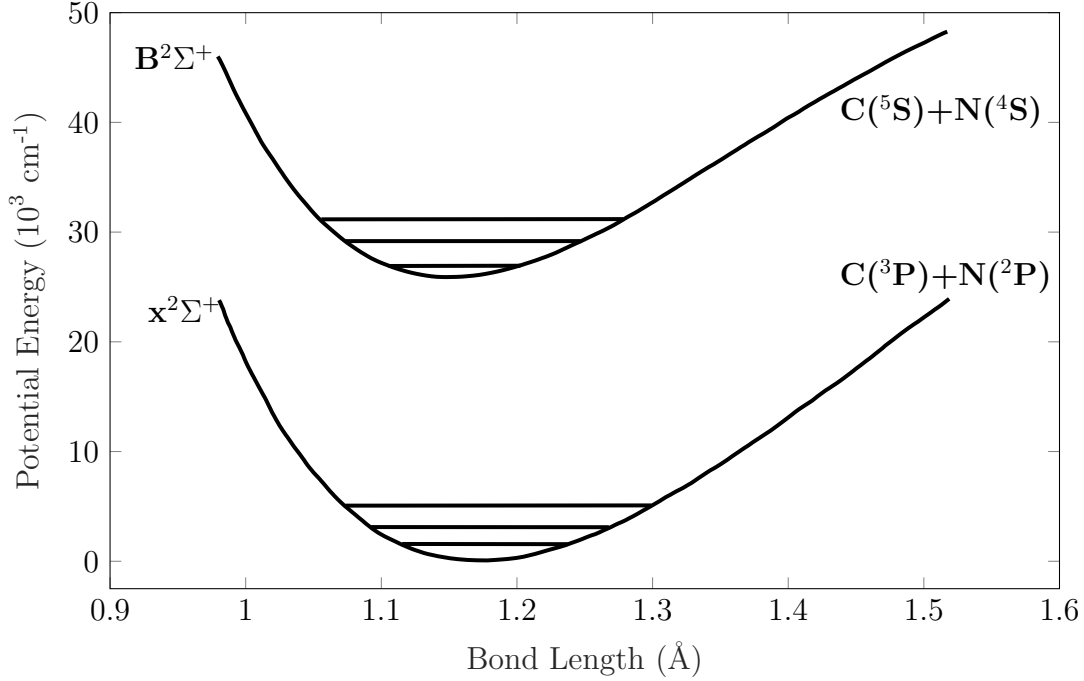
Figure 6. Potential energy surfaces for the $X^2\Sigma^+$ and $B^2\Sigma^+$ electronic states of CN. The $v = 0 - 2$ vibrational levels are shown for each state. (Adapted from [62])

Spontaneous emission of a photon can occur from a molecule in an excited state resulting in an emitted photon with an energy equal to the energy level spacing. The rate constant for this process is the Einstein A coefficient. It can be calculated using the equation in SI units [32]

$$A_{J'J''} = \frac{16\pi^3 v^3}{3\epsilon_0 hc^3} \frac{S_{J'J''}}{(2J'+1)} \tag{12}$$

where $S_{J'J''} \equiv \sum_{M',M''} |\langle J'M'| \hat{\boldsymbol{\mu}} |J''M''\rangle|^2$ is the line strength as defined in [63]. However, it can be approximately factored into the vibrational, electronic, and rotational components with

$$S_{J'J''} = q_{v'-v''}|\boldsymbol{R}_e|^2 S_{J''}^{\Delta J} \tag{13}$$

where $q_{v'-v''}$ is the Franck-Condon factor, $\boldsymbol{R}_e$ is the electronic transition dipole, and $S_{J''}^{\Delta J}$ is the Hönl-London factor [32]. Using the Einstein A coefficient, the spectral

15

irradiance from emission can be calculated,

$$I_\lambda \mathrm{d}\lambda = \frac{hcA_{ij}n_i l}{\lambda_i j^3}\mathrm{d}\lambda \tag{14}$$

where h is Planck's constant, c is the speed of light, A_{ij} is the Einstein A coefficient, n_i is the species concentration in the upper state i, l is the optical path, and λ_{ij} is the wavelength of the transition. All of these principles underly the actual experiment as well as the simulation that was used to process the data after the experiment.

III. Experiment and Methodology

3.1 Pulsed Laser Ablation of Graphite

The overall experimental setup is shown in Figure 7. The purpose of the experiment was to gather temporally resolved spectra and imagery of the carbon plume that resulted from the pulsed laser ablation of a graphite target. In addition to gathering temporally resolved data, different background gases were used. Air, argon, nitrogen, and helium were all used to understand the effects of background gas on the plume dynamics. Pulsed laser ablation of graphite was accomplished using a Lambda Physik LPX 305 KrF laser at $\lambda = 248$ nm operating at 1 Hz. The laser delivered an average 170 mJ/pulse onto a rectangular spot size of 8 x 1 mm as shown in Figure 8. The laser pulse had a FWHM of 25 ns [24]. With these parameters, the laser delivered an irradiance of 151 MW/cm^2 to the target each pulse. After being reflected off a
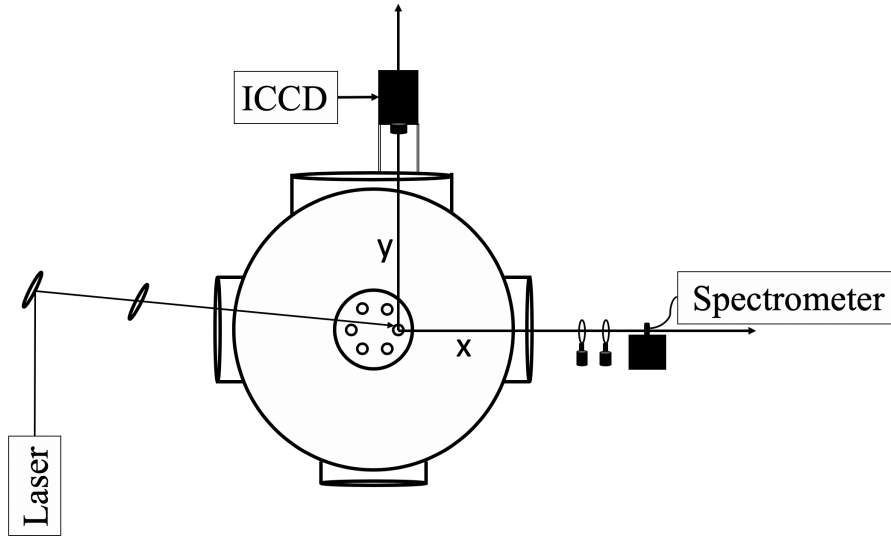
Figure 7. Diagram of the overall experimental setup. The ICCD camera is looking down along the y-axis toward the target with a 5.24 x 5.24 cm (0.102 mm per pixel) field of view (FOV). The spectrometer is coupled with a optical fiber for a viewing geometry down the x-axis with a spot size at the target of 1.1 mm. The laser is coming in at an angle so that it is incident on the target at a 45° angle.

17
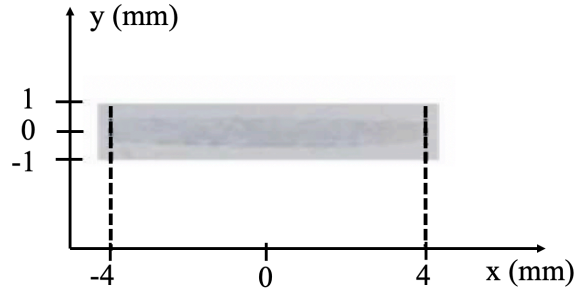
Figure 8. The laser spot size of the Lambda Physik LPX 305 KrF laser ($\lambda = 248$ nm) operating at 1 Hz. The spot size is appoximately 8 mm x 1 mm.

mirror with 99.9% reflection at 248 nm, the laser is focused onto the target inside the 10" vacuum chamber at a 45° angle using a 300 mm focal length plano-convex fused silica 2" lens as shown in Figure 9.
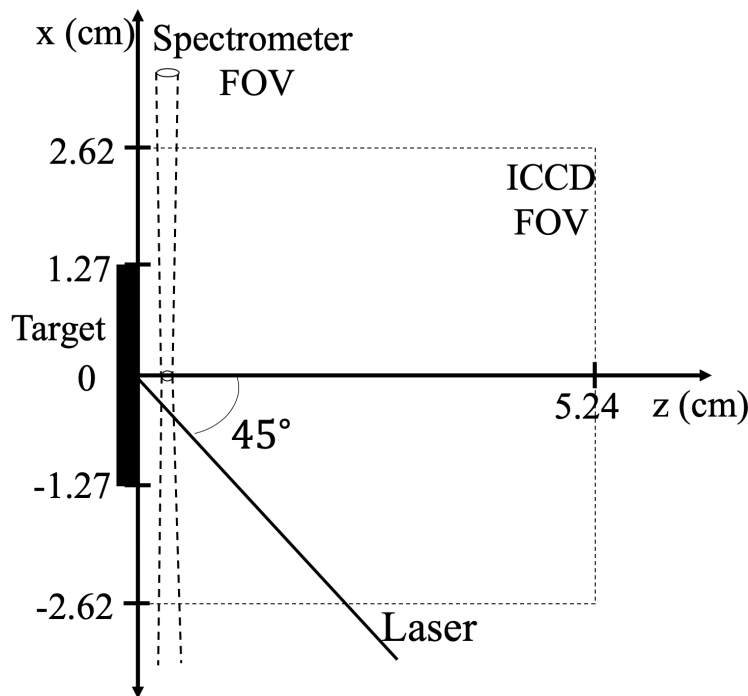
Figure 9. Diagram of the overall experimental setup. The ICCD camera is looking down along the y-axis toward the target with a 5.24 x 5.24 cm (0.102 mm per pixel) field of view (FOV). The spectrometer is coupled with a optical fiber for a viewing geometry down the x-axis with a spot size at the target of 1.1 mm. The laser is coming in at an angle so that it is incident on the target at a 45° angle. The plume will propagate in the direction normal to the surface target.

18

The vacuum chamger was evacuated using a Pfeiffer turbomolecular pump/Varian DS 102 mechanical pump combination resulting in a base pressure of approximately 10^{-6} Torr, which was measured by a Varian K7360 Type 5721 ionization gauge. After being evacuated for at least 12 hours, the chamber was backfilled and maintained at the desired pressure of background gas (Air, Ar, He, or N_2) at either 1 or 10 Torr using an MKS Baratron gauge and downstream MKS butterfly valve controlled by a MKS 600 series pressure controller.
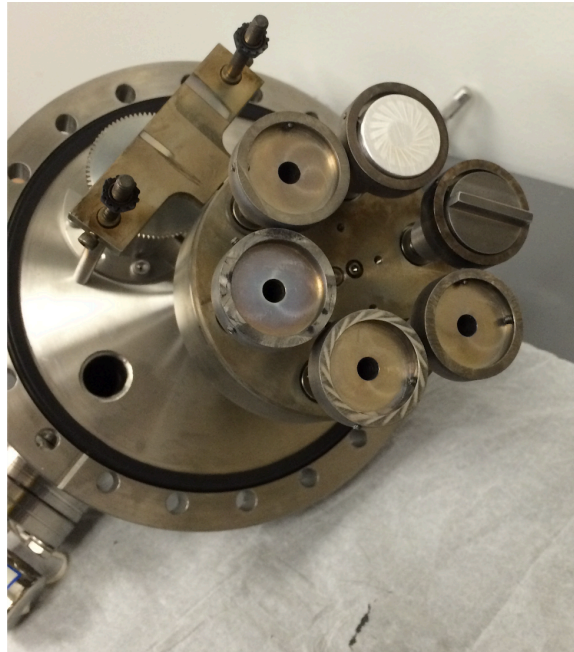
Figure 10. The target carousel with ablated sample and spatial calibration target are shown. The target carousel holds up to 6 samples at a time. During the experiment, the sample rotates at 10 rpm to randomize the laser spot location on the target, which decreases localized cratering.

The targets were 1" diameter by 0.25" thick pyrolytic graphite (99.999% C) from Kurt J. Lesker. A carousel that could hold six targets was used as shown in Figure 10. During testing, each target was rotated along the z-axis at 10 rpm to avoid excessive cratering. A reference target was also initially placed in the carousel to determine the viewing geometry of the spectrometer, which can also be seen in Figure 10. It

19

had a 25.4 mm x 6.2 mm x 1mm stainless steel spatial grid welded to the front of a 1" diameter by 0.25" thick stainless steel disk.
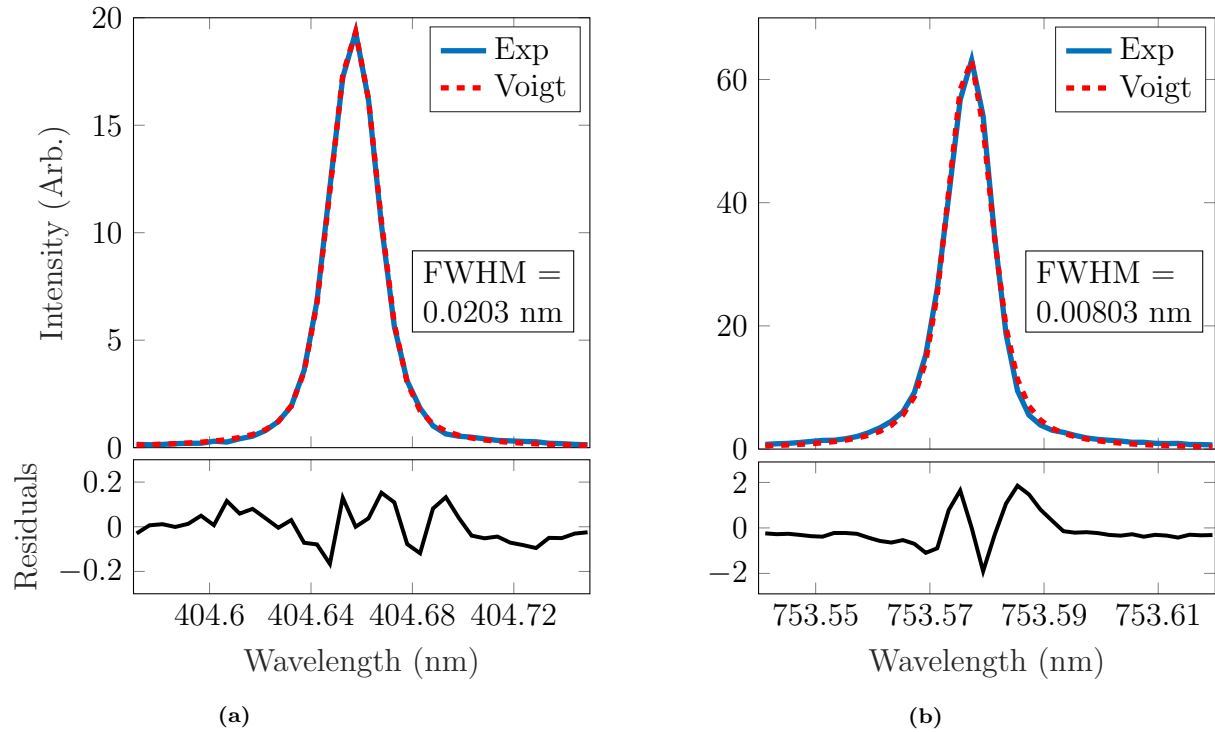
Figure 11. (a) The Instrument line shape of the McPherson 209 1.33 m spectrometer obtained from the 404.656 nm line of Hg. It is a Voigt profile with a FWHM of 0.0203 nm. (b) The instrument line shape of the 753.57 nm line of Ne. It is a Voigt profile with a FWHM of 0.0783 nm.

A McPherson 209 1.33 m spectrometer equipped with a Princeton Instruments PIMAX4 1024 x 1024 intensified charged coupled deviced (ICCD) array was used to capture the visible emission spectra of the plumes. A fiber bundle (NA of 0.22) was coupled to the spectrometer, and two 2" biconvex fused silica lenses were used as collection objects. The closest to the chamber was a 300 mm focal length lenss, which was followed by a 100 mm focal length lens located 3 cm from the 300 mm lens. The spectrometer had a slit width of 40 μm and blazed grating with 1800 groves/mm was used. With this setup, a spectral resolution of $\delta\lambda = 0.0203$ nm was obtained on the blue side. The instrument line shape has a Voigt profile as shown in Figure 11. The

20

specific components of the profile at 400 nm are a Gaussian with a FWHM of 0.0172 nm, and a Lorentzian with a FWHM of 0.0099 nm. On the red end of the spectrum, the Voigt profile had a FWHM of 0.00803 nm (Gaussian FWHM of 0.0062 nm and Lorentzian FWHM of 0.0052 nm).
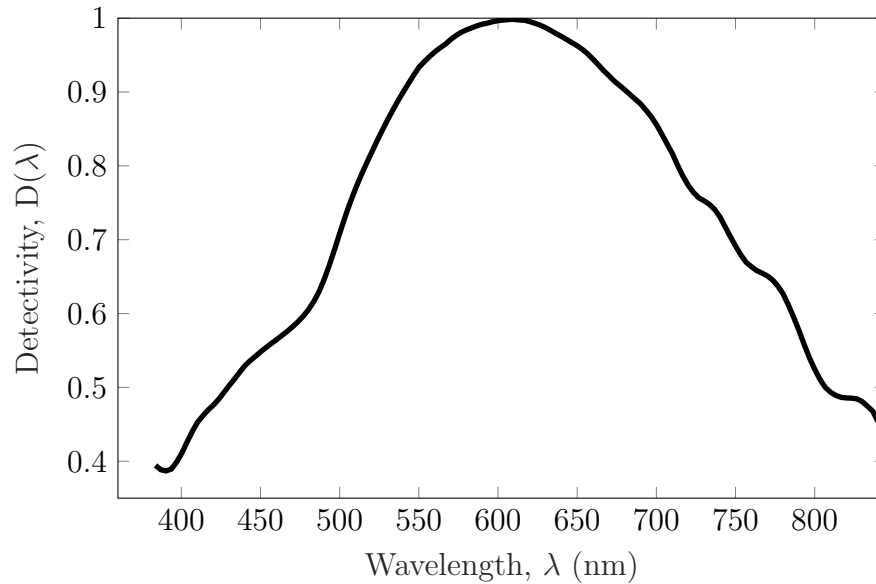
Figure 12. Detectivity as a function of wavelength is displayed for a gate width of 250 ns. The detectivity drops off rapidly with wavelength outside the middle of the visible spectrum.

The spectrometer had a spectral viewing window of 2-4 nm (depending on grating angle) throughout the visible spectrum, so the grating was manually turned in between shots to collect spectra at various wavelengths. At each wavelength, the camera was gated with delay times from 1-10 μs and gate widths of 100-1000 ns to develop temporally resolved spectra. The shots suffered from $< 5\%$ pulse-to-pulse laser flicker and ≤ 10 ns pulse-to-pulse timing jitter. The collection of various gated shots at a specific wavelength happened over approximately 100 shots. The spectrometer was spectrally calibrated each day using Hg and Ne lamps. Radiometric calibrations were accomplished using a NIST certified tungsten (W) filament. The plume spectra were capture with varying gate widths, so the radiometric calibration also incorporated

21

multiple gate widths to ensure the detectivity was properly characterized. The detectivity is shown in Figure 12. The window and lens transmission over the visible spectrum was calculated to be 0.77. A spatial resolution of 1.1 mm was determined by shining a lamp through the back of the fiber onto the focus aid in the vacuum chamber as shown in Figure 13.
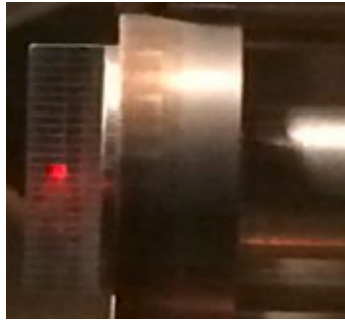
Figure 13. Viewing from the x-axis, the red dot is from a light shining through the back of the fiber onto the focus aid. A spot size of 1.1 mm was determined using the grid on the focus aid as shown.

Visible imagery was also collected with a Princeton Instruments PIMAX I 512 x 512 Gen III ICCD with a Nikon AF Nikkor 60 mm micro f/2.8 lens. The system had a field of view (FOV) of 5.24 x 5.24 cm (102 μm per pixel). Per previous characterization [24], the PIMAX Gen III quantum efficiency had a maximum of 40% at 700 nm and was above 20% from 410-890 nm. The camera was gated with nonlinearly varying gate delays and gate widths of 1.5-11.5 μs and 2-200 ns, respectively. A ST-133 controller externally triggered by the laser electronics contolled the gating. Using the focus aid, a point spread function (PSF) of 0.5 mm (5 pixels) was calculated.

Band pass filters were used to isolate various emissions from neutral and ionized species, which will help to correlate the spectra and the imagery data. The various filter information is shown in Table 4. They were specifically chosen to correspond to CN, C_2, Ar, and C I lines. Combing the imagery and the optical emissions spectra will aid in developing an understanding of the plume dynamics. To gain an understanding

22

of the spectra, simulations need to be conducted in order to compare to the ones observed experimentally.

Table 4. The bandwidth and center wavelengths for each filter used in the imagery is shown here. Possible species of interest that correspond to those wavelengths are also shown.

Center Wavelength (nm)	Bandwidth (nm)	Species of Interest
374	10.8	Possibly CN Violet
393	8.9	CN Violet (0,0) Band head
521.49	9.22	C2 Swan (0,0)
761	10	Ar I
830.63	9.65	C I

3.2   PGOPHER Simulation

To aid in understanding the plume dynamics of the PLA of graphite, simulations were conducted using the spectra obtained from the experiment to extract rovibrational temperatures. Two models were developed for the simulations: one for the C_2 Swan band and one for the CN Violet. The simulations were accomplished using PGOPHER, which is a program developed by Dr. Colin Western from the University of Bristol to simulate rotational, vibrational, and electronic spectra. It is a multi purpose tool for the simulation and fitting of molecular spectra [64]. PGOPHER was chosen for its ability to handle a large number of transitions and interactions. It also had previously been used in simulating C_2 and CN spectra [40, 52]. Each model is broken down into a tree structure as shown in Figure 14.

The mixture contains top level settings for the calculations such as units. The simulation contains objects which describe the experimental conditions such as temperatures and linewidths. When both a Gaussian and Lorentzian linewidth are specified, a Voigt convolution is performed. The species contain the molecules object, which

23
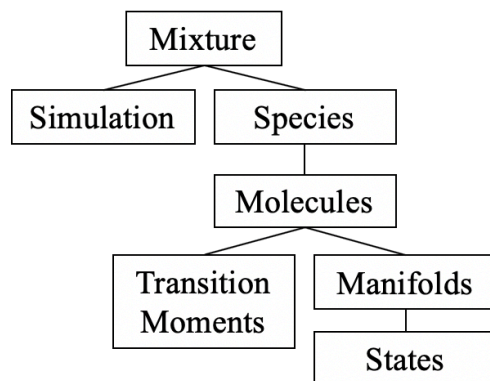
Figure 14. **An overview of the structure of a PGOPHER model is shown.**

specify the type of molecule (linear in this case) and other things such as symmetry. The manifolds are groups of states, such as a specfic electronic state. The state object contains the band origin and rotational constants for a particular state. Perturbations (not shown in figure) can also be added to the manifolds object. Also under the molecules object is the transition moments object which describes the transitions between or within the various manifolds. It contains various transition moments for each state to state transition depending on the type. For the models used in this experiment, only spherical (electric dipole moment) transitions were used.

The C_2 Swan ($d^3\Pi_g$ – $a^3\Pi_u$) model was designed with the $v = 0 - 10$ vibrational states for the $d^3\Pi_g$ electronic state and the $v = 0 - 9$ vibrational states for the $a^3\Pi_u$ electronic state using the available spectroscopic constants [51]. The constants that were used in the model are shown in Table 9 in Appendix A. No perturbations were included in this simulation. The transition dipole moments were obtained from another previously reported experiment [40]. For reference, the Einstein A coefficients are shown in Table 10. The transition moments were calculated from the Einstein A coefficients. The radiative lifetimes from these are approximately 100 ns. Although the model simulates the whole system, the portion used to estimate the temperatures is the $0 - 0$ band and part of the $1 - 1$ band in the $\Delta v = 0$ sequence. This portion

24
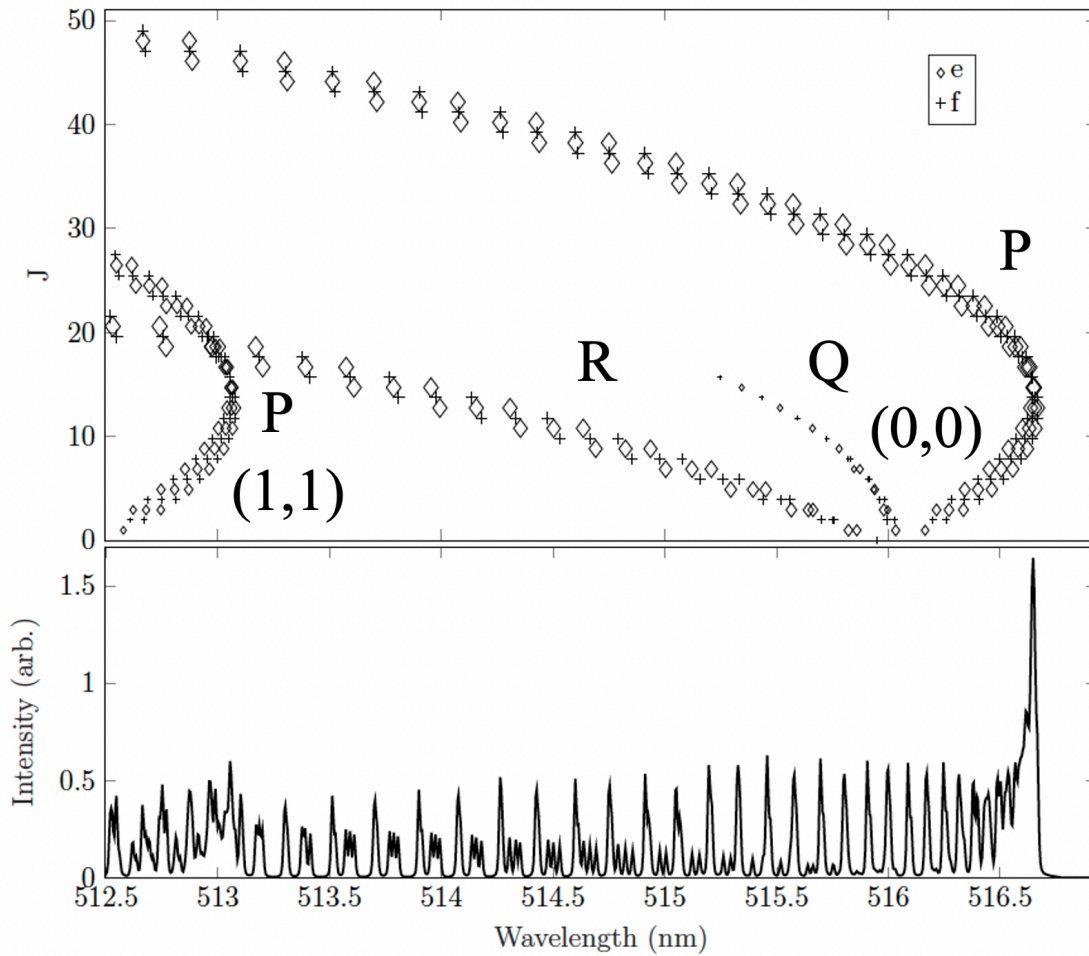
Figure 15. The Fortrat diagram along with the spectra for the C_2 Swan simulation is shown. The Fortrat diagram markers are scaled based on intensity. The P, Q, and R branches of $0-0$ band are visible as well as the P branch of the $1-1$ band.

with its associated Fortrat diagram is shown in Figure 15.

The CN Violet $(B^2\Sigma^+ - X^2\Sigma^+)$ model used the $v = 0-15$ vibrational states for the $B^2\Sigma^+$ electronic state and the $v = 0 - 15$ vibrational states for the $X^2\Sigma^+$ electronic state [52]. The spectroscopic constants for these states are shown in Table 11 in Appendix A. The associated Einstein A coefficients used to calculate the transition moments are shown in Table 12 in Appendix A for reference. These produce radiative lifetimes of approximately 60 ns [52]. The portion used to estimate the temperatures is mainly the $0-0$ band, the $1-1$ band, the $2-2$ band; however, the $3-3$ band up

to the $10 - 10$ band add small contributions as shown in Fortrat portion of Figure 16.
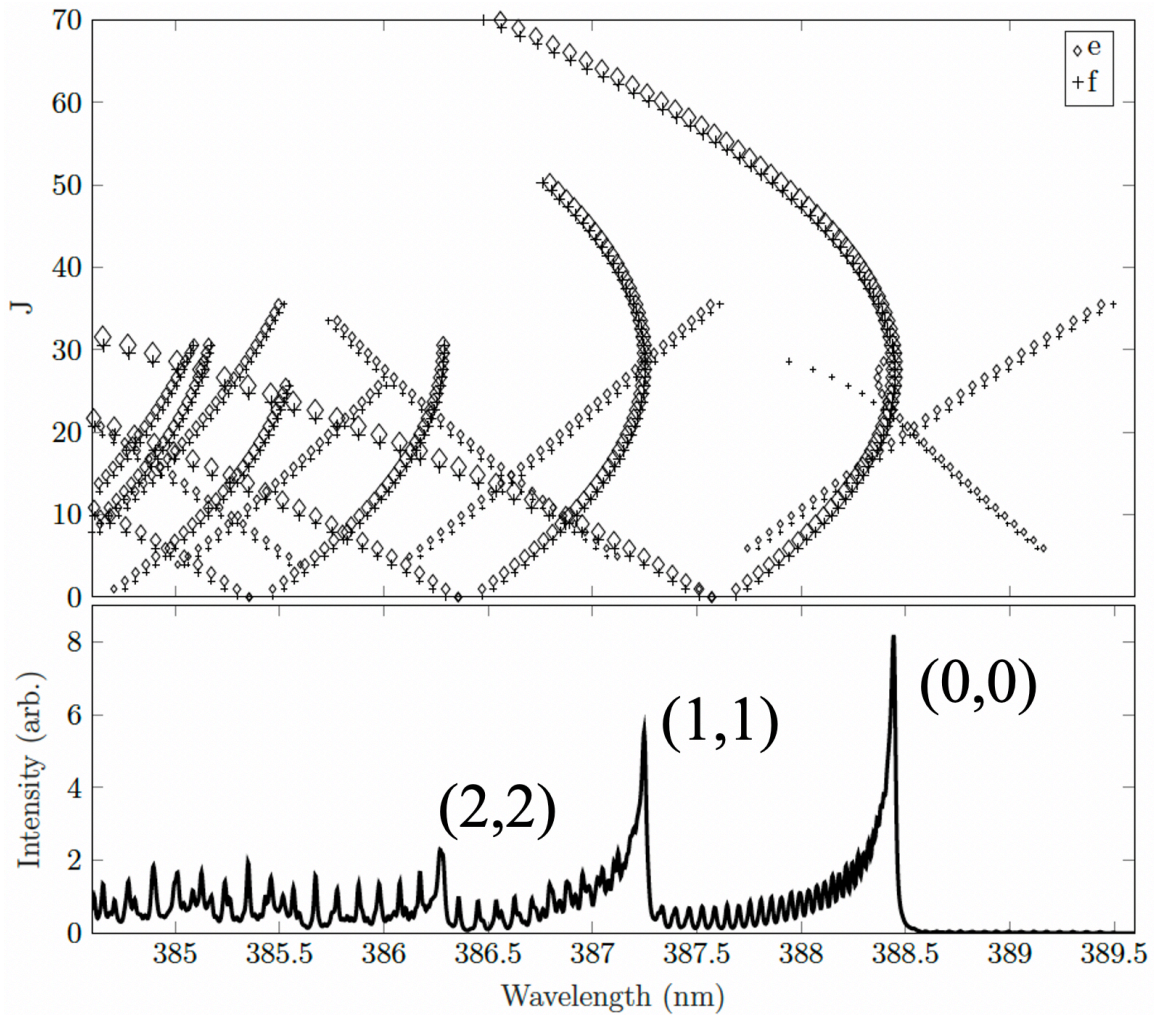
Figure 16. The Fortrat diagram along with the spectra for the CN Violet simulation is shown. The Fortrat diagram markers are scaled based on intensity.

To extract rotational and vibrational temperatures from the experimental data, a fitting routine was developed using the models described above. The experimental data was collected in various tests. A single test is a collection of frames that were collected under the same experimental conditions (i.e. background gas and pressure). The different frames within a test then had different gate delays in order to temporally resolve the plume propagation after the laser irradiation occurred. Thus, by fitting each frame, a rotational and vibrational temperature was extracted at each time step

26

for a given test. An overview of the process for fitting a test comprised of many frames is shown in the block diagram in Figure 17.
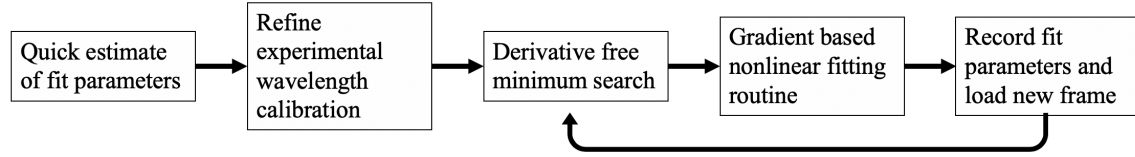
Figure 17. An overview of the fitting routine for an individual test is shown in this block diagram. The fit parameters are extracted at each frame of the test in order to give temporally resolved temperatures.

A function was written in Matlab to change various parameters of the simulation in order to fit the simulation to the experimental data using the nonlinear fitting tools native to MATLAB. The function floated the following parameters in the simulation: Gaussian line shape (FWHM), Lorentzian line shape (FWHM), rotational temperature, vibrational temperature, vertical scale factor, and a constant vertical offset. These parameters were simultaneously fit using a nonlinear contour fitting process; however, there were a few calibration steps prior to the actual fitting. Although a spectral calibration was performed each day during testing, the spectral axis was found to be slightly off for each test, so it was then fine tuned using the simulated spectra to improve the calibration. Once this was done, the actual fitting process could occur.

Recall from Section 2.3 that Equation 14 described how the spectral irradiance can be calculated. If we assume that the rotational and vibrational temperatures are not in equilibrium, then the upper state column density can be calculated using

$$n_i l = \frac{n'l}{Q}(2J'+1)e^{\frac{-F(J')}{kT_R}} e^{\frac{-G(v')}{kT_v}} \tag{15}$$

where n' is the total population of the $\mathrm{d}^3\Pi_g$ (upper) state, l is the optical path length, J' is the upper state total angular momentum quantum number, Q is the partition

27

Figure 18. C_2 Swan simulated spectra. (a)The effect of the rotational temperature on the simulated spectra is shown. (b) The effect of the vibrational temperature on the simulated spectra is shown.

function, $F(J')$ is the the upper state rotational energy, $G(v')$ is the upper state vibrational energy, k is the boltzmann constant, T_R is the rotational temperature, and T_v is the vibrational temperature. This means that changing the rotational and vibrational temperatures affects the relative populations of the rovibrational energy levels.

Understanding exactly how the temperatures affect the populations in the rotational and vibrational levels for each molecule is best done visually. Figure 18 displays how a change in the rotational temperature or the vibrational temperature affects the spectral region that will be fit. The plots were normalized to the peak intensity of the band head to emphasize the changes in the relative populations, which is what the temperatures are truly changing. The rotational temperature changes the spectrum a lot since a large portion of the (0,0) band is visible; whereas, the vibrational temperature only affects a small portion because only part of the P branch of the (1,1) band is visible.

Figure 19 displays similar information but for the CN Violet spectrum. This portion of the spectrum encompasses a larger amount of vibrational bands; however, the spectrum is less sensitive to changes in the rotational and vibrational temperatures
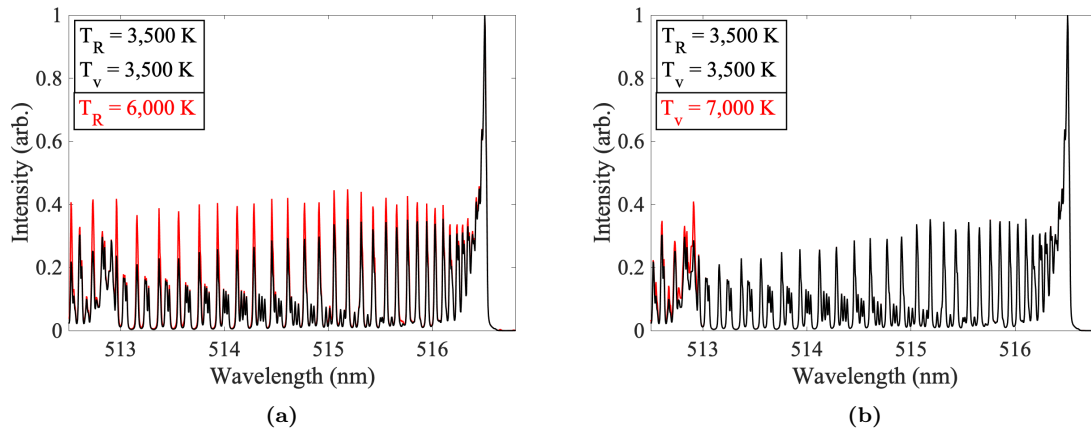
28
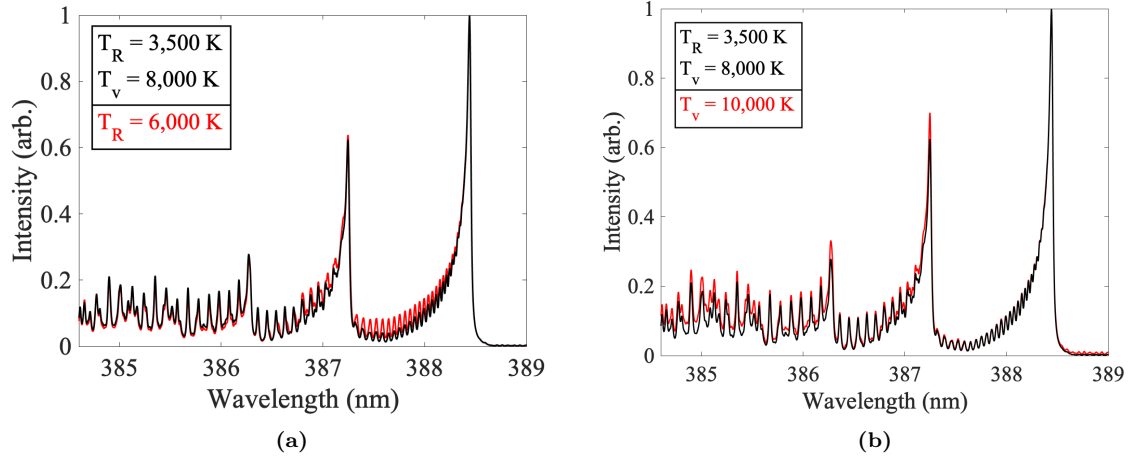
Figure 19. CN Violet simulated spectra. (a)The effect of the rotational temperature on the simulated spectra is shown. (b) The effect of the vibrational temperature on the simulated spectra is shown.

due to the spacing. Because of this, we can expect the error bounds for the CN Violet temperatures to be larger than the ones for the C_2 Swan.

Regardless of these differences, the fit process was the same for both the C_2 Swan and CN Violet regions of the spectra. Once the wavelength axis is finished being calibrated for a particular test, each frame starts with a non-gradient based minima search to give a better chance of finding the global minimum and then moves into a gradient based approach to fine tune the floated parameters. The parameters are bounded during these processes. An initial bound for each variable was developed based on its reasonableness in the simulation compared to the experimental data. These bounds for each simulation are shown in Table 5.

The fit bounds were initially a lot broader to ensure the model was not overly constrained; however, after a few tests from various time steps across the different background gases, they were tightened using the early results to improve run times. The various bounds are different because the initial testing led to those bounds being created. Widening the bounds naturally increases the run time drastically due to the initial non-gradient based fitting. Overall, 53 tests ($\sim$ 2000 frames) were fit using the

29

Table 5. Fit parameter bounds for both C_2 and CN fitting routines.

Fit Parameters	C_2		CN	
	Lower	Upper	Lower	Upper
Gaussian FWHM (nm)	0.008	.02	0.001	0.02
Lorentzian FWHM (nm)	0.008	.02	0.001	0.03
Rotational Temperature, T_R (K)	1500	10000	3000	8000
Vibrational Temperature, T_v (K)	1500	10000	5000	15000
Scale Factor (arb)	0.1	12	0.1	8
Offset (arb)	$\pm 15\%$ of frame baseline			

C_2 model, and 12 tests (~ 500 frames) were fit using the CN model. The results from these simulations will be presented in the following section.

IV. Results and Analysis

4.1 Plume Imagery

Before the simulations are discussed, it is helpful to first glance at the plume imagery to orient the reader with what the plume looks like and how it is propagating through the background medium, which is key to understanding the dynamics of the plumes during the nanosecond pulsed laser ablation of graphite. Overall, approximately 7,000 images were captured under the various test conditions, so this section will only display a small portion of those. The imagery complimented the spectra well, as it was able to capture events on time scales that were just not possible with the spectrometer.

Figure 20 shows the broadband (no filter) plume imagery for six different time delays. The tests were conducted in an argon background. It is important to note the timing of each plot. The plume comes off extremely bullet like initially as shown in the first three images. The shock front slows down very fast, and the plume begins to expand outward on the sides. After about 1 microsecond, the front of the plume does not progress farther forward. This also highlights the inital spatial averaging that occurs with the spectrometer. Figure 20(c)-(d) show the initial shock front traversing through the FOV of the spectrometer during its early collection times. With a spectrometer gate width of 250 ns or 500 ns depending on what molecule is being looked at, there is a significant amount of averaging that occurs in the first two time steps; however, as is shown in the later time steps of the imagery, there is much less plume movement.

The background gas significantly affects the propagation of the plume. Particularly, the helium background gas varies significantly. Figure 21 shows snapshots of the plume imagery at the same time steps but in a helium background gas. Comparing

31

(a) $t = 64$ **ns**

(b) $t = 315$ **ns**

(c) $t = 590$ **ns**

(d) $t = 1.1$ μ**s**

(e) $t = 5$ μ**s**

(f) $t = 11.5$ μ**s**

Figure 20. Various images are plotted from the experiment conducted in 10 torr of argon. The highlighted red area is the estimated location of the spectrometer view across the x-axis.

these to Figure 20 highlights how different the plume propagation truly is. There are a few interesting features. First, the initial velocity is higher, as the plume has
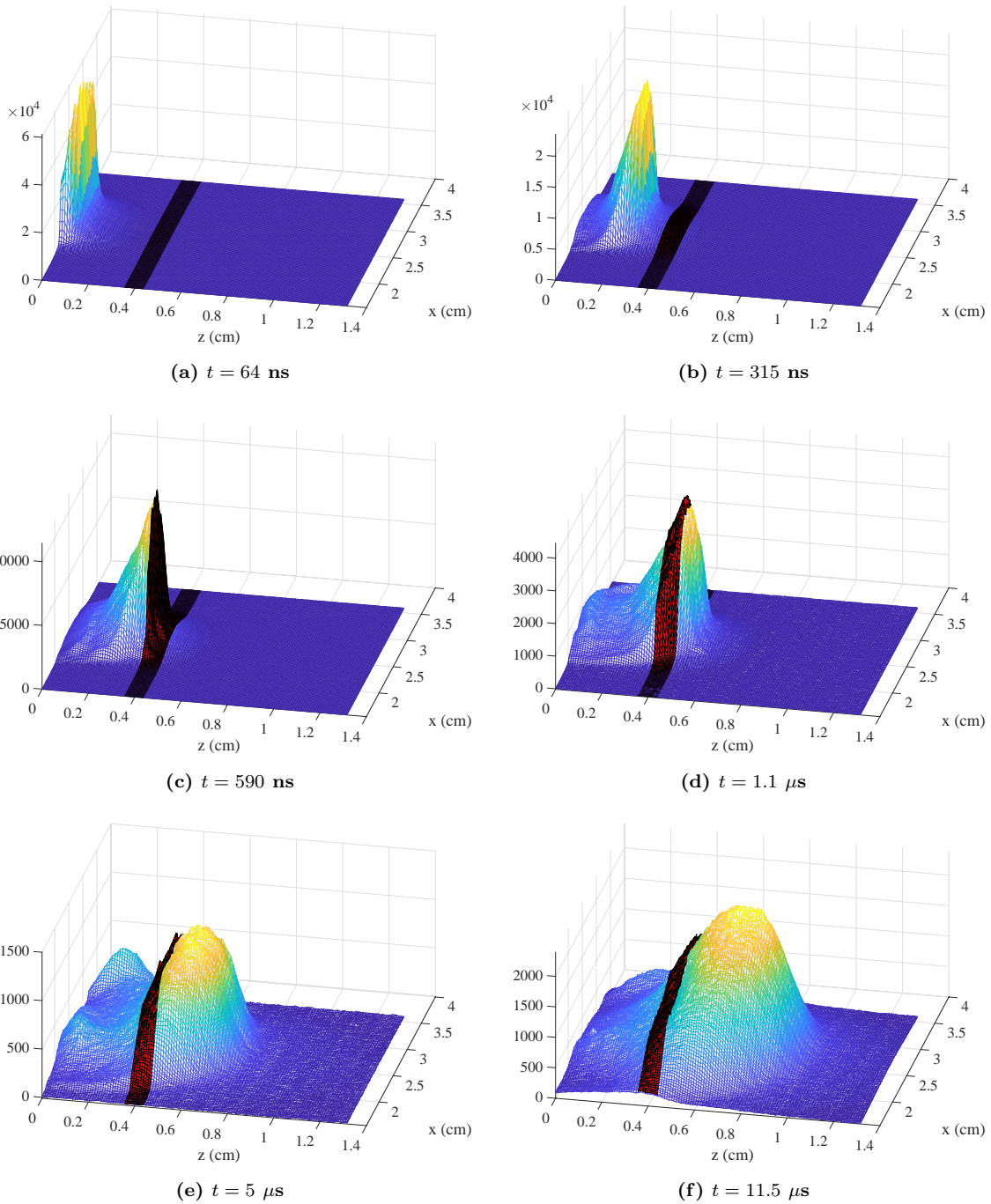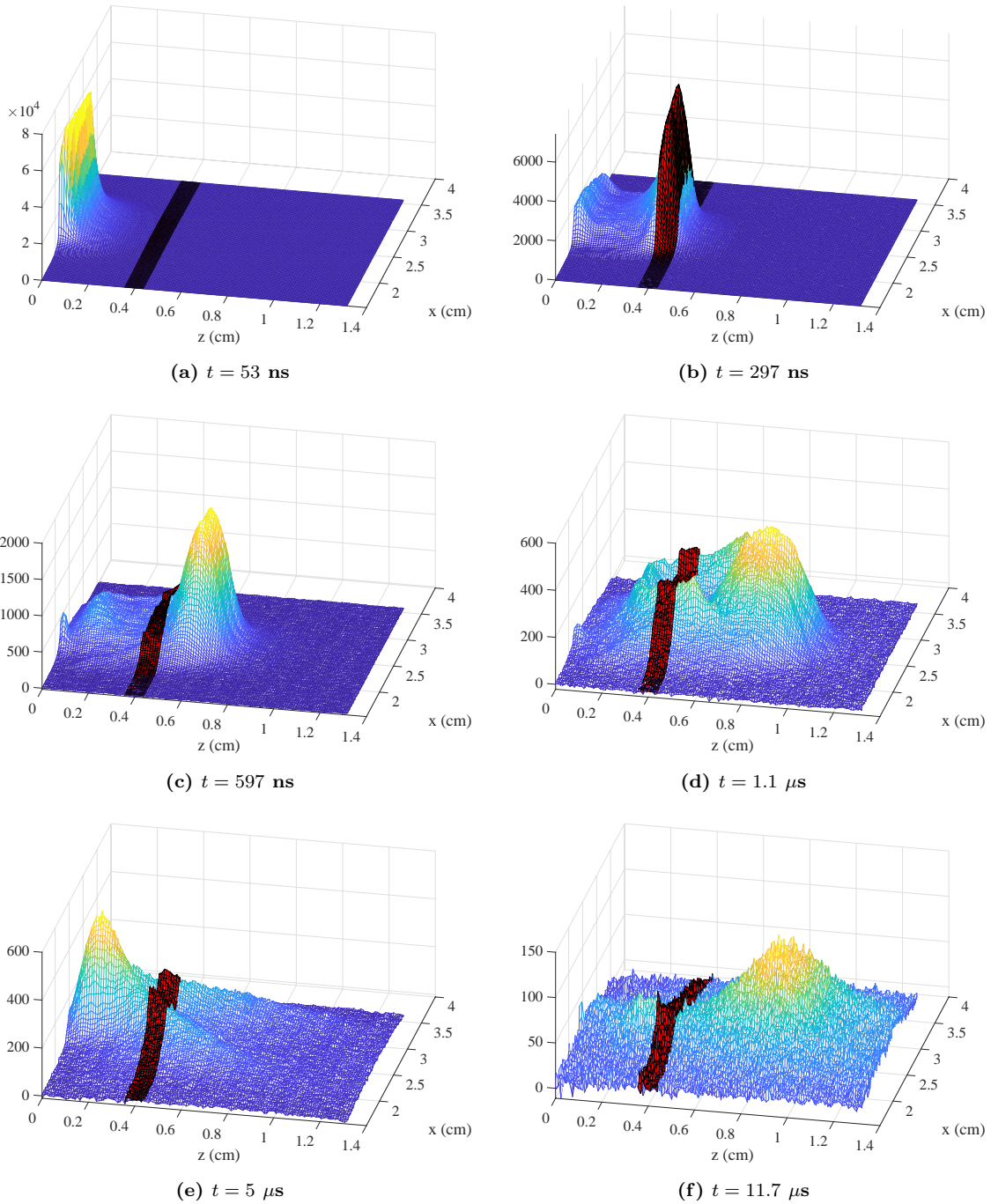
32

Figure 21. Various images are plotted from the experiment conducted in 10 torr of helium. The highlighted red area is the estimated location of the spectrometer view across the x-axis.

traveled mucher farther in helium at time $t = 300$ ns when compared to the argon background imagery. The second thing to note is the plume propagates out much

farther, which will become even more apparent when looking at the shock front propagation in Section 4.2. The last thing to note is in Figure 21(d)-(f). It appears as though part of the plume reverses direction and comes back toward the target. This odd phenomena will be further documented in Appendix C.

Viewing the imagery is a qualitative way to begin to understand the dynamics of the plume after the laser ablates the graphite target. However, analyzing the shock front propagation provides a more quantitative discussion of the plume dynamics.

4.2 Shock Front Analysis

This section will detail the analysis of the shock fronts for the various tests in both the filtered and unfiltered imagery. The theoretical foundation for this was discussed in Section 2.2. It is useful to go through an example of the full process in order to understand exactly how the data is extracted prior to fitting the various models.

To find the shock front, centerline intensities are taken along the image to find the 50% max of the shock front, similar to that which is discussed in [28]. Figure 22 shows an example of finding the shock front location for two different time steps. At each time step, the centerline intensities are taken for each image. This is shown in Figure 22(a)-(b) for two separate times. Once the centerline intensity is taken from the imagery, the 50% max of the intensity is taken to be the actual location of the shock front. Figure 22(c)-(d) shows the location of the shock front as represented by the blue circle in each plot. Once this is done for each time step where the shock front is clearly visible, we then have the shock front location, $R(t)$. The shock front location calculated from the no filter imagery for each of the background gases is shown in Figure 23.

It is clear from Figure 23 that the plume propagation is different in the helium background gas when compared to the other three background gases. It is important

34

(a) $t = 107$ **ns**

(b) $t = 293$ **ns**

(c) $t = 107$ **ns**

(d) $t = 293$ **ns**
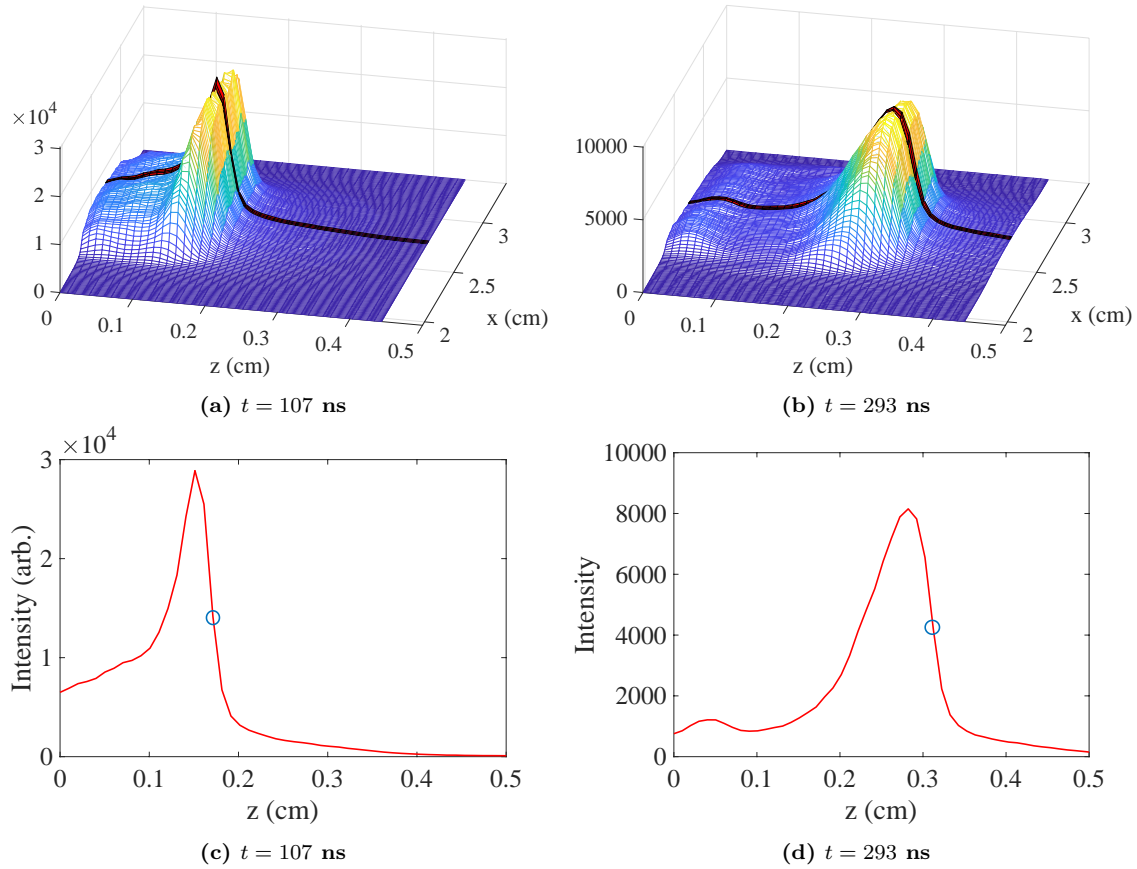
Figure 22. Two separate time steps are plotted to show how the shock front is actually tracked. (a)-(b) Two images at different times are plotted. The highlighted area in red is the centerline intensity for each given frame. (c)-(d) These are the 1-D centerline intensity plots gathered from the two plume images. the 50% max of the centerline intensity is highlighted by the blue circle. This is what is deemed as the actual shock front location.

Table 6. The reduced mass of C_2 and the various background gases used in the experiment are displayed in atomic mass units. The reduced mass with helium is drastically different than the others.

Background Gas	Reduced mass, μ (amu)
Air	13.1
Ar	15
N_2	12.9
He	3.43
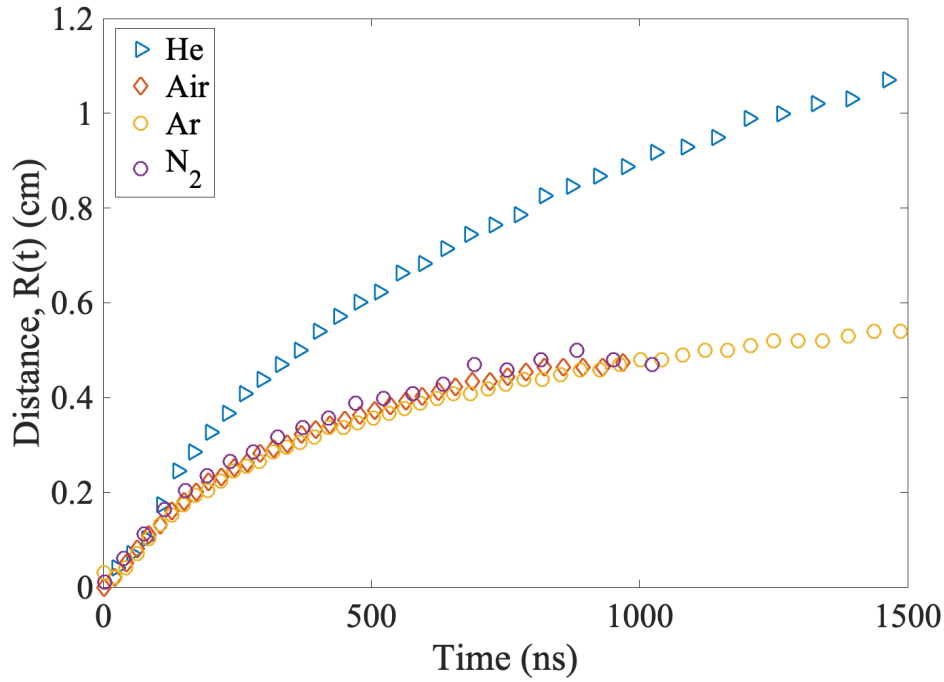
Figure 23. The shock front location (calculated from the broadband imagery) in each background gas is plotted as a function of time.

to note that the reduced mass of C_2 and He is much different than the rest of the background gases as shown in Table 6. It appears from the imagery, the carbon plume is just plowing through the helium background in comparison to the other three background gases. This will become important later because the spectrometer was not moved during any of the experiments, so the FOV is looking at a much different portion of the plume during the experiments with a helium background as opposed to the experiments with air, argon, and nitrogen backgrounds.

With the shock front location properly characterized, various shock propagation models can be used to examine the data. Recall from Section 2.2, two models, the Taylor-Sedov model and the drag model, were described. These are the two models that will be used to fit the data, and the estimation of the free expansion velocity from the drag model will also be shown. An example fit from the shock location in the experiment with a 10 Torr air background is shown in Figure 24. The drag

36
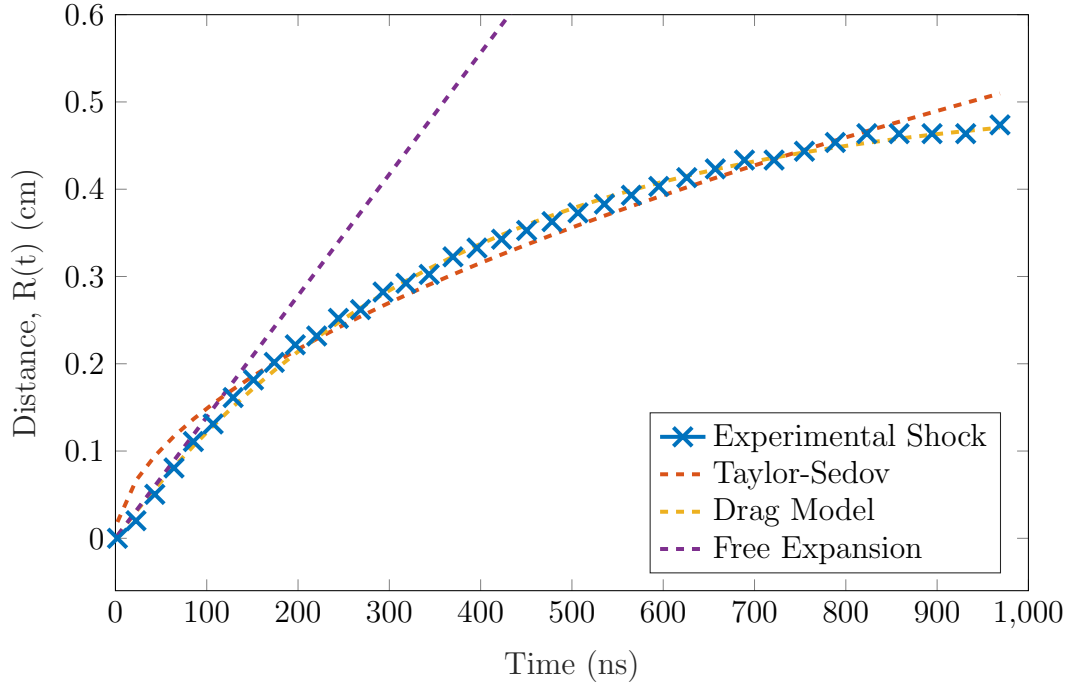
Figure 24. The experimental shock front from imagery data with no filter in 10 Torr Air. The intial velocity was $v_0 = 1.39 \pm 0.05$ cm/μs, and a stopping distance of $R_s = 0.506$ cm for the drag model. The Taylor-Sedov model had $n = 1.69$, which suggests it is somewhere between a spherical wave and a cylindrical wave

model does particularly well in describing the shock front propagation, and this trend was common throughout all of the data. The intial velocity for the drag model was $v_0 = 1.39 \pm 0.05$ cm/μs, and a stopping distance of $R_s = 0.506$ cm. Interestingly, the value of n for the Taylor-Sedov model was found to be 1.69, which means it is somewhere between a plane wave and a cylindrical wave. This makes sense given the elongated rectangular nature of the laser spot size. It should be noted there is a degree of difficulty in fitting the Taylor-Sedov model because correctly calculating where the model is valid becomes difficult. Equation 6 from Section 2.2 defines the limits; however, the lower limit is difficult to estimate due to not knowing the actual ablated mass.

To compare each of the background gases, their shock front model parameters are all displayed in Table 7. Some of the expected trends were the larger stopping distance

37

Table 7. The Taylor-Sedov model and drag model parameters are displayed for all of the no filter imagery.

	Taylor-Sedov Model		Drag Model	
	n	$\xi\left(\frac{E}{\rho_b}\right)^{1/(n+2)}$	R_s (cm)	v_0 (cm/μs)
Air	1.69 ± 0.26	0.012 ± 0.003	0.506 ± 0.008	1.39 ± 0.05
Ar	1.99 ± 0.25	0.015 ± 0.003	0.614 ± 0.012	1.03 ± 0.06
He	1.41 ± 0.12	0.016 ± 0.002	1.161 ± 0.019	1.80 ± 0.06
N_2	1.88 ± 0.21	0.016 ± 0.003	0.514 ± 0.009	1.47 ± 0.23
N_2 (1 Torr)	1.71 ± 0.18	0.024 ± 0.005	1.585 ± 0.033	1.82 ± 0.08

for a helium background as well as for the lower pressure nitrogen background. The error analysis for the various parameters is detailed in Appendix B. Another way to view Figure 24 is to take the derivatives of the experimental values as well as the models to obtain the velocities. These can be converted to Mach number by using the speed of sound in each background gas, which is displayed in Table 8. This stark

Table 8. The various sound speeds are displayed along with the average initial mach number for each background gas

Parameter	Air	Ar	He	N_2	N_2 (1 Torr)
Speed of Sound (cm/s $\times 10^4$)	3.47	3.22	10.2	3.85	—
Average Initial Mach Number	40	41	19	39	57

contrast in Mach number between helium and the rest of the background gases further shows how different the dynamics between the two groups must be.

Using various filtered imagery helps to visualize where the different particles are located in the shock. Figure 25 plots the various filtered shock front locations found using the different types of filtered imagery in an argon background. The curves are each labeled based on what emission species was visible in that wavelength range. The C_2 is the first to drop off of the shock, while the atomic carbon and argon continue to

38
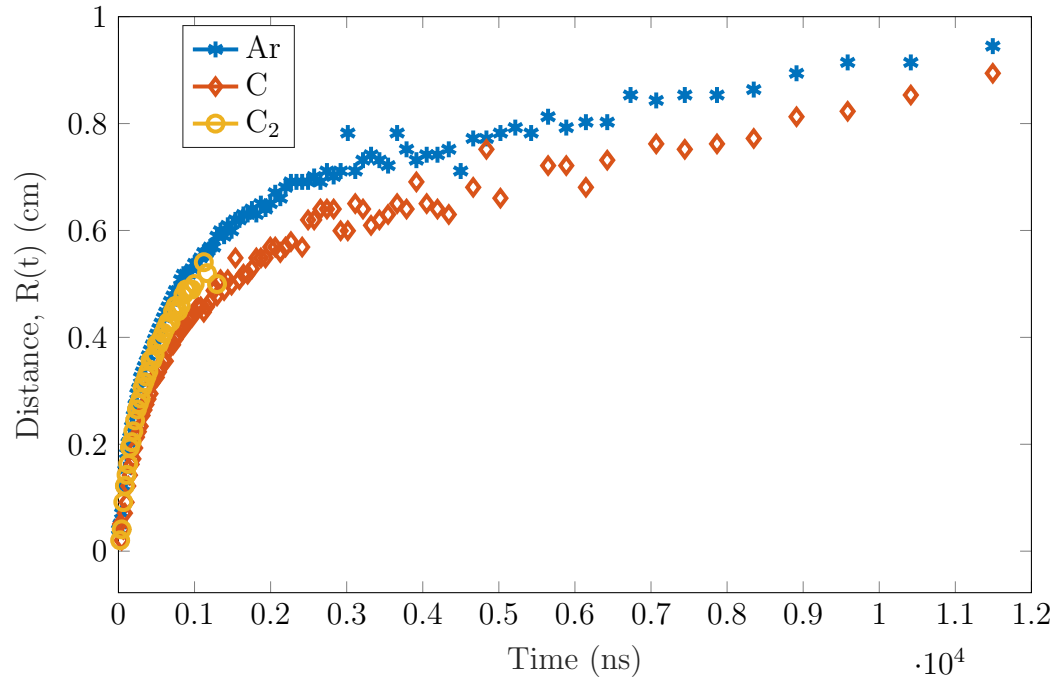
Figure 25. The splitting of the various shock fronts based on species is shown in an argon background gas. The argon is continually excited as it is plowed forward by the inital plume.

propagate. The atomic argon continues to stay connected to the shock as the plume is plowing into the background gas. Now that the imagery has been characterized, we can begin to look at the various spectra that were collected.

4.3 Visible Spectra

A collection was taken to capture the full visible spectrum to see exactly what molecular and atomic structure was visible during the pulsed ablation. It was collected in a 1 Torr N_2 background with a 1.7 μs time delay, so no ionized species are expected to be seen this late. The spectrum is shown in Figure 26. The gaps that occur towards the red end of the spectrum are from missing wavelengths due to improperly moving the spectrometer during the experiment. Due to the very high resolution, only about 4 nm of the spectrum can be captured at once; however, the spectrometer grating was moved too far in between each shot, so parts of the spectrum are missing. The

C_2 Swan band and the CN Violet are well resolved. The $\Delta v = -2, -1, 0, +1, +2$ sequences of the C_2 Swan bands are all visible as well as the $\Delta v = 0, +1$ sequences of the CN Violet. Data collection focused mainly around the $\Delta v = 0$ sequences for
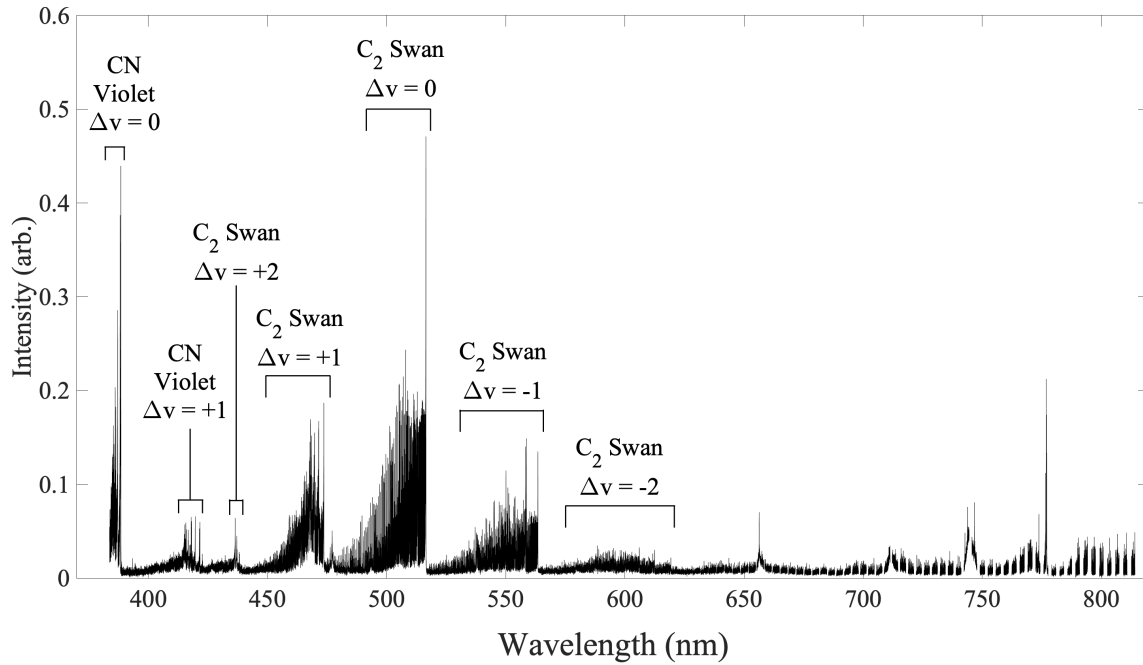
Figure 26. The full visible spectra is shown for 151 MW/cm^2 irradiation of graphite.

both the C_2 Swan and the CN Violet, and these were the areas that were used to compare against the spectral simulations.

4.4 Spectral Fits and Errors

The overall fitting process was previously described in Section 3.2; however, it is important to show and discuss a few example fits spanning the different background gases, time steps, and molecules in order to have an understanding of the error. There were many different sources of error involved in the fitting process, and each had varying degrees of importance. This section is going to look at those various sources as well as how they were mitigated.

40
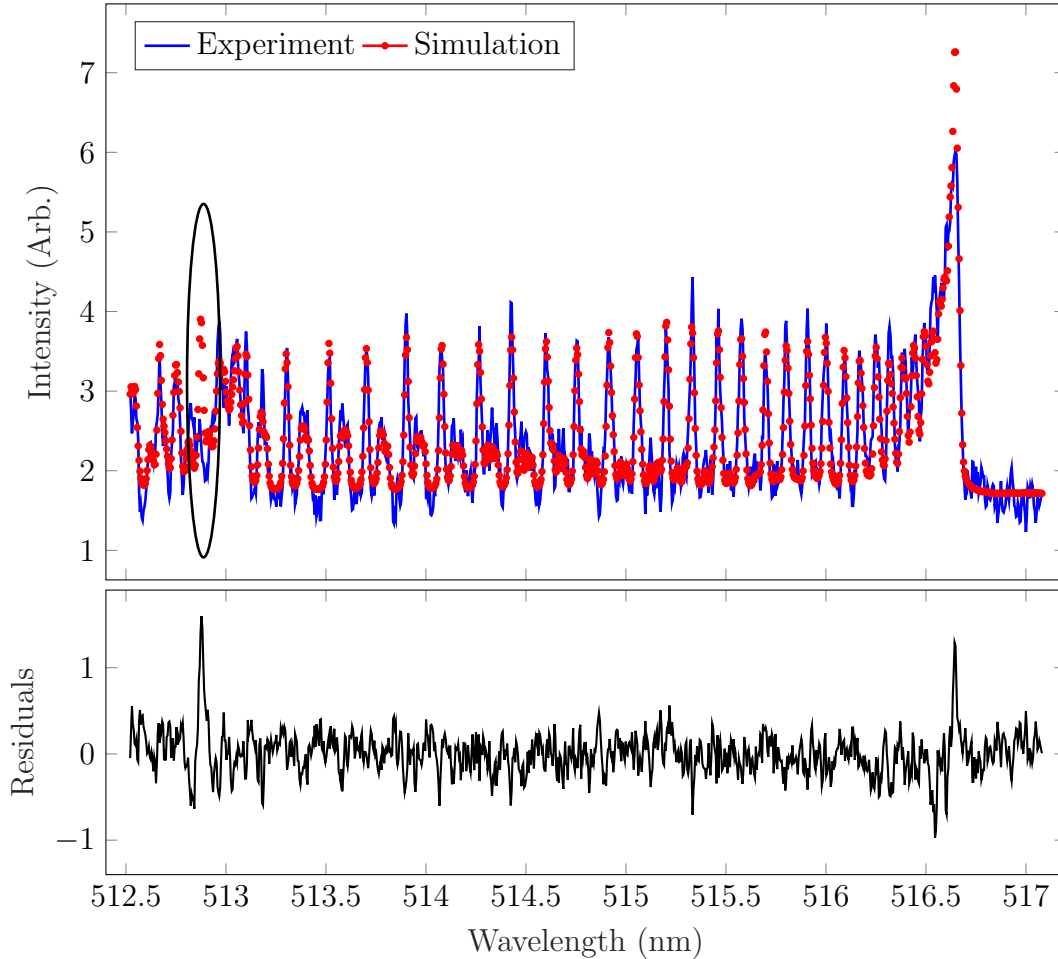
Figure 27. An example fitted C_2 Swan spectrum is shown here. It was taken t=0.34 μs after the laser irradiation, and the background gas was 10 Torr of Argon. The circled portion shows a common discrepency seen throughout all of the spectra, which corresponds to $P_1(49)$, $P_2(48)$, and $P_3(47)$ lines of the $(0,0)$ band.

Figure 27 shows a typical fit for the optical emission spectrum of the C_2 Swan $(0,0)$ band and $(1,1)$ band. Recall from Fortrat diagram in Figure 15 that only a part of the P branch of the $(1,1)$ band is within the frame for the spectral fits. At 512.9 nm, the lines corresponding all three fine-structure components of $N = 47$ level ($P_1(49)$, $P_2(48)$, and $P_3(47)$) of the $(0,0)$ band are not present in any of the experimental

41

data. This is most likely due to perturbations of the $d\ ^3\Pi_g$ state with the $b\ ^3\Sigma_g^-$ state [51]. Previous work suggests the $N = 47$ level of the $b\ ^3\Sigma_g^-$ is the perturbing state [65]. Although the perturbations were not added to the model, this small region of the spectra was excluded during the actual fitting procedures to ensure it would not influence the temperatures. It was also noted that the band heading was frequently lower in the experiment than in the simulation in early time steps. This was likely due to self-absorption in the plume, which was also seen in the first microsecond by Vivien et al [54]. The absorption effects are clearly strongest in the band head. This will affect the temperatures due to changing the relative intensities of the lines; however, the self-absorption does not last very long, so the assumption of an optically thin plume holds for the majority of the data.

Figure 28 shows multiple spectral fits at various time steps in the different background gases tested. It is easy to see the self-absorption is only an issue early on when comparing Figure 28(a) to the others. The previously discussed perturbation is also visible in each spectra as well. Towards 10 μs, the SNR becomes poor as visible in Figure 28(d). The spectrum is still barely visible, so the results from those fits will be included as well; however, as will be shown in the following sections, the error bars get increasingly large in the 7–10 μs range because of the poor SNR.

An example fit for the CN Violet spectrum is shown in Figure 29 with simulation temperatures of $T_R = 5,170\pm680$ K and $T_v = 10,040\pm1320$ K. Recall, the main bands are the (0,0), the (1,1), the (2,2), and the (3,3); however, as stated shown previously in Figure 16, partial bands up to the (10,10) band for the $\Delta v = 0$ sequence are visible in this spectral range. It is clear the residuals are higher compared to the C_2 Swan simulations; however, it should be noted that the rotational spacing of lines for the CN Violet spectra are much lower, and the sensitivity to the rotational and vibrational temperatures is lower as well. With these two issues combined, it becomes much more

42

Figure 28. Various C_2 Swan spectral fits and residuals. (a) Spectral fit at $t = 0.51$ μs in 10 Torr Ar. (b) Spectral fit at $t = 3.85$ μs in 10 Torr He. (c) Spectral fit at $t = 7.18$ μs in 10 Torr Air. (d) Spectral fit at $t = 10$ μs in 10 Torr N_2.

difficult to fit compared to the C_2 swan with the obtained spectral resolution from the experiment. Another potential issue is the longer gate width. With the radiative lifetimes of the excited states, there is a large degree of temporal averaging over the 500 ns gate width, which makes fitting for temperatures more complicated as well. All of these factors also resulted in the run time for fitting being quadrupled.

Similar to the C_2 Swan spectral fits, it is useful to look at a wide variety of the fits across both the different background gases as well as different time steps. Figure 30 displays four different spectral fits. Once again, the simulations overestimate the

43
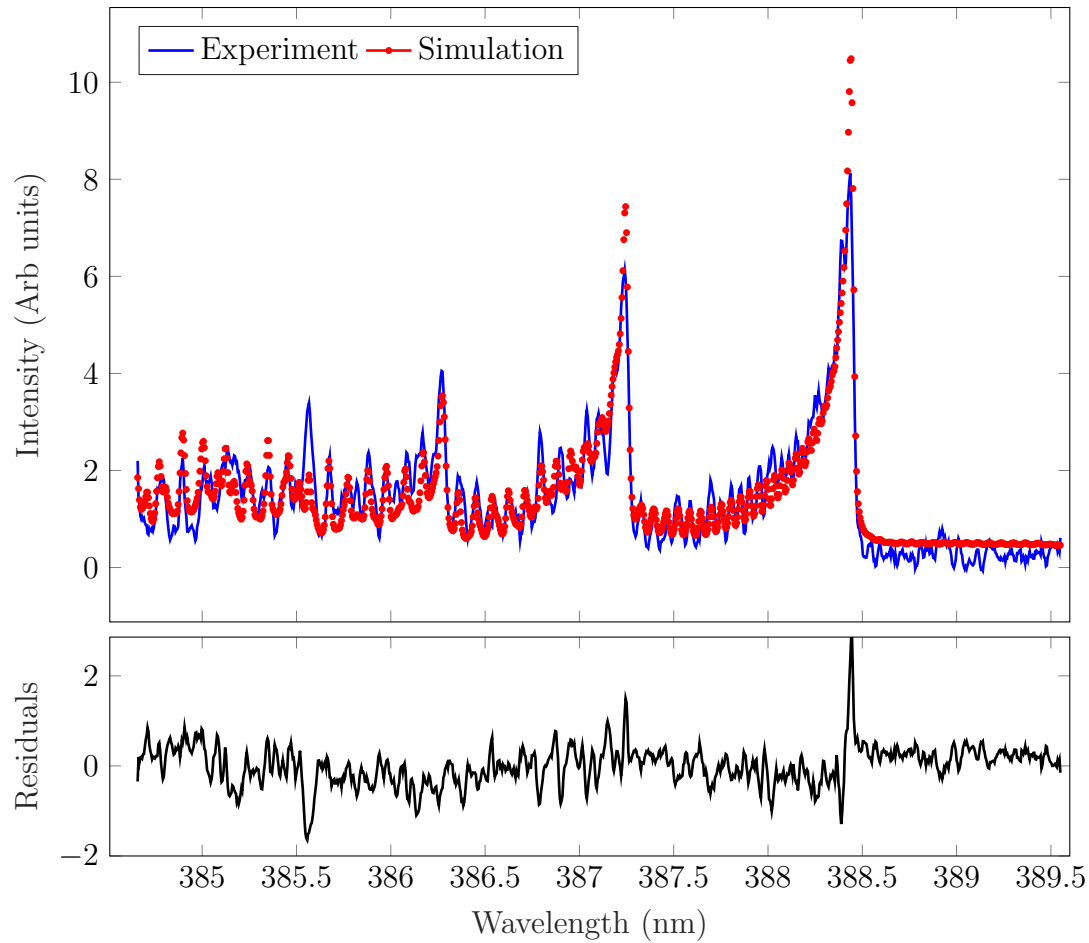
Figure 29. An example CN Violet fitted spectrum is shown here. It was taken t=0.77μs after the laser irradiation, and the background gas was 10 Torr of N_2. The simulation temperatures are $T_R = 5170 \pm 680$ K and $T_v = 10,040 \pm 1320$ K. The fits are more difficult due to the density of lines being much higher compared to the C_2 Swan.

band heads in the early time steps, which provides more evidence for the possible issue of self-absorption. This error is much lower for the CN Violet compared to the C_2, which is clear when comparing the two fits visually. However, it is still a source of systematic error early on in the fits. Overall, the fits display random error besides the discussed band head issues. It is also clear that the SNR ratio is much better than the C_2 Swan at 10 μs as shown by comparing Figure 30(d) with Figure 28(d). One way to see how well the model fits to the experimental data is to look at the mean square error (MSE) of the fits.
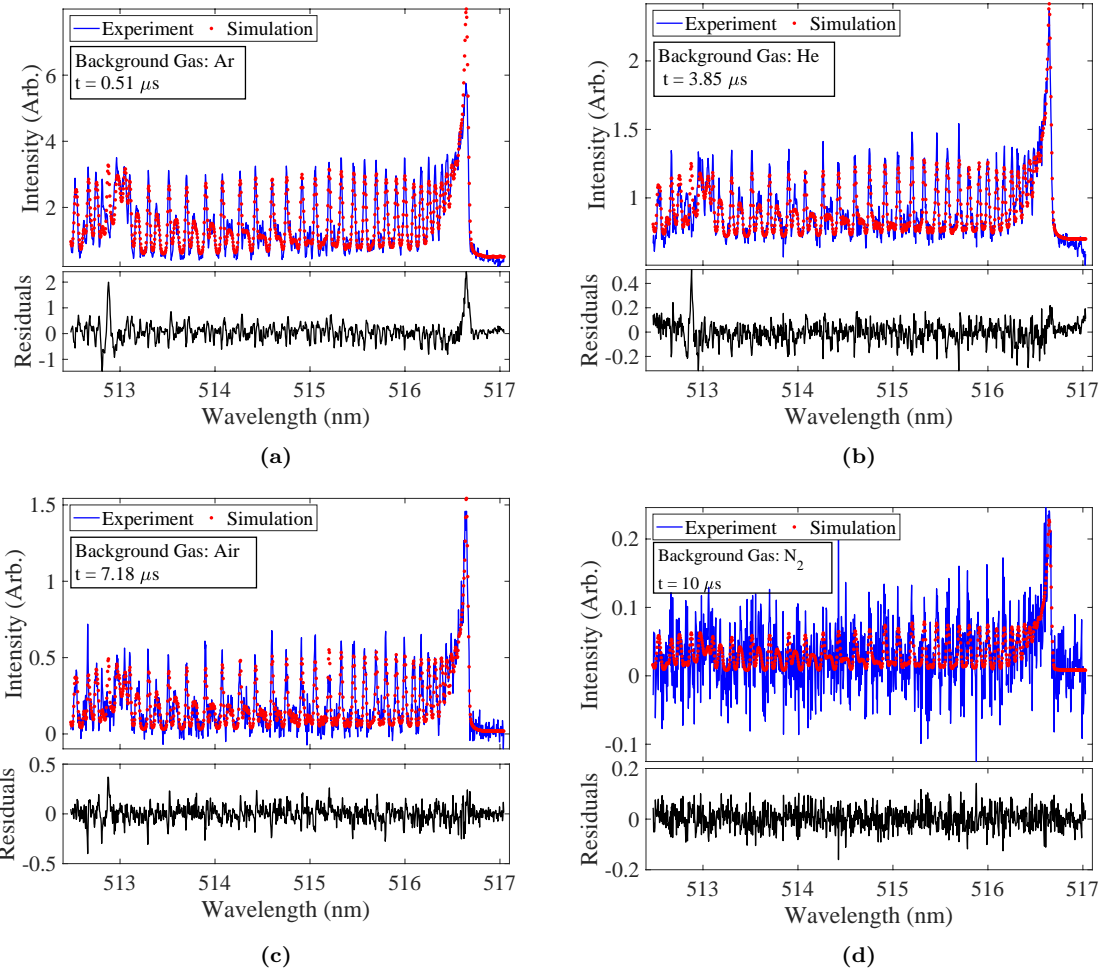
44
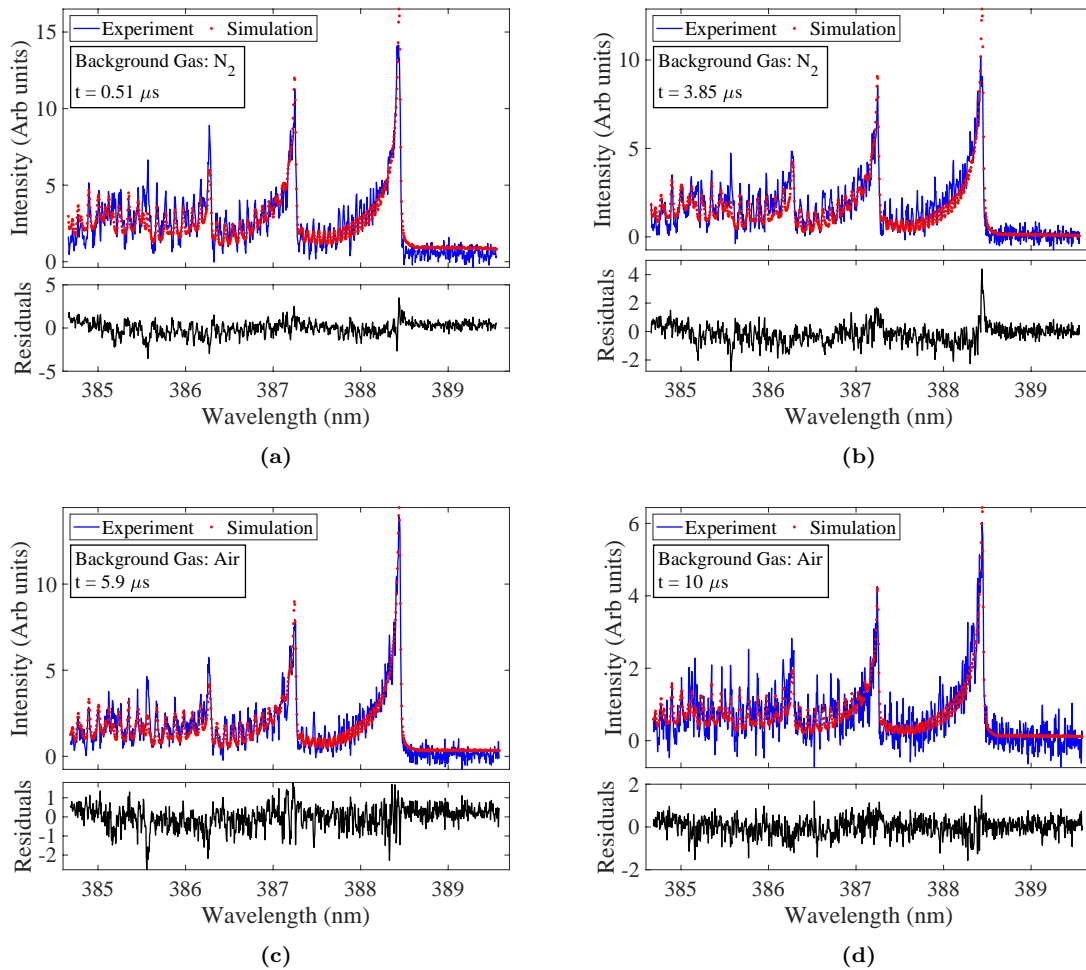
Figure 30. Various CN Violet spectral fits and residuals. (a) Spectral fit at $t = 0.51$ μs in 10 Torr N_2. (b) Spectral fit at $t = 3.85$ μs in 10 Torr N_2. (c) Spectral fit at $t = 5.9$ μs in 10 Torr Air. (d) Spectral fit at $t = 10$ μs in 10 Torr Air.

Figure 31 displays the MSE for each molecule in the various background gases. The MSE is scaled by the intensity to allow it to be compared across each time step. This was accomplished by dividing by the scale factor of each fit in order to account for the fact that the signal is brighter towards the beginning of the time sequence. Interestingly, the C_2 MSE displays this "U-shaped" like curve, while the CN MSE is relatively constant throughout the whole range. The shape of the C_2 MSE displays the effect of two of the larger errors that occurred during the fitting process: the self-absorption that drove more error in the initial fits and the low SNR that added

45
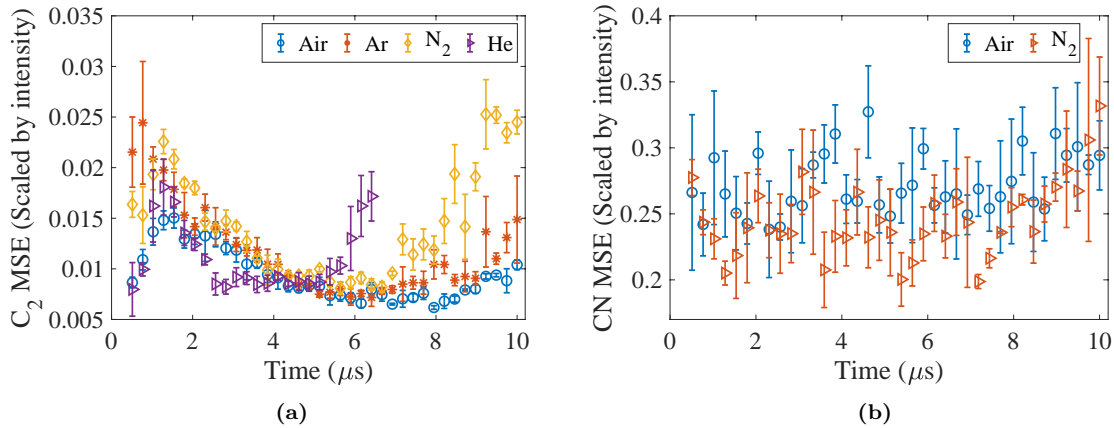
Figure 31. The mean square error for (a)C_2 Swan and (b)CN Violet spectral fits are displayed for $t = 0 - 10$ μs in each background gas.

error towards the later time steps. As we saw in Figure 30, the errors in the band heads of the CN spectral fits were much smaller compared to the initial band head error in the C_2 spectral fits, and the SNR was much better for the CN at time $t = 10$ μs. In addition to these types of fit errors, the experimental spectra can be skewed by random error in the data collection itself, which also merits discussion.

All of the test conditions (i.e. background gas/pressure) were collected multiple times. This enables us to look at the shot to shot variability and the random error in data collection. One of the large assumptions for the collection of the data was that each shot was essentially the same. For each test condition, three shots were collected at each time step. Figure 32 displays rotational and vibrational temperatures of both molecules for various backgound gases. There are only a few instances of outliers such as the first time step in Figure 32(b). Overall, the three tests constantly coincide with one another, which shows the shot to shot repeatability is good. It is important to once again note that although there are only three colors for visual purposes, each data point itself is from a single shot. Only one data point was collected per laser pulse, which gives even more merit to the consistency of the plots show in each part of Figure 32.

46
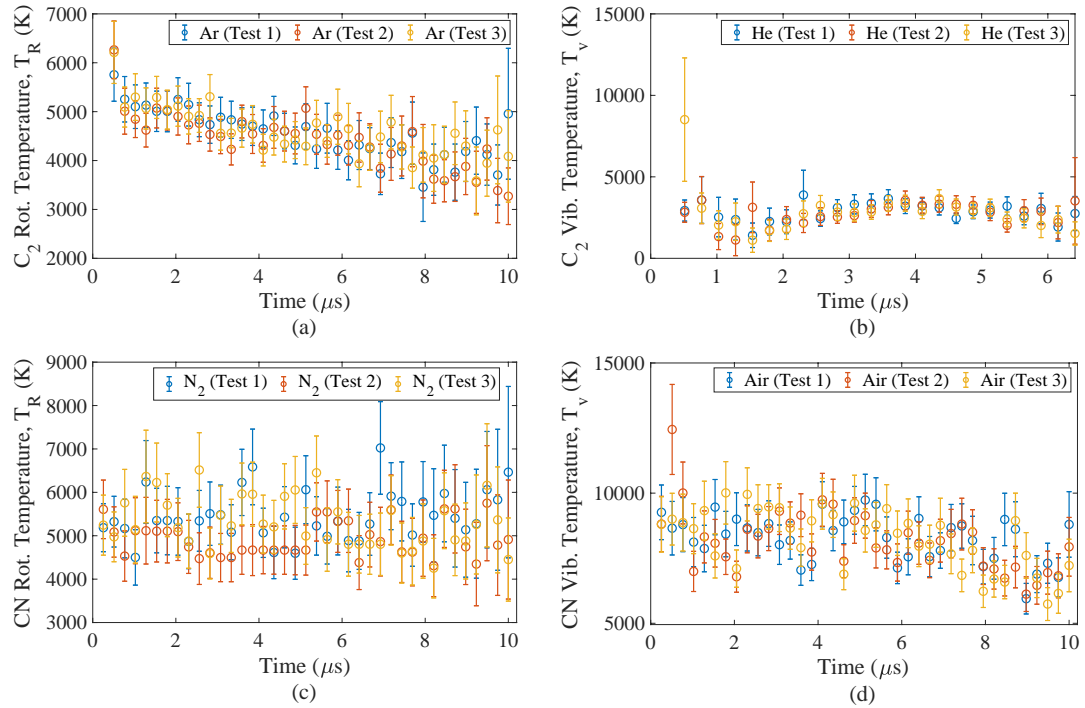
Figure 32. Various sets of tests are displayed to show the shot to shot variability in the extracted temperatures. (a) The C_2 rotational temperatures for 3 tests in an Ar background. (b) The C_2 vibrational temperatures for 3 tests in a He background. (c) The CN rotational temperatures for 3 tests in an N_2 background. (d) The CN vibrational temperatures for 3 tests in an Air background.

This naturally leads into the discussion of the error that will be displayed in the final plume temperature plots (Section 4.5). The error displayed in Figure 32 is the 95% confidence bound from the fitting routine, which provides a good estimation of how well the temperatures in the simulation fit the given experimental data; however, it does not naturally account for the experimental error from the actual data collection at all. This error from the fitting process is denoted σ_{fit}. There is a σ_{fit} associated with each single spectrum that was fit, so the average of the three single fit errors for a given time step is taken and called $\overline{\sigma}_{\text{fit}}$. However, since each collection was taken three times, the error between the three spectra at a single time step does give rise to an estimation of the experimental error (i.e. the standard deviation between the

47

three temperatures at a single time step). This error is denoted σ_{test}. In the final rotational and vibrational temperatures, we assume that these two types of error are independent of each other and can therefore be added in quadrature. This accounts for the confidence in the fit parameters themselves, but it also accounts for the error in the assumption that every shot is the same. Combing these two errors yields an equation for the error in temperature,

$$\delta T_i = \sqrt{(\overline{\sigma}_{\text{fit}})^2 + (\sigma_{\text{test}})^2} \tag{16}$$

where T_i is either the rotational temperature, T_R, or the vibrational temperature, T_v.
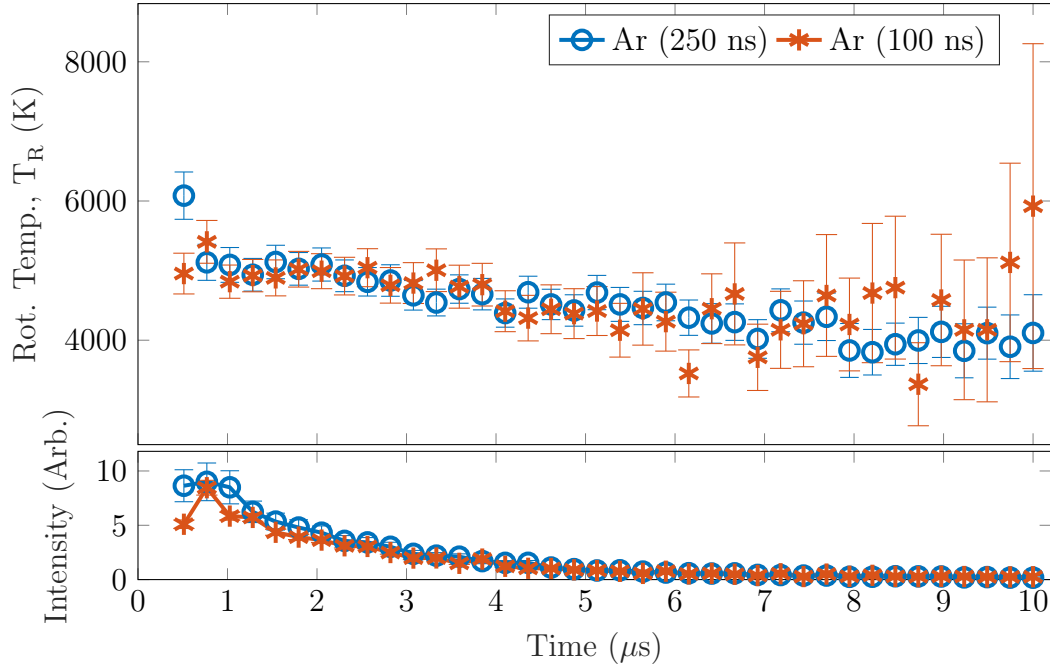
Figure 33. The rotational temperatures, T_R, for the C_2 Swan fits are shown for the background gas of 10 torr of Ar. The two lines are for the two gate widths used with the spectrometer. The gate width was shown to not affect the simulation temperatures.

Another potential source of error was the gate width. For the C_2 Swan spectra, the gate width for each collection was 250 ns, and for the CN Violet spectra, the gate width for each collection was 500 ns unless otherwise stated. The background gases

were air and N_2 This ensured enough light passed through the fiber to gather good spectra. This ensured enough light passed through the fiber to gather good spectra. The gate width could affect the simulation results because of temporal averaging, so a comparison was done between two gate widths. The background gas was argon at 10 torr for both collections, and 100 ns and 250 ns gate widths were used to compare the effects. The gate width was found to not have an immediate effect on the temperatures extracted from the simulations. The rotational temperatures for the two different gate widths along with their intensities are shown in Figure 33. Data for each time step was collected three times for each gate width, so the lines shown are the average of each set of three. As you can see, the error bars begin to increase towards the end of the time series (7-10 μs) due to the lack of signal in the 100 ns gate width. Besides this effect, the temperatures are the same. The gate width was not investigated for the CN Violet; however, similar results would be expected. With the errors and fitting process investigated, the actual temperature results can now be discussed.

4.5 Molecular Temperatures

Investigating the rovibrational temperatures of the C_2 Swan (0,0) band and the CN Violet $\Delta v = 0$ sequence was one of the main goals for this research. The temperatures coupled with the previously described plume imagery can provide key insights into the plume dynamics after the laser irradiation of graphite. Now that the fitting process and error has been detailed, the actually resulting plume temperatures for each molecule can be fully discussed.

The C_2 Swan rotational temperatures, T_R, for the various background gases (Air, Ar N_2, and He) are shown in Figure 34, and the vibrational temperatures, T_v, are shown in Figure 35. The temporal evolution of the rotational temperatures for each

49

Figure 34. The rotational temperatures from the C_2 Swan simulations are displayed for each background gas. The rotational temperatures are all the same within the error and have a decreasing linear trend. The trend of the intensity is drastically different for the experiments with helium as the background gas.

background gas is essentially the same. The rotational temperatures themselves appear to be fairly consistent with Park et al [53] and Saito et al [66], as they too decrease in approximately the same temperature range. The rotational temperatures of C_2 that were calculated in this study are essentially linearly decreasing with time. The fact that the background gas does not affect the rotational temperatures whatsoever is interesting, and this is inconsistent with the rotational temperatures calculated from Park et al [53].
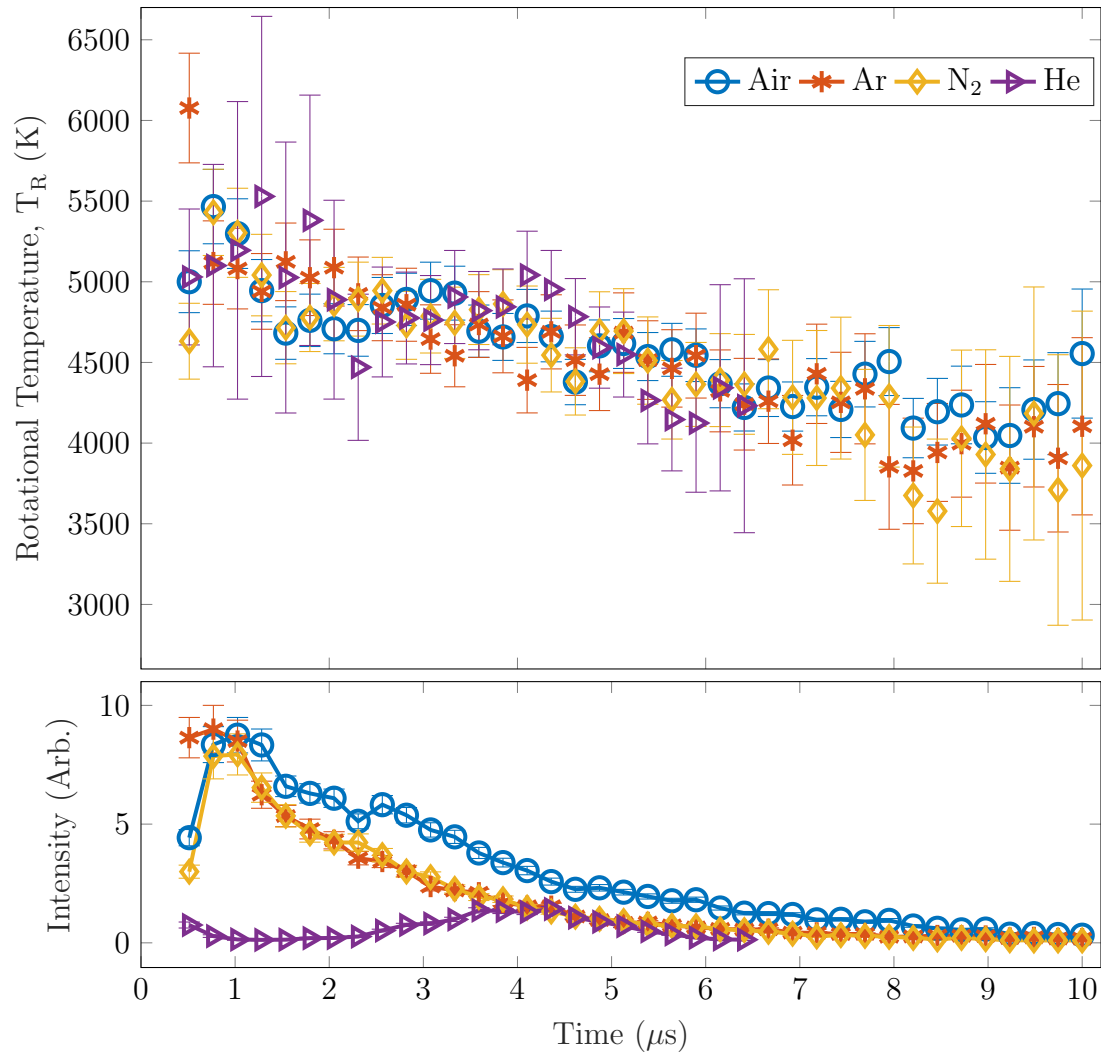
www.manaraa.com
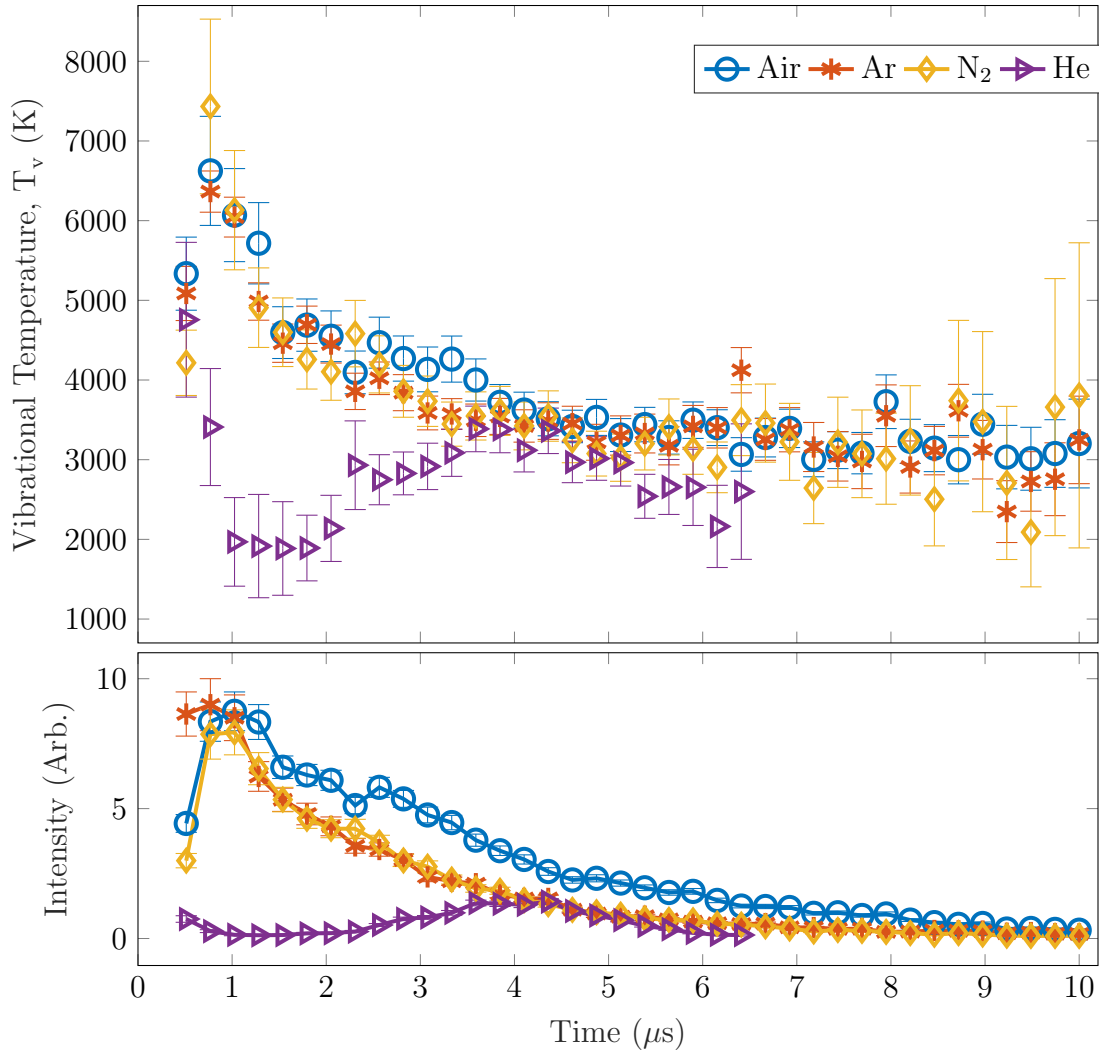
Figure 35. The vibrational temperatures from the C₂ Swan simulations are displayed for each background gas. The vibrational temperatures are all the same with the exception of the helium background gas. The trend is less linearly especially in the earlier times.

The intensity profile of the C₂ Swan in a helium background appears drastically different than the rest of the background gases. Recall from Section 4.1 and 4.2 that the plume propagation in helium is much different than the rest of the background gases. The peak intensity temporal location for Ar and N₂ is consistent with Park et al [53] who found the peak of both to occur at time $t = 1$ μs. In their work though, the shape of the helium intensity looked similar to the other background gases; whereas, Figure 34 suggests it is drastically different. This suggests that the

51

spectra are possibly dependent upon location relative to the shock front.

The vibrational temperatures are all the same except for in a helium background gas. The trend is more nonlinear for the vibrational temperatures as well. The vibrational temperatures are much lower than those found by Harilal et al [37]; however, the pressure used in their experiment was much lower at 50 mTorr. Ikegami et al found vibrational temperatures slightly higher as well with their temperatures only ranging from 8,000 K down to 5,000 K, and they reported that in an N_2 background (600 Torr), the vibrational temperatures were lower when compared to an argon background (600 Torr) [5].
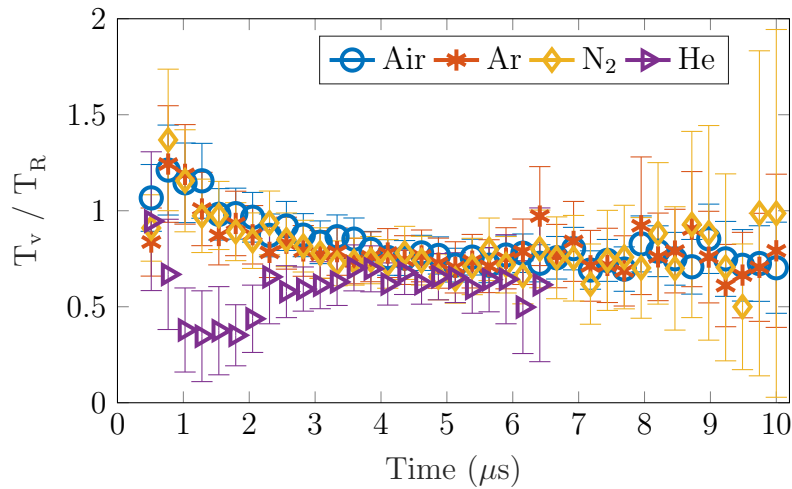
Figure 36. The temperature ratio (T_v/T_R) from the C_2 Swan simulation temperatures are displayed for each background gas. The ratio approaches approximately 0.78.

An interesting trend is uncovered when T_v/T_R is plotted. As time progresses, this ratio was expected to approach 1, as it approaches equilibrium; however, as shown in Figure 36, it dips slightly below 1 and approaches a ratio of 0.78. The error bars of the for Figure 36 are based on the standard uncertainty for a function of several

52

variables [67] as described in Equation 17

$$\delta\left(\frac{T_v}{T_R}\right) = \left(\left(\frac{\partial}{\partial T_v}\left(\frac{T_v}{T_R}\right)\delta T_v\right)^2 + \left(\frac{\partial}{\partial T_R}\left(\frac{T_v}{T_R}\right)\delta T_R\right)^2\right)^{\frac{1}{2}}$$

$$= \left(\left(\frac{1}{T_R}\delta T_v\right)^2 + \left(\frac{T_v}{T_R^2}\delta T_R\right)^2\right)^{\frac{1}{2}} \qquad (17)$$

The fact that the rotational and vibrational temperatures are not in equilibrium is particularly important for determining the mechanisms in which C_2 is formed. Nowhere has the phenomena with the He been seen previously.

Figure 37. The rotational temperatures from the CN Violet simulations are displayed for the Air and N_2 background gases. The rotational temperatures are higher in an N_2 background.

53

The rotational temperatures for the various CN Violet emission spectra are shown in Figure 37. As expected from the discussion in Section 4.4, the error bars are much worse in comparison to the C_2 simulations. The rotational temperatures of CN barely decrease during the time interval. The trendlines are the best fit for each background gas using a simple linear regression in order to provide a visual, and both show a slight decrease in temperature over time. In contrast to the C_2 Swan, there is a difference in temperatures between the background gases. Park et al found extremely different rotational temperatures ranging from 18,000 K down to 8,000 K and were found to steadily decrease over that range for similar pressures of N_2 [53].

The overall shape of the intensity of the CN Violet emissions looks different from previous studies as well [38, 47, 54]. Most intensity plots displayed in previous work have a single peak similar to the C_2 intensities shown previously. This could be due to the time scale, as most other work only spans a few microseconds at most.

The vibrational temperatures are shown in Figure 38. The vibrational temperatures are dramatically higher than the rotational temperatures in both background gases. Both are also much more time dependent than the rotational temperatures, but they do not vary as much as the temperatures found from CN simulations by Vivien et al [54]. It should be noted that a previous study resulted in the exact opposite, where the rotational temperatures were much higher than the vibrational temperatures [53]. However, a different study by Thareja et al. showed similar vibrational temperatures to the ones shown here [38]. The temperature ratio for the CN Violet is shown in Figure 39.

The temperature ratio fluctuates between 2 and 2.2, while dropping between 1.8 and 2 later in the time series. While the temperatures were different between the two different background gases, the ratios are indistinguishable. The fact that the ratio is far from 1 suggests it is not in local thermodynamic equilibrium, which is
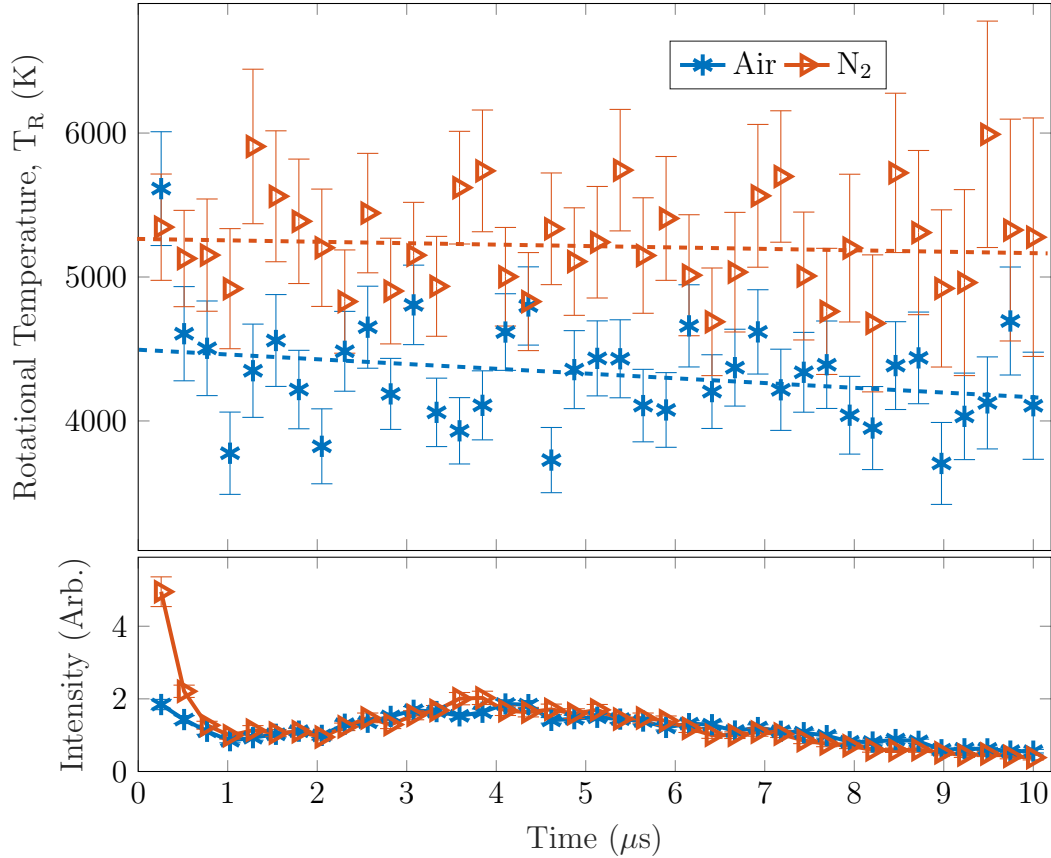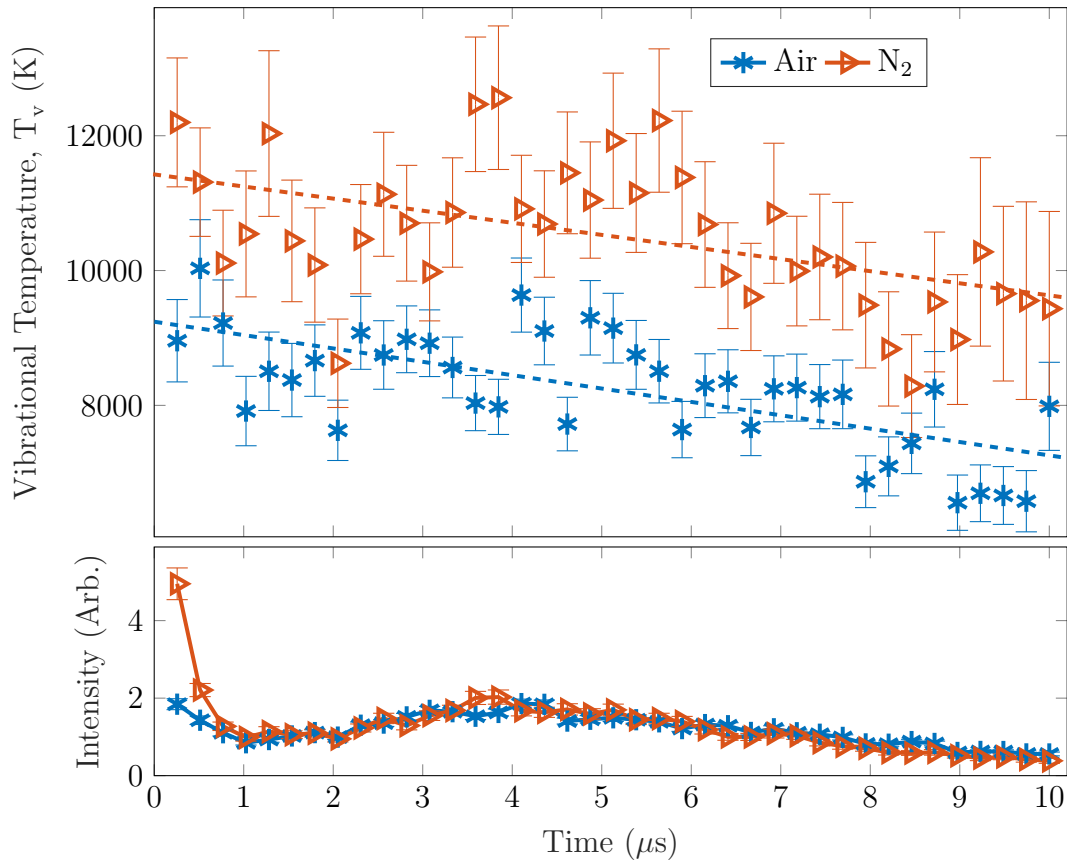
54

Figure 38. The vibrational temperatures from the CN Violet simulations are displayed for each background gas. The vibrational temperatures are much higher than the rotational temperatures. The vibrational temperatures are higher in an N_2 background. Both are decreasing with time.

once again extremely important for the discussion of formation mechanisms. The C_2 Swan temperature ratio is vastly different from the CN Violet ratio, although neither temperature ratio approaches 1.

While the C_2 Swan rovibrational temperatures did not depend on background gas besides helium, the CN Violet temperatures were background gas dependent between the air and nitrogen backgrounds. Figure 40 displays the intensity of the C_2 Swan emissions in comparison with the CN Violet emissions. The intensity is derived from the scale factor used in the fitting process. The C_2 emissions are much brighter than
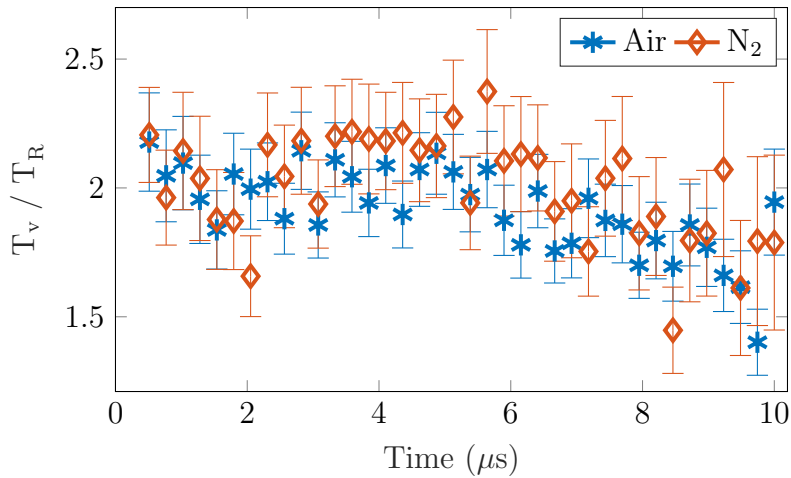
Figure 39. The temperature ratio (T_v/T_R) from the CN Violet simulation temperatures are displayed for both background gases. The ratio stays around 2 with a slight decrease towards the end of the time interval.
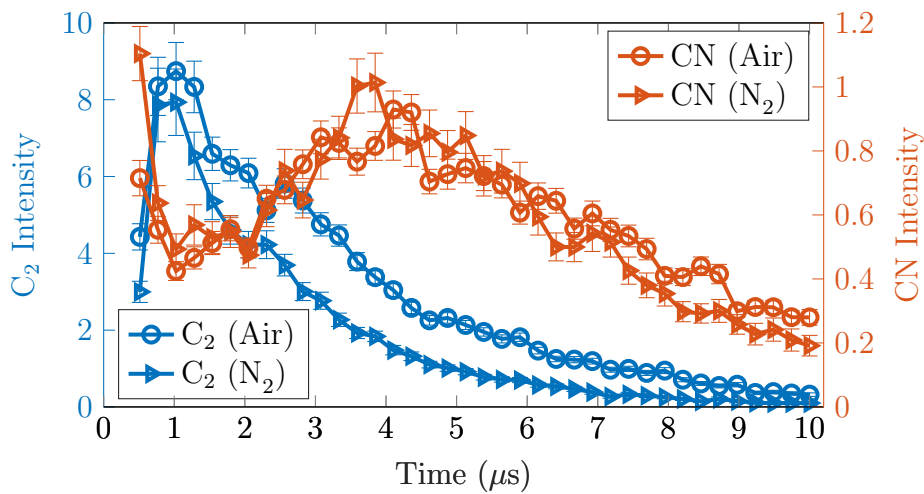
Figure 40. The intensities of both C_2 and CN are plotted for both air and nitrogen backgrounds. The C_2 intensity is plotted on the y axis on the left and is blue. The CN intensity is plotted on the y axis on the right and is orange.

the CN, so they are scaled differently. However, the trend is the interesting portion. The rise in intensity of the CN directly coincides with the fall in the C_2 intensity. This suggests that C_2 might play a role in the production of CN, which is consistent with previous research [35,38]. Another interesting feature is shown in Figure 41. The ratio of the two intensities which is proportional to their relative concentrations is plotted
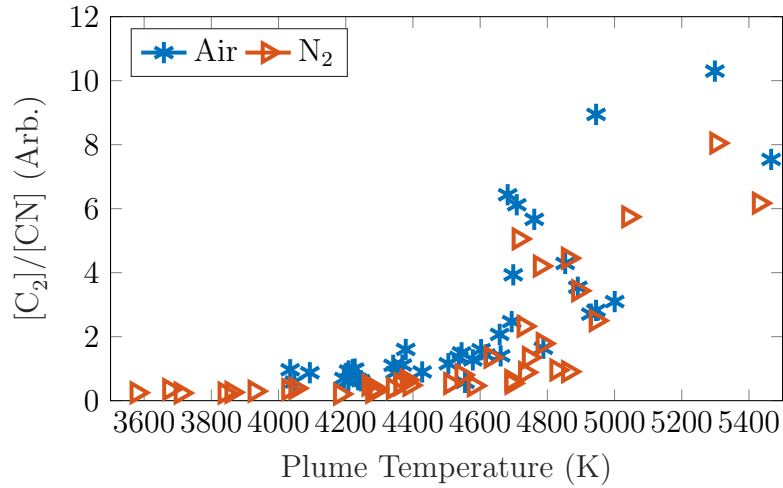
Figure 41. The intensity ratio of C_2 and CN is plotted for various plume temperatures. It is assumed that the rotational temperature of the C_2 molecular is a good estimate for the plume temperature. A strong temperature dependence between the two species is shown.

against the plume temperature. It is assumed that the rotational temperature of the C_2 is a good estimate of the plume temperature. A strong temperature dependence is shown, which has a similar shape compared to previous research [56].

V. Conclusions

The overarching goal of this research was to begin to piece together a convincing mechanism for the formation of C_2 and CN during the pulsed ablation of graphite. While it has been studied quite frequently in the past, there are largely inconsistent theories on what is truly happening in these high mach plumes as shown through the discussion in Section 4.5. The experimental analysis of this data is not confined to this type of work, as there are many fields that require a foundational approach to extracting rovibrational temperatures for not only C_2 Swan and CN Violet but for other spectra as well. The model that was developed can be applied to any portion of the C_2 Swan and CN Violet band systems can easily be adapted to other molecular band systems as well. The commercial and scientific communities such as thin film production and laser induced breakdown spectroscopy will benefit from the work done here as it serves to not only provide insights, but to also guide understanding and laboratory efforts. The key results will be highlighted in the following sections. Following that, a guide for future work will be laid out in order to aid those continuing these efforts.

5.1 Molecular Temperatures

The rovibrational temperatures for both the C_2 Swan (0,0) and (1,1) band as well as the CN Violet $\Delta v = 0$ sequence have been successfully extracted using models based in PGOPHER. The rotational temperatures for the C_2 Swan system varied from 6,000 K down to 3,700 K in a linear trend over $t = 0 - 10$ μs. The rotational temperatures did not depend on the background gas, nor did the vibrational temperatures. The vibrational temperatures varied less linearly from 7,000 K down to 3,000 K. The background gas did not matter except for the special case of helium

58

where the vibrational temperature decreased rapidly and then approached the temperatures with the other background gases. The temperature ratio for C_2 varied from 1.2 down to 0.78. The intensity of the C_2 Swan band was approximately an order of magnitude higher than the CN Violet. The decrease in inensity of C_2 relative to CN suggests that C_2 is involved in the mechanism of creating CN. The CN rotationaly temperatures were less time dependent compared to the C_2. However, there was an increase of approximately 700 K in the rotational temperature when the background gas was N_2 as opposed to air. The vibrational temperature increased by almost 2,000 K between the same two background gases. The vibrational temperature was much higher than the rotational temperature with the ratio hovering between 2.2 and 1.8 throughout the time interval. Although the temperatures were different between the two molecules, an important similarity was that neither of the two had rotational and vibrational temperatures in equilibrium, which is extremely important for understanding the mechanism.

5.2   Shock Front Analysis

Centerline intensities were used to calculate the shock front propagation of the plume resulting from the laser ablation of graphite. The plumes initial velocities were on average 1.46 cm/μs, which equates to anywhere from Mach 19 to Mach 57 depending on the background gas.The stopping distance in the drag model varied between 0.5 cm and 1.6 cm based upon the background gas and pressure. The drag model did a better job fitting the shock front expansion than the Taylor-Sedov model. Fitting the Taylor-Sedov model to the shock fronts gave an average n value of 2.74, which suggests the blast wave is somewhere between a spherical and cylindrical wave, which is to be expected given the laser profile. The C, C_2, and Ar filtered shock fronts all began to diverge from each other after 150 ns, and they were noticeably separated

at about 1 μs. The effects of background pressure on the plume's shock front was also investigated. The stopping distance was tripled when the background gas was lowered by a factor of 10, and the intial expansion velocity increased by about 20%. There are secondary shocks that develop in the data that were not analyzed, and it would require tweaking some theory to try to fit similar models and compare the results due to the plume splitting.

5.3   Recommendations Future Work

This work did a large amount of analyzing and processing the spectroscopic data; however, it created many more questions than answers. One foundational piece that was missing was CN filtered imagery. This will be key in understanding the location of CN formation relative to the shock, and a future experiment to look at that would be invaluable.

While optical emissions spectroscopy is a useful tool, it is limited in that no data is obtained on the non-emitting species. Another form of active spectroscopy could be a contribution to understanding the mechanism. Setting up an laser induced florescence or absorption experiment would provide a way to look at the ground state populations, which would aid in understanding the formation mechanisms.

Another possible experiment would be to reprocess the data using PGOPHER with numerical populations. There are ways to alter the PGOPHER model to accept numerical populations for each state. This would allow for possible non-equilibrium fitting of the spectra.

Setting up imagery that captures different orientations will help to investigate the v-shaped plume phenomena shown in Appendix C. It will be extremely important to understand this, since it fairly undocumented in the literature until recently.

If optical emissions spectroscopy were to be done again, moving the spectrometer

location would be another extremely important experiment. Having the spatially resolved data as well as the temporally resolved data would help to understand why the helium spectra looked so different from the other background gases, as it is potentially due to where the spectrometer FOV is relative to the shock front location.

Appendix A. Molecular Constants and Einstein A Coefficients for C_2 Swan and CN Violet PGOPHER Models

All of the molecular constants for the C_2 Swan and CN Violet models in PGO-PHER are displayed here, as well as the asssociated Einstein A coefficients that were used to calculate the transition moments. The C_2 Swan model used $v = 0 - 9$ vibrational states for the $a^3\Pi_u$ ground state and the $v = 0 - 10$ vibrational states for the $d^3\Pi_g$ electronic state. The CN Violet model used the $v = 0 - 15$ vibrational states for both the $X^2\Sigma^+$ and the $B^2\Sigma^+$ electronic states. The C_2 Swan molecular constants and Einstein A coefficients are displayed first, followed by the CN Violet molecular constants and Einstein A coefficients.

Table 9. Molecular constants for $a^3\Pi_u$ and $d^3\Pi_g$ states of C_2 used in the simulations. (Adapted from [51])

State	v	T_v	A	A_D	B	$D \times 10^6$	λ	o	p	q
$a^3\Pi_u$	0.......	0	-15.26912 (20)	0.0002388 (33)	1.6240451 (22)	6.45068 (84)	-0.15490 (25)	0.67539 (20)	0.002465 (24)	-0.0005319 (20)
	1.......	1618.02330 (31)	-15.25176 (27)	0.0002029 (32)	1.6074301 (20)	6.44478 (84)	-0.15355 (21)	0.66997 (21)	0.002697 (20)	-0.0005779 (18)
	2.......	3212.72262 (41)	-15.23388 (63)	0.0001684 (41)	1.5907615 (27)	6.4581 (18)	-0.15206 (50)	0.66308 (57)	0.003068 (33)	-0.0006472 (21)
	3.......	4784.1113 (31)	-15.2262 (52)	0.000106 (21)	1.574009 (12)	6.4573 (95)	-0.1592 (44)	0.6496 (44)	0.00352 (21)	-0.0007679 (76)
	4.......	6332.1373 (22)	-15.2031 (30)	0.000185 (17)	1.557175 (14)	6.444 (17)	-0.1448 (33)	0.6504 (30)	0.00527 (17)	-0.0008912 (71)
	5.......	7856.8242 (17)	-15.2009 (25)	0.000005 (13)	1.540145 (11)	6.349 (15)	-0.1443 (23)	0.6394 (20)	0.00646 (12)	-0.0012316 (55)
	6.......	9358.1728 (23)	-15.1586 (36)	0.000226 (17)	1.523437 (14)	6.101 (19)	-0.1416 (27)	0.6491 (28)	0.00403 (16)	-0.0006443 (73)
	7.......	10836.1550 (45)	-15.0856 (64)	0.00046 (15)	1.50875 (12)	3.05 (39)	-0.1478 (48)	0.6538 (65)	-0.0283 (14)	0.00685 (26)
	8.......	12290.903 (27)	-15.247 (57)	-0.00006 (10)	1.48789 (18)	3.71 (12)	-0.082 (36)	0.735 (43)	0.0033 (31)	-0.00202 (19)
	9.......	13722.1096 (33)	-15.0808 (53)	0.000482 (24)	1.472691 (21)	5.793 (40)	-0.1662 (20)	0.6516 (43)	0.00296 (32)	-0.000207 (18)
$d^3\Pi_g$	0.......	19378.46446 (30)	-14.00111 (28)	0.0004803 (37)	1.7455695 (20)	6.82103 (66)	0.03303 (20)	0.61085 (22)	0.003947 (20)	-0.0007762 (18)
	1.......	21132.13960 (13)	-13.87440 (24)	0.0005495 (43)	1.7254012 (25)	6.9647 (13)	0.03018 (27)	0.61703 (21)	0.004181 (25)	-0.0008310 (22)
	2.......	22848.4150 (30)	-13.8444 (49)	0.000655 (23)	1.704494 (13)	7.360 (11)	0.0108 (43)	0.6205 (43)	0.00431 (20)	-0.0009841 (69)
	3.......	24524.2222 (11)	-13.5329 (18)	0.000637 (11)	1.6814609 (79)	7.490 (11)	0.0515 (15)	0.5724 (14)	0.005213 (85)	-0.0008519 (40)
	4.......	26155.0003 (49)	-13.3557 (89)	0.000621 (28)	1.657484 (17)	8.095 (12)	0.0448 (55)	0.5382 (60)	0.00439 (23)	-0.0010884 (82)
	5.......	27735.6847 (26)	-13.0264 (47)	0.000582 (22)	1.630248 (15)	8.694 (18)	0.0823 (29)	0.5633 (32)	0.00541 (18)	-0.0008693 (70)
	6.......	29259.704 (14)	-13.082 (35)	0.00052 (fixed)	1.599841 (19)	9.0 (fixed)	0.062 (14)	0.559 (16)	0.00104 (65)	-0.001514 (17)
	7.......	30717.9217 (33)	-12.3299 (58)	0.000903 (28)	1.565922 (22)	9.787 (42)	0.0901 (20)	0.5127 (43)	0.00901 (30)	-0.001283 (15)
	8.......	32102.6713 (90)	-12.0890 (95)	0.00052 (fixed)	1.52672 (12)	9.58 (39)	0.046 (12)	0.4915 (96)	0.00457 (84)	-0.000863 (84)
	9.......	33406.325 (28)	-11.785 (66)	0.00052 (fixed)	1.48487 (18)	10.04 (14)	0.232 (43)	0.564 (49)	-0.0014 (28)	-0.00201 (20)
	10.......	34626.8093 (47)	-11.2469 (79)	0.00052 (fixed)	1.440994 (34)	12.544 (48)	0.1162 (65)	0.3578 (64)	0.00702 (47)	-0.001119 (20)

Table 10. Einstein $A_{v'v''}$ values for $d^3\Pi_g - a^3\Pi_u$ transitions used in the simulations. (Adapted from [40])

v''	v'										
	0	1	2	3	4	5	6	7	8	9	10
0	7.626 (+6)	2.814 (+6)	2.809 (+5)	4.333 (+3)	2.033 (+2)	3.642 (+1)	2.470 (-2)	2.140 (-1)	9.989 (-4)	3.827 (-3)	3.140 (-9)
1	2.135 (+6)	3.427 (+6)	4.072 (+6)	6.429 (+5)	8.720 (+3)	1.608 (+3)	1.591 (+2)	2.744 (+0)	1.822 (+0)	4.947 (-2)	3.540 (-2)
2	3.832 (+5)	2.746 (+6)	1.270 (+6)	4.422 (+6)	9.615 (+5)	7.432 (+3)	6.154 (+3)	3.223 (+2)	6.379 (+1)	4.108 (+0)	1.567 (+0)
3	5.590 (+4)	8.273 (+5)	2.568 (+6)	3.236 (+5)	4.301 (+6)	1.168 (+6)	1.085 (+3)	1.805 (+4)	1.707 (+2)	3.472 (+2)	1.346 (-2)
4	7.224 (+3)	1.710 (+5)	1.169 (+6)	2.066 (+6)	2.505 (+4)	4.005 (+6)	1.149 (+6)	4.993 (+3)	3.581 (+4)	1.535 (+2)	9.452 (+2)
5	8.592 (+2)	2.886 (+4)	3.215 (+5)	1.352 (+6)	1.510 (+6)	1.513 (+4)	3.459 (+6)	1.120 (+6)	5.272 (+4)	4.975 (+4)	4.445 (+3)
6	9.574 (+1)	4.280 (+3)	6.793 (+4)	4.745 (+5)	1.381 (+6)	1.038 (+6)	8.028 (+4)	3.438 (+6)	8.558 (+5)	1.863 (+5)	4.075 (+4)
7	1.006 (+1)	5.775 (+2)	1.218 (+4)	1.218 (+5)	6.009 (+5)	1.302 (+6)	6.443 (+5)	1.343 (+5)	3.253 (+6)	4.834 (+5)	4.111 (+5)
8	9.931 (-1)	7.206 (+1)	1.945 (+3)	2.582 (+4)	1.830 (+5)	6.840 (+5)	1.087 (+6)	4.546 (+5)	1.285 (+5)	3.081 (+6)	1.342 (+5)
9	9.005 (-2)	8.335 (+0)	2.828 (+2)	4.785 (+3)	4.495 (+4)	2.421 (+5)	6.721 (+5)	9.993 (+5)	3.120 (+5)	8.080 (+4)	2.824 (+6)

Table 11. for $X^2\Sigma^+$ and $B^2\Sigma^+$ states of CN used in the simulations. (Adapted from [52])

State and Equilibrium Constants	v	T_v	B_v	$D_v \times 10^5$	H_v	γ_v	γ_{D_v}
	0	0	1.891090248(84)	0.640771(18)	6.277(17)E-12	7.25393(56)E-3	-9.1(11)E-9
	1	2042.42135(11)	1.873665679(78)	0.641647(18)	5.984(17)E-12	7.17190(82)E-3	-1.12(12)E-8
	2	4058.54930(11)	1.856187457(76)	0.642639(18)	5.678(18)E-12	7.0801(12)E-3	-1.75(15)E-8
$X^2\Sigma^+$	3	6048.34449(17)	1.83865289(13)	0.643809(23)	5.510(34)E-12	6.9798(14)E-3	-2.43(36)E-8
$\omega_e = 2068.68325(99)$	4	8011.76770(17)	1.82105955(22)	0.645051(29)	5.204(52)E-12	6.8636(16)E-3	-3.67(52)E-8
$\omega_e x_e = 13.12156(45)$	5	9948.77678(17)	1.80340446(25)	0.646440(35)	5.014(91)E-12	6.7213(16)E-3	-5.87(76)E-8
$\omega_e y_e = -0.005426(74)$	6	11859.32865(19)	1.78568518(26)	0.647525(51)	...	6.5456(17)E-3	...
$\omega_e z_e = -9.82(40)$E-5	7	13743.37581(21)	1.76789886(23)	0.649207(93)	...	6.3134(16)E-3	...
$B_e = 1.8997872(28)$	8	15600.87043((26)	1.75004067(30)	0.65094(18)	...	6.0118(18)E-3	...
$\alpha_1 = -0.0173802(27)$	9	17431.75566(40)	1.73210142(28)	0.65297(56)	...	5.6130(25)E-3	...
$\alpha_2 = -2.235$ (69)E-5	10	19235.96013(45)	1.71404986(30)	0.66358(75)	...	5.2324(30)E-3	...
$\alpha_3 = -6.64(48)$ E-7	11	21013.29410(84)	1.695088(22)	0.192(14)	-9.19(23)E-9	1.434(16)E-2	-8.111(76)E-5
$r_e(\mathring{A}) = 1.17180630(86)$	12	22765.7282(10)	1.677608(27)	1.231(21)	1.099(47) E-8	1.3297(18)E-1	-2.274(11)E-4
	13	24488.7305(13)	1.659501(23)	0.6610(68)	...	1.777(20)E-2	...
	14	26185.6928(18)	1.641413(46)	0.742(27)	...	1.179(25)E-2	...
	15	27856.2000	1.62261(12)	0.617(46)	...	3.5(17)E-3	...
	0	25797.87041(49)	1.9587206(15)	0.659524(62)	...	1.7153(60)E-2	-6.81(31)E-7
	1	27921.46673(58)	1.9380395(52)	0.67308(33)	...	1.8162(95)E-2	-8.96(93)E-7
$B^2\Sigma^+$	2	30004.90702(83)	1.916503(12)	0.7031(32)	...	1.839(15)E-2	-2.40(69)E-6
$T_e = 25752.590(12)$	3	32045.94782(75)	1.894182(17)	0.7115(69)	...	2.453(18)E-2	-7.3(13)E-6
$\omega_e = 2162.223(30)$	4	34041.97171(62)	1.8704798(76)	0.7451(17)	...	2.117(11)E-2	-5.18(41)E-6
$\omega_e x_e = 19.006(22)$	5	35990.0982(24)	1.847108(28)	0.9139(61)	...	4.27(96)E-3	1.693(45)E-4
$\omega_e y_e = -0.1346(65)$	6	37887.42564(54)	1.8193419(61)	0.8099(12)	...	2.524(10)E-2	-8.53(31)E-6
$\omega_e z_e = -0.03673(85)$	7	39730.53557(59)	1.790760(14)	1.1049(67)	...	6.098(67)E-3	...
$\omega_e \eta_e = 0.001430(37)$	8	41516.64447(62)	1.7621439(66)	0.9058(14)	...	3.488(11)E-2	-1.985(36)E-5
$B_e = 1.96797(41)$	9	43242.98520(78)	1.730286(14)	0.9254(67)	...	1.576(12)E-2	-1.937(41)E-5
$\alpha_1 = -0.01881(18)$	10	44908.7939(11)	1.696076(40)	0.313(40)	...	2.4897(38)E-1	-1.7970(62)E-3
$\alpha_2 = -0.000643(16)$	11	46511.39737(85)	1.664979(12)	1.0253(31)	...	2.161(16)E-2	-1.866(62)E-5
$r_e(\mathring{A}) = 1.15133(12)$	12	48053.7308(11)	1.629785(33)	1.846(22)	...	-9.17(26)E-3	-7.56(25)E-5
	13	49537.3409(13)	1.598044(22)	1.0871(61)	...	3.344(25)E-2	-2.565(72) E-5
	14	50964.5889(26)	1.564126(94)	1.207(41)	...	3.49(49)E-3	...
	15	52340.0287(20)	1.53238(13)	1.220(60)	...	8.61(17)E-2	-2.334(28)E-4

Table 12. Einstein $A_{v'v''}$ values for $B^2\Sigma^+ - X^2\Sigma^+$ transitions used in the simulations. (Adapted from [52])

v''	v'															
	0	1	2	3	4	5	6	7	8	9	10	11	12	13	14	15
0	1.50E+07	1.61E+06	2.24E+04	3.04E+02	3.22E+01	7.10E-02	8.17E-05	8.69E-03	2.43E-04	2.21E-04	2.39E-03	5.53E-03	2.94E-03	5.05E-06	3.06E-03	5.61E-03
1	9.41E+05	1.25E+07	2.89E+06	4.82E+04	2.00E+03	1.51E+02	1.89E+00	6.04E-04	5.64E-02	9.67E-03	4.46E-02	1.34E-02	3.08E-04	1.06E-03	2.80E-03	3.26E-03
2	4.34E+04	1.65E+06	1.05E+07	3.85E+06	6.21E+04	7.36E+03	3.79E+02	1.66E+01	3.35E-01	6.12E-02	3.15E-05	7.72E-02	3.35E-02	1.63E-04	3.96E-03	3.67E-03
3	1.61E+03	1.21E+05	2.12E+06	8.93E+06	4.52E+06	5.47E+04	2.00E+04	5.49E+02	9.12E+01	1.13E+00	1.47E-03	1.19E-01	4.65E-02	1.29E-01	2.90E-02	1.98E-04
4	6.07E+01	6.11E+03	2.18E+05	2.39E+06	7.76E+06	4.93E+06	2.90E+04	4.35E+04	3.74E+02	3.52E+02	1.86E-01	7.17E-01	3.04E-01	5.11E-03	2.00E-01	1.58E-01
5	2.63E+00	2.71E+02	1.42E+04	3.21E+05	2.49E+06	6.94E+06	5.08E+06	2.85E+03	7.86E+04	3.13E-01	9.33E+02	9.52E+00	4.97E+00	2.84E-02	3.20E-01	4.18E-02
6	6.24E-02	1.26E+01	7.42E+02	2.57E+04	4.18E+05	2.45E+06	6.43E+06	4.98E+06	1.41E+04	1.19E+05	1.57E+03	1.67E+03	1.35E+02	7.56E+00	1.51E+00	5.58E-01
7	2.67E-03	4.26E-01	3.67E+01	1.56E+03	3.96E+04	4.98E+05	2.30E+06	6.18E+06	4.60E+06	1.18E+05	1.47E+05	1.10E+04	1.76E+03	6.59E+02	2.87E-02	1.13E+01
8	3.87E-03	1.98E-03	1.36E+00	8.04E+01	2.75E+03	5.44E+04	5.59E+05	2.06E+06	6.15E+06	3.95E+06	3.75E+05	1.39E+05	3.66E+04	4.94E+02	1.74E+03	9.18E+01
9	5.85E-04	1.86E-02	2.69E-03	3.16E+00	1.51E+02	4.31E+03	6.78E+04	5.97E+05	1.76E+06	6.30E+06	3.05E+06	8.17E+05	8.24E+04	8.04E+04	8.19E+02	2.50E+03
10	1.44E-05	6.77E-03	6.00E-02	4.02E-05	6.25E+00	2.52E+02	6.09E+03	7.78E+04	6.17E+05	1.42E+06	6.54E+06	1.98E+06	1.40E+06	1.20E+04	1.24E+05	1.28E+04
11	5.33E-11	8.99E-04	2.52E-02	1.18E-01	4.04E-03	1.06E+01	3.77E+02	7.89E+03	8.27E+04	6.22E+05	1.06E+06	6.75E+06	9.41E+05	1.96E+06	2.63E+04	1.29E+05
12	2.82E-07	3.30E-05	3.75E-03	6.53E-02	1.99E-01	1.83E-02	1.62E+01	5.17E+02	9.48E+03	8.11E+04	6.21E+05	7.14E+05	6.79E+06	1.96E+05	2.24E+06	2.51E+05
13	8.22E-08	2.45E-07	1.75E-04	1.32E-02	1.39E-01	3.03E-01	4.45E-02	2.22E+01	6.45E+02	1.07E+04	7.27E+04	6.19E+05	4.19E+05	6.49E+06	2.04E+04	2.04E+06
14	–	2.37E-07	1.51E-08	1.01E-03	3.58E-02	2.48E-01	4.29E-01	5.16E-02	2.74E+01	7.29E+02	1.14E+04	5.83E+04	6.24E+05	2.02E+05	5.77E+06	5.34E+05
15	–	–	8.83E-07	9.44E-06	3.93E-03	7.75E-02	4.13E-01	6.11E-01	1.84E-02	3.07E+01	7.36E+02	1.17E+04	3.99E+04	6.37E+05	7.27E+04	4.64E+06

Appendix B. Error Analysis for Shock Models

The details of the error analysis for the various parameters of the Taylor-Sedov model and the drag model are detailed below. First, the Taylor-Sedov model is treated followed by the drag model.

2.1   Taylor-Sedov Model

The Taylor-Sedov model is described below:

$$R(t) = \xi \left(\frac{E}{\rho_b} \right)^{\frac{1}{n+2}} t^{\frac{2}{n+2}}$$

For the purposes of fitting, we can simplify it to $R = at^b$ where $a = \xi \left(\frac{E}{\rho_b} \right)^{\frac{1}{n+2}}$ and $b = 2/(n+2)$. Thus, the error in $\xi \left(\frac{E}{\rho_b} \right)^{\frac{1}{n+2}}$ is simply the error in a, but the error in n is slightly different. First, rearranging to solve for n in terms of b yields

$$n = \frac{2}{b} - 2$$

Therefore, the error in n is

$$\delta n = \frac{\partial n}{\partial b} \delta b = \frac{2}{b^2} \delta b \tag{18}$$

2.2   Drag Model

The drag model is described by

$$R(t) = R_s (1 - e^{-kt})$$

where R_s is the stopping distance and k is the slowing term. We know from Section 2.2 that the initial velocity is simple $v_0 = kR_s$. When fitting the drag model R_s gets

67

fit directly so there is no need to propagate its error. However, the error propagation for v_0 is as follows

$$\delta v_0 = \left[\left(\frac{\partial v_0}{\partial R_s}\delta R_s\right)^2 + \left(\frac{\partial v_0}{\partial k}\delta k\right)^2\right]^{\frac{1}{2}}$$
$$= \left[(k\delta R_s)^2 + (R_s\delta k)^2\right]^{\frac{1}{2}}$$

Appendix C. Plume Reversal

This section is meant to detail a phenomena only recently seen in the imagery data. In some background gases, the plume seems to reverse direction and head back towards the graphite target. This feauture is most prominent in a helium background. The V-shape structure was just only recently published by another research group. This appendix serves as documentation that a similar structure was seen in our experiments as well.

(a) $t = 1.27$ μs

(b) $t = 1.53$ μs

(c) $t = 2.36$ μs

(d) $t = 3.44$ μs

(e) $t = 4.06$ μs

(f) $t = 4.89$ μs

(g) $t = 5.49$ μs

(h) $t = 6.30$ μs

70
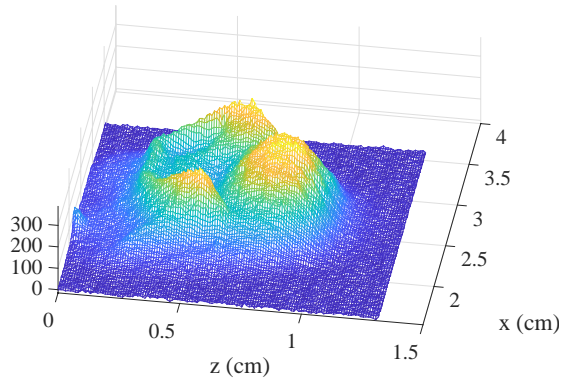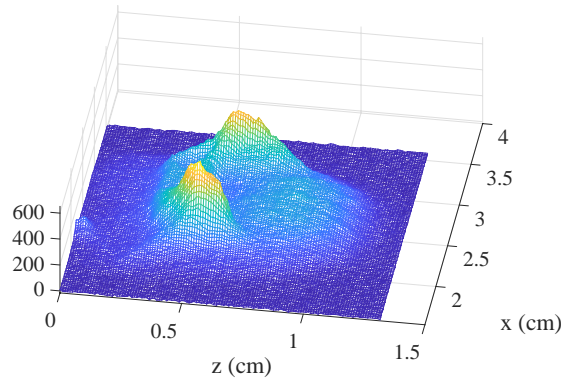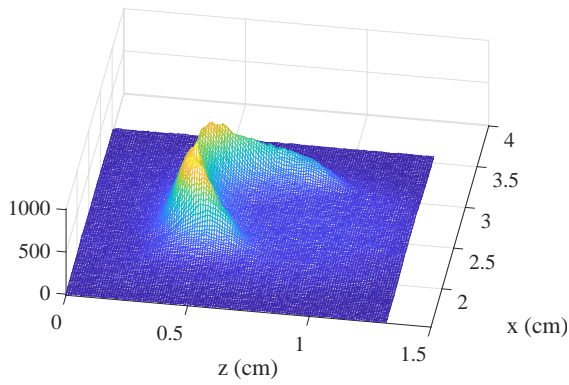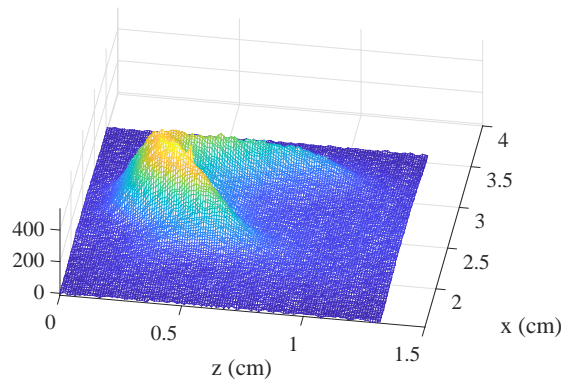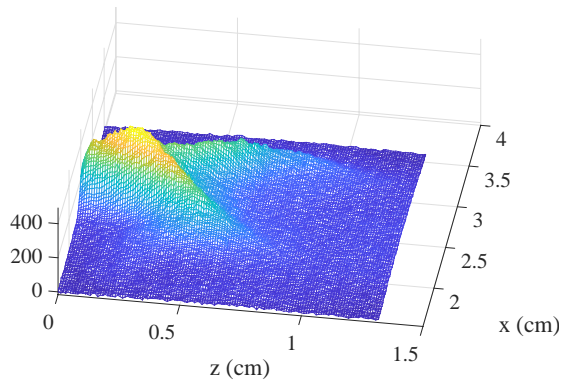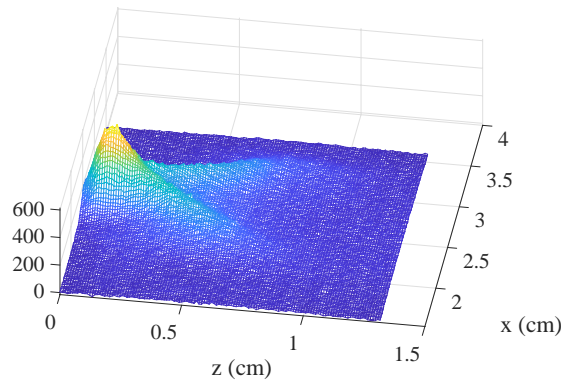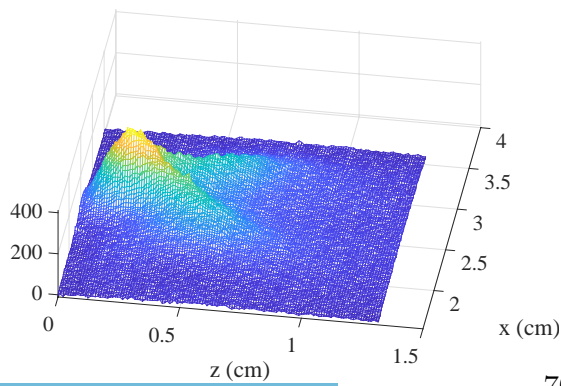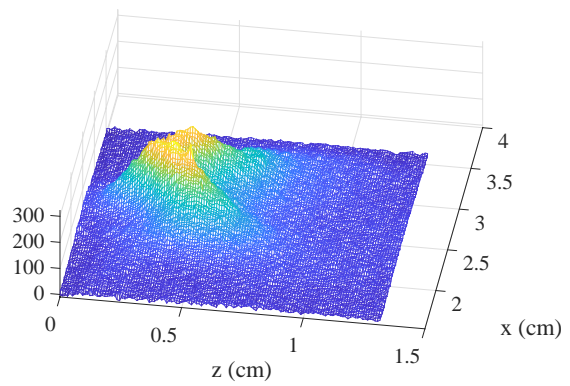
Figure 42

Appendix D. Shock Front Fits

The shock front fits from the ICCD imagery mentioned in Section 4.2 are presented here. The filter and background gases for the shock fronts not shown previously, and the corresponding figure numbers are:

Figure 43: No filter and 10 Torr Air background

Figure 44: 520 nm filter and 10 Torr Air background

Figure 45: 830 nm filter and 10 Torr Air background

Figure 46: No filter and 10 Torr Ar background

Figure 47: 520 nm filter and 10 Torr Ar background

Figure 48: 830 nm filter and 10 Torr Ar background

Figure 49: No filter and 10 Torr He background

Figure 50: 520 nm filter and 10 Torr He background

Figure 51: 830 nm filter and 10 Torr He background

Figure 52: No filter and 1 Torr N_2 background

Figure 53: No filter and 10 Torr N_2 background

Figure 54: 520 nm filter and 10 Torr N_2 background

Figure 55: 830 nm filter and 10 Torr N_2 background

Figure 56: No filter and vacuum

Figure 57: 520 nm filter and vacuum

Figure 58: 830 nm filter and vacuum
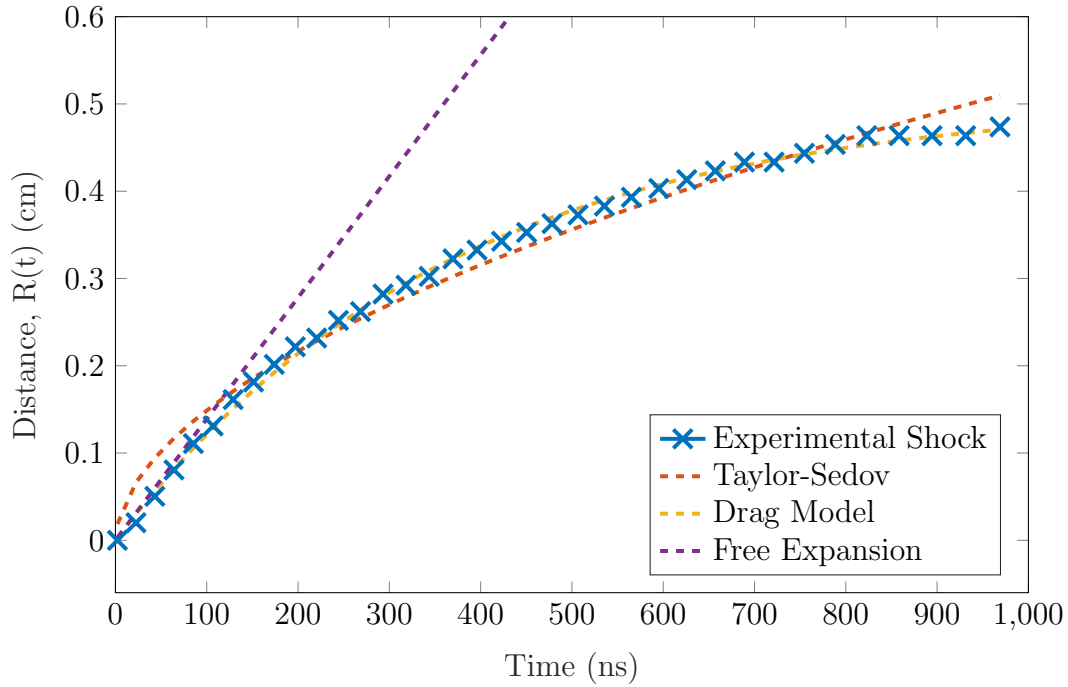
Figure 43. The shock front propagation is shown for an air background pressure of 10 Torr with no filter on the ICCD array.
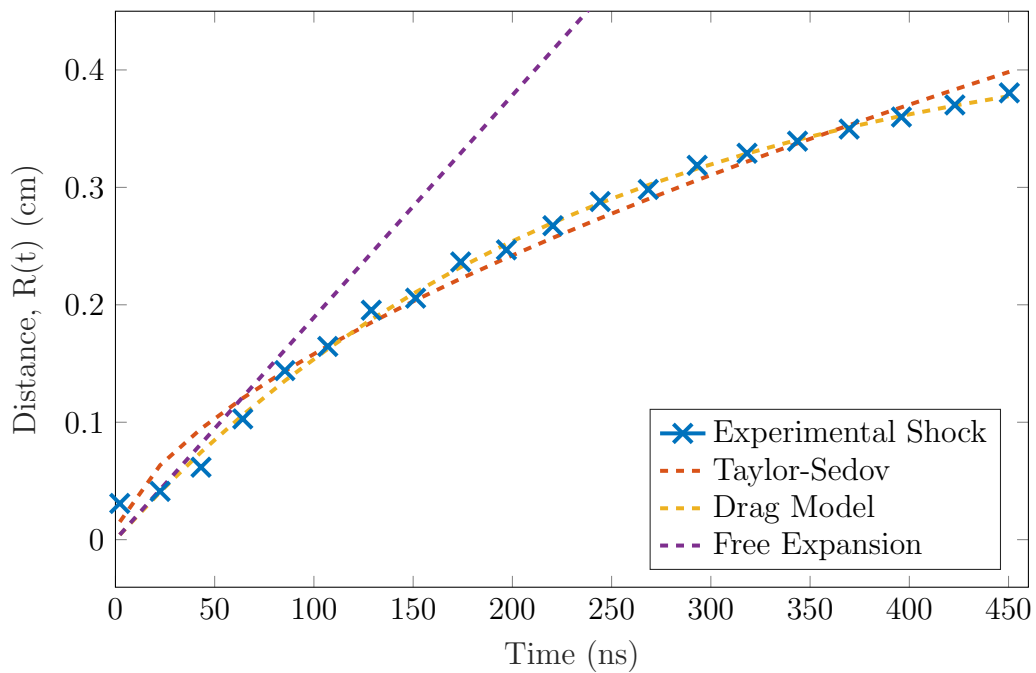

Figure 44. The shock front propagation is shown for an air background pressure of 10 Torr with a 520 nm filter on the ICCD array.
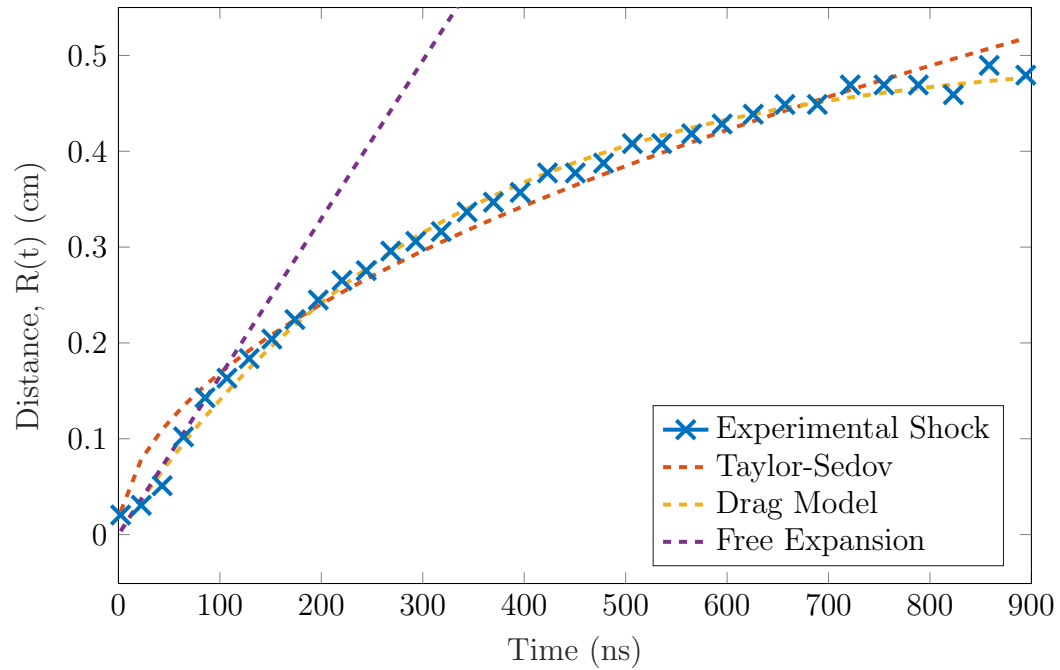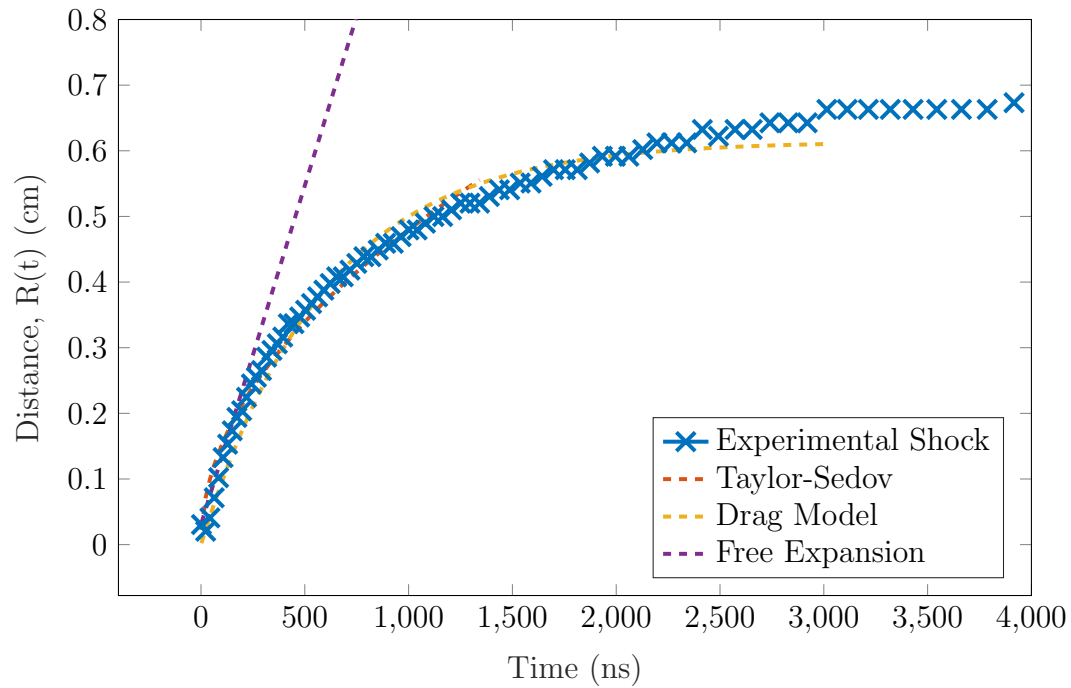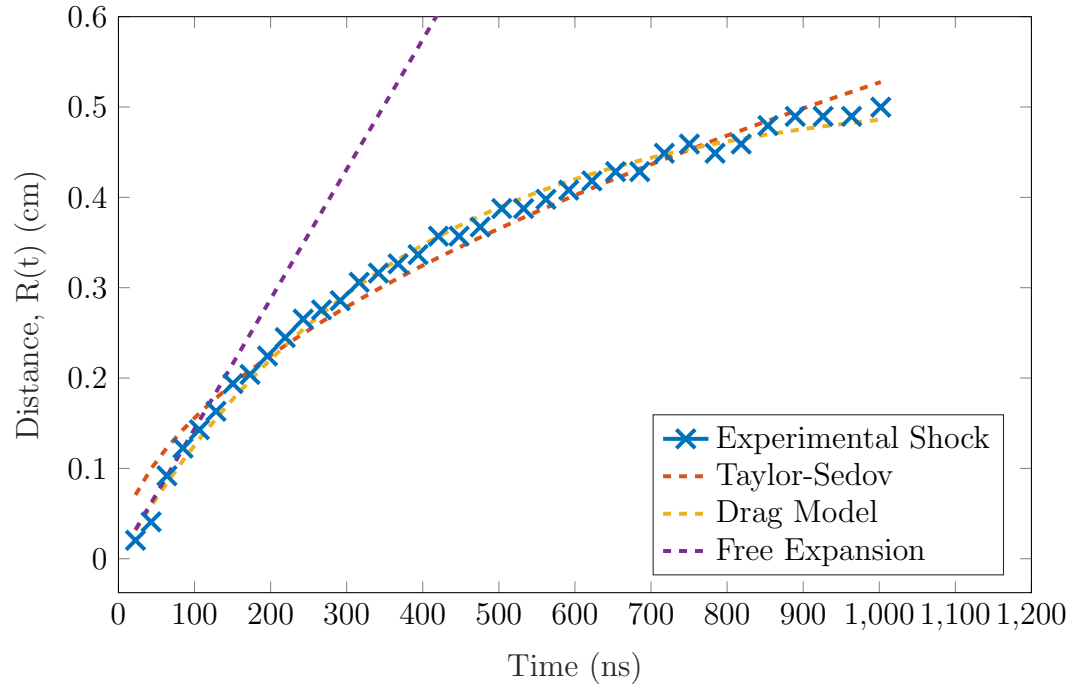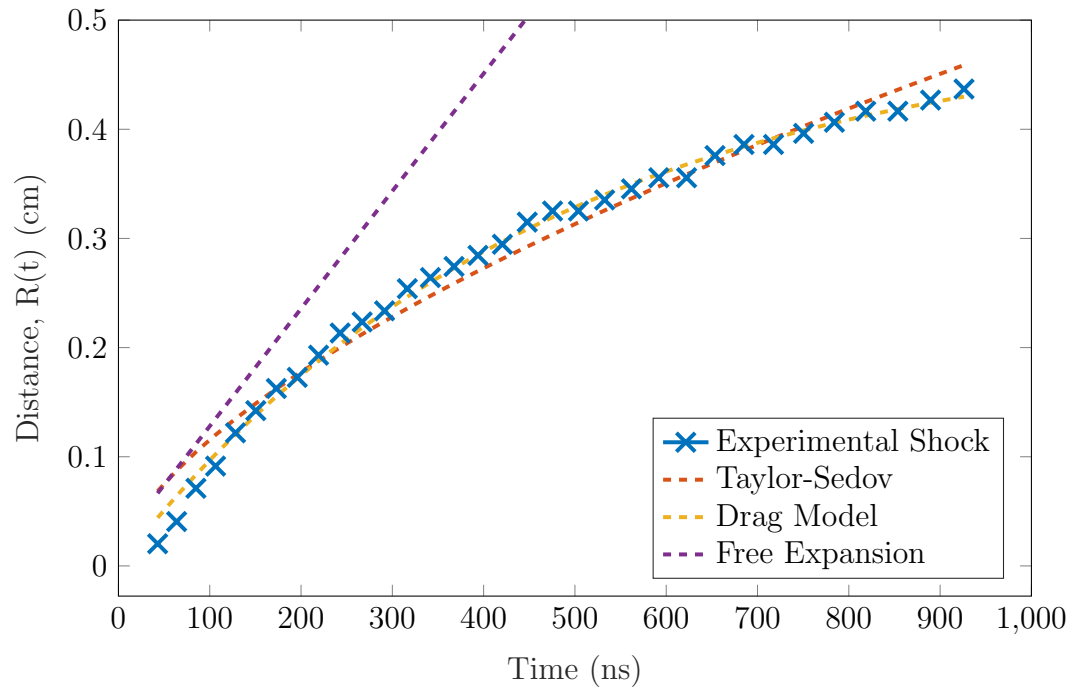
72

Figure 45. The shock front propagation is shown for an air background pressure of 10 Torr with a 830 nm filter on the ICCD array.

Figure 46. The shock front propagation is shown for an argon background pressure of 10 Torr with no filter on the ICCD array.

73

Figure 47. The shock front propagation is shown for an argon background pressure of 10 Torr with a 520 nm filter on the ICCD array.

Figure 48. The shock front propagation is shown for an argon background pressure of 10 Torr with a 830 nm filter on the ICCD array.
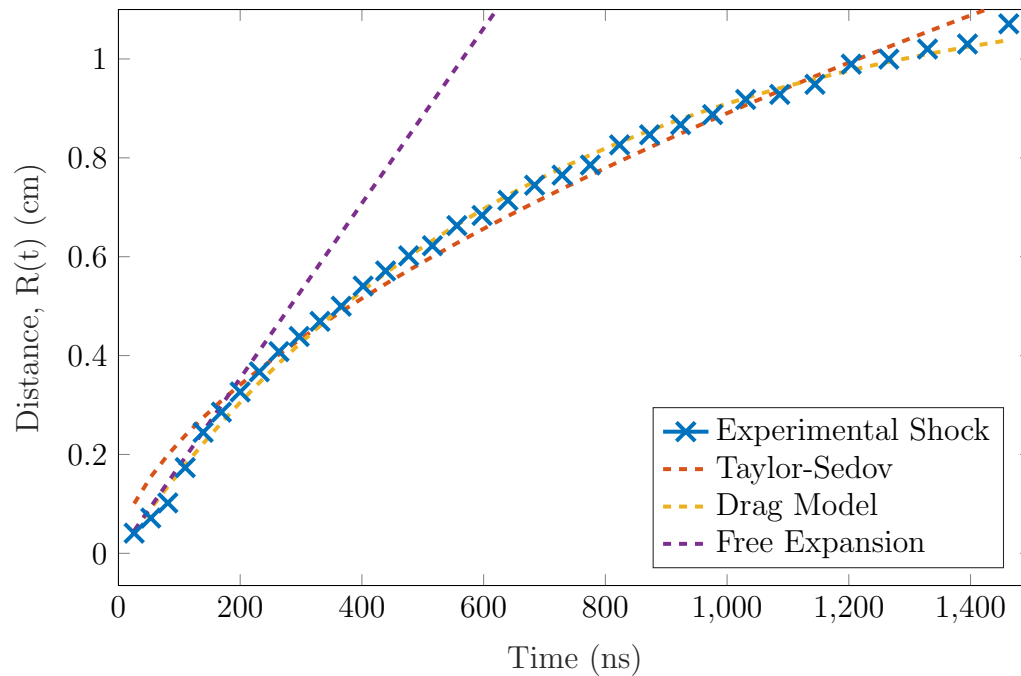
74

Figure 49. The shock front propagation is shown for a helium background pressure of 10 Torr with no filter on the ICCD array.
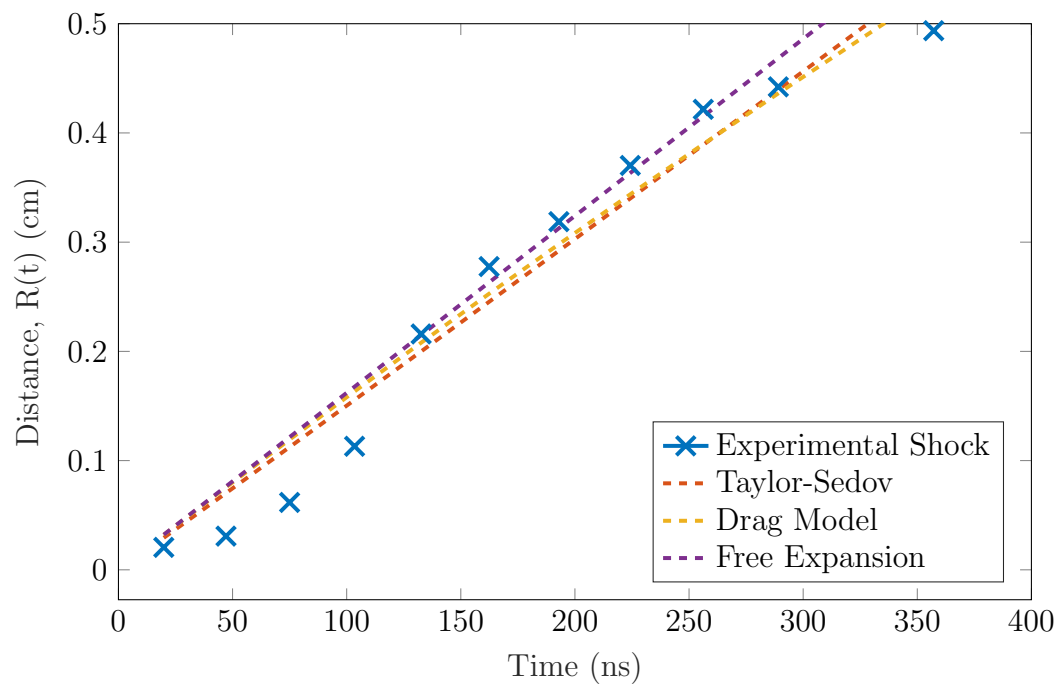

Figure 50. The shock front propagation is shown for a helium background pressure of 10 Torr with a 520 nm filter on the ICCD array.
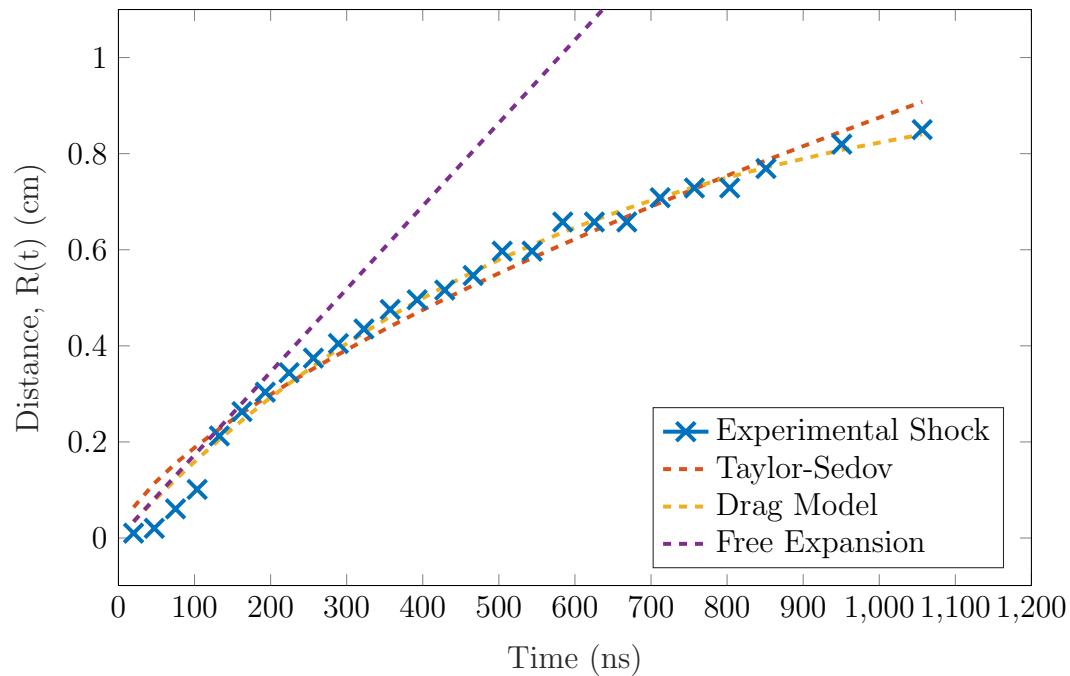
75

Figure 51. The shock front propagation is shown for a helium background pressure of 10 Torr with a 830 nm filter on the ICCD array.

Figure 52. The shock front propagation is shown for a nitrogen background pressure of 1 Torr with no filter on the ICCD array.

Figure 53. The shock front propagation is shown for a nitrogen background pressure of 10 Torr with no filter on the ICCD array.
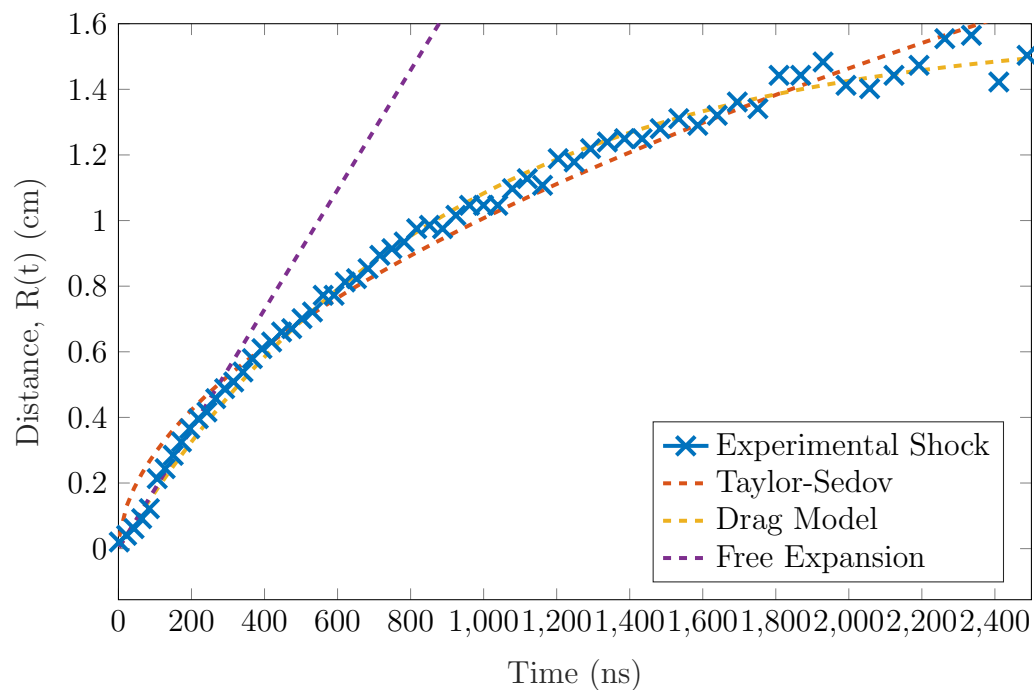

Figure 54. The shock front propagation is shown for a nitrogen background pressure of 10 Torr with a 520 nm filter on the ICCD array.
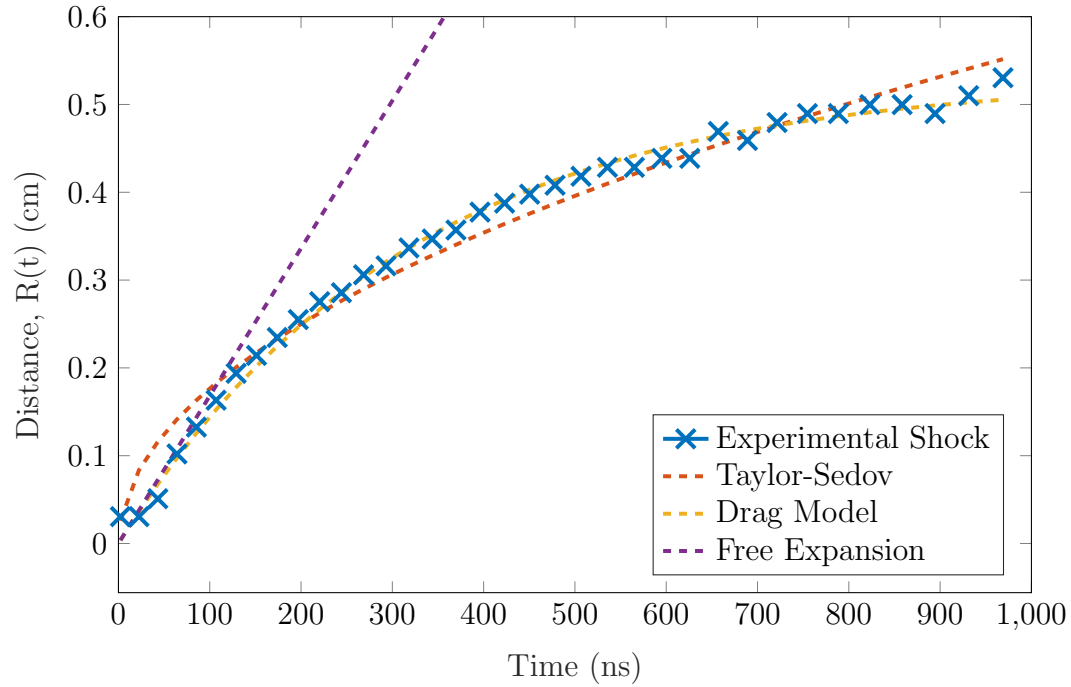
Figure 55. The shock front propagation is shown for a nitrogen background pressure of 10 Torr with a 830 nm filter on the ICCD array.
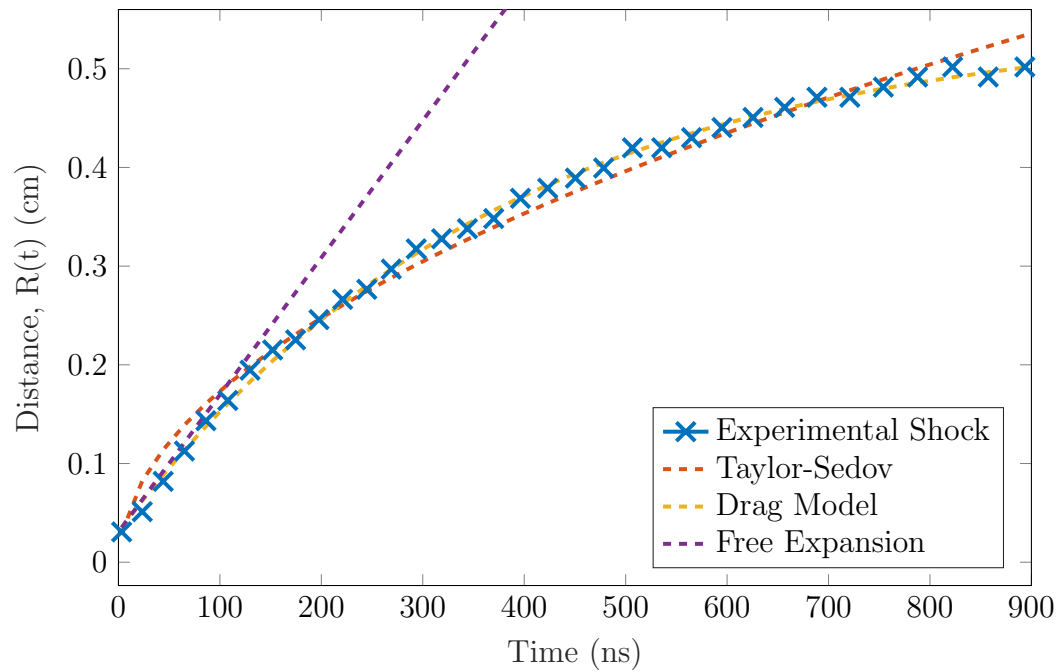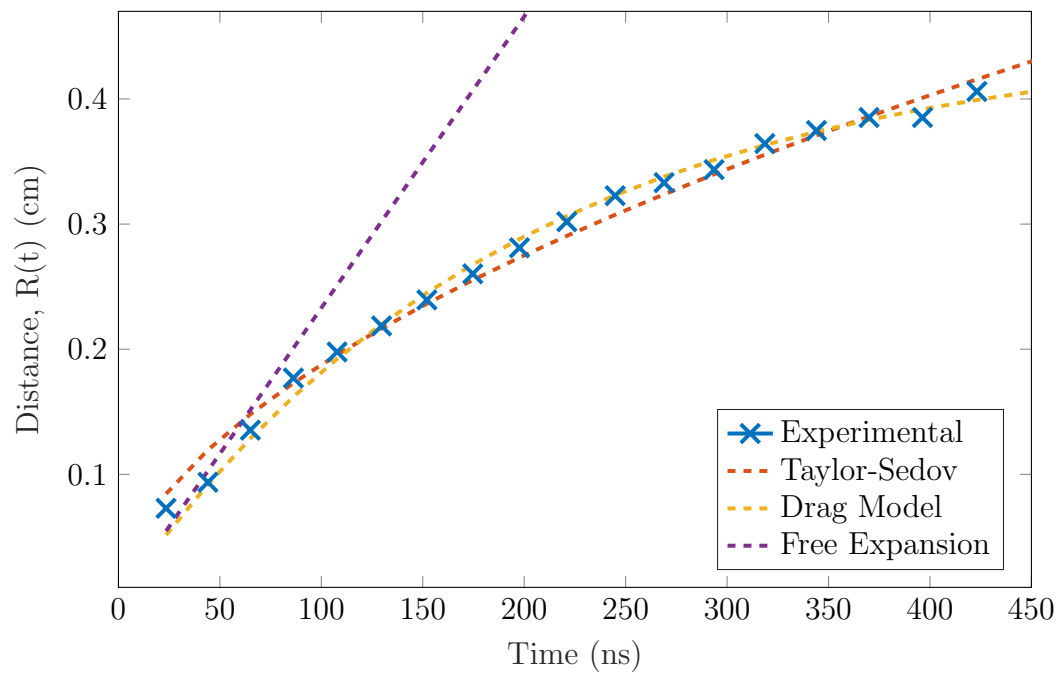

Figure 56. The shock front propagation is shown in a vacuum with no filter on the ICCD array.

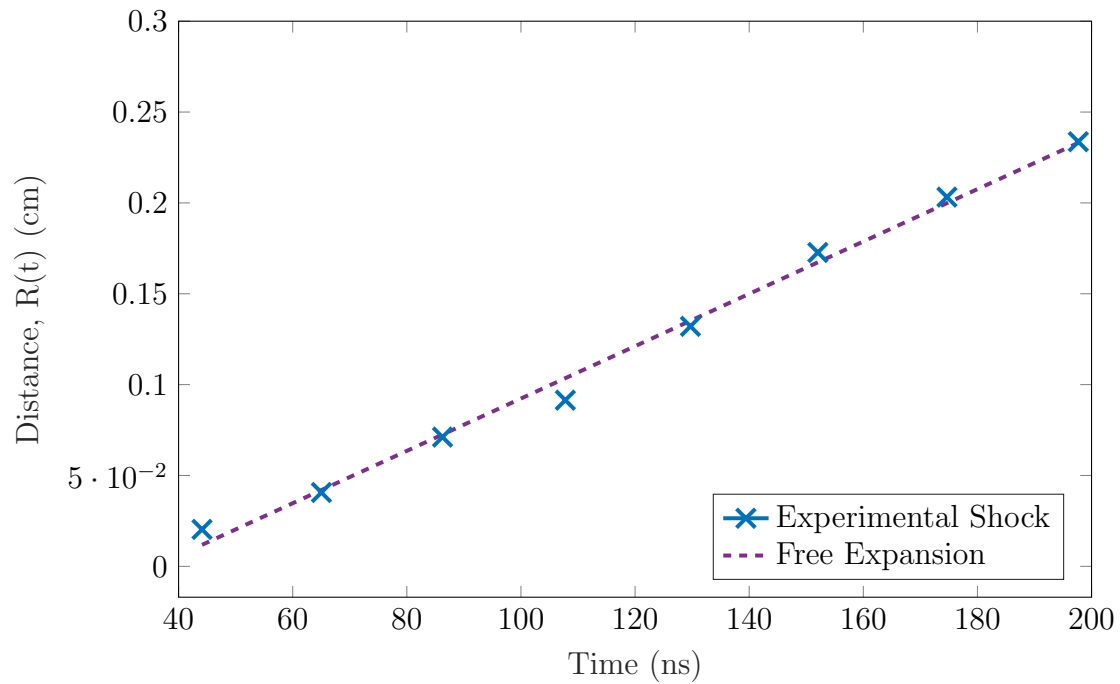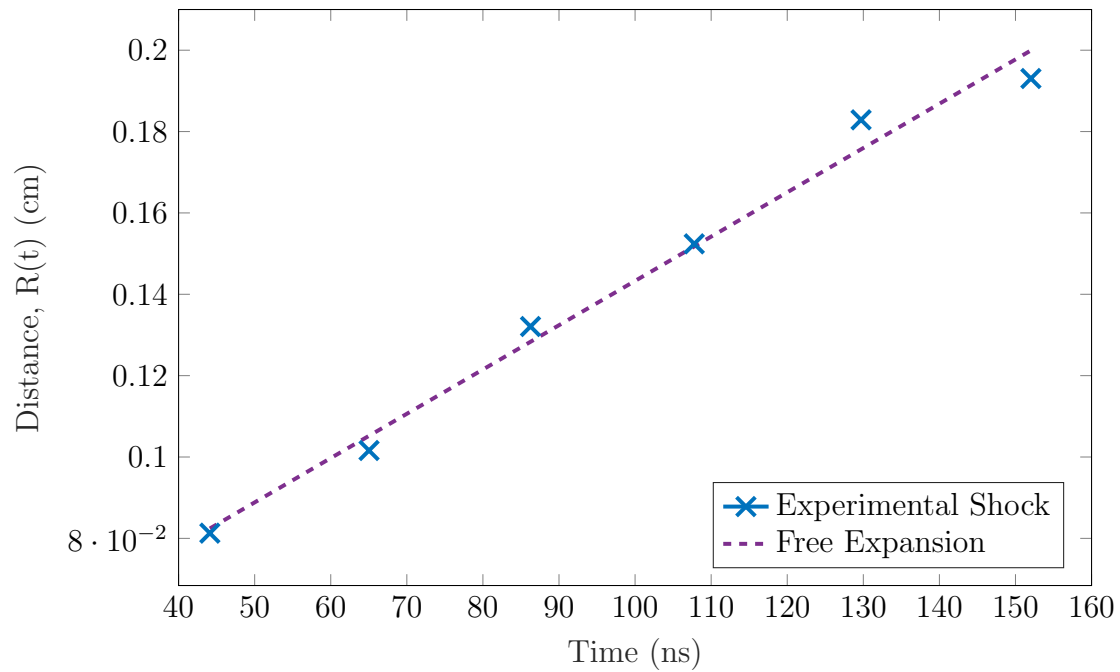**Figure 57. The shock front propagation is shown in a vacuum with a 520 nm filter on the ICCD array.**
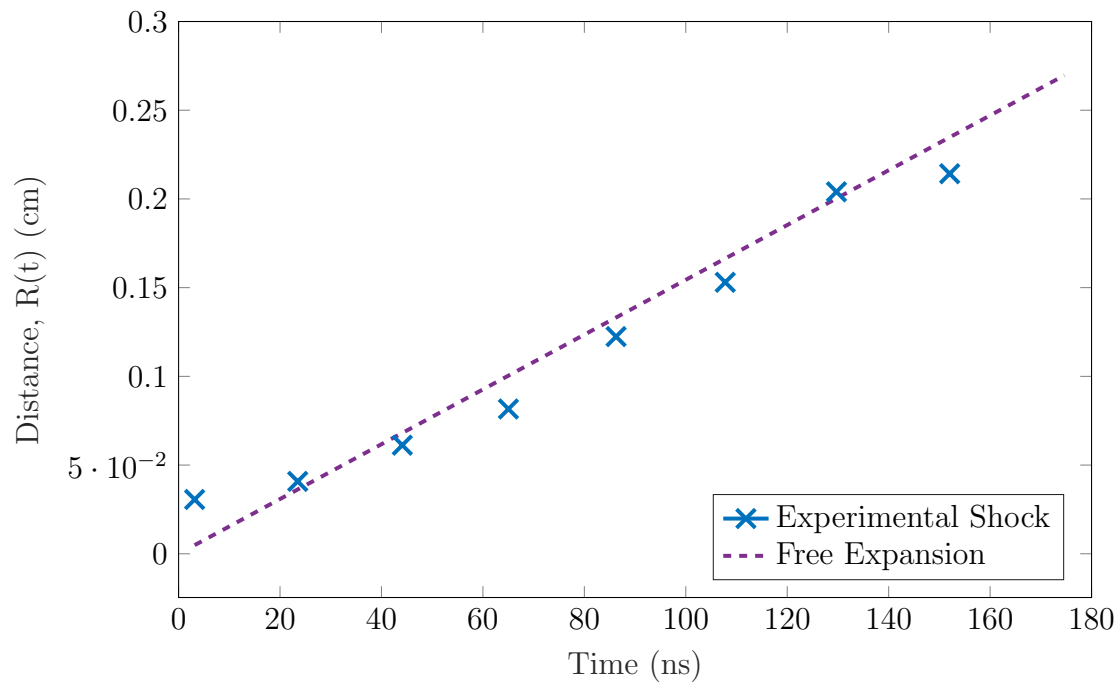

Figure 58. The shock front propagation is shown in a vacuum with a 830 nm filter on the ICCD array.

Bibliography

1. W. Liu, X. Chang, X. Zhang, and Y. Zhang, "Progressive damage analysis of carbon/epoxy laminates under couple laser and mechanical loading," *Results in Physics*, vol. 7, pp. 995 – 1005, 2017. [Online]. Available: http://www.sciencedirect.com/science/article/pii/S2211379716301048

2. S. W. Lewis, C. M. James, R. G. Morgan, T. J. McIntyre, C. R. Alba, and R. B. Greendyke, "Carbon ablative shock-layer radiation with high surface temperatures," *Journal of Thermophysics and Heat Transfer*, vol. 31, no. 1, pp. 193–204, 2017. [Online]. Available: https://doi.org/10.2514/1.T4902

3. R. K. Singh and J. Narayan, "Pulsed-laser evaporation technique for deposition of thin films: Physics and theoretical model," *Phys. Rev. B*, vol. 41, pp. 8843–8859, May 1990.

4. F. J. Gordillo-Vázquez and J. M. Albella, "Distinct nonequilibrium plasma chemistry of c2 affecting the synthesis of nanodiamond thin films from $C_2H_2(1\%)$/ H_2/Ar-rich plasmas," *Journal of Applied Physics*, vol. 94, no. 9, pp. 6085–6090, 2003. [Online]. Available: https://doi.org/10.1063/1.1617362

5. T. Ikegami, F. Nakanishi, M. Uchiyama, and K. Ebihara, "Optical measurement in carbon nanotubes formation by pulsed laser ablation," *Thin Solid Films*, vol. 457, no. 1, pp. 7 – 11, 2004, the 16th Symposium on Plasma Science for Materials (SPSM-16). [Online]. Available: http://www.sciencedirect.com/science/article/pii/S0040609003019126

6. A. A. Puretzky, D. B. Geohegan, X. Fan, and S. J. Pennycook, "Dynamics of single-wall carbon nanotube synthesis by laser vaporization," *Applied Physics A*, vol. 70, no. 2, pp. 153–160, February 2000.

7. S. Bhattacharyya, O. Auciello, J. Birrell, J. A. Carlisle, L. A. Curtiss, A. N. Goyette, D. M. Gruen, A. R. Krauss, J. Schlueter, A. Sumant, and P. Zapol, "Synthesis and characterization of highly-conducting nitrogen-doped ultrananocrystalline diamond films," *Applied Physics Letters*, vol. 79, no. 10, pp. 1441–1443, 2001. [Online]. Available: https://doi.org/10.1063/1.1400761

8. S. Sinha, "Nanosecond laser ablation of graphite: A thermal model based simulation," *Journal of Laser Applications*, vol. 30, no. 1, p. 012008, 2018. [Online]. Available: https://doi.org/10.2351/1.5021520

9. C. Sawyer, K. Iyer, X. Zhu, M. Kelly, D. Luke, and D. Amdahl, "Two-dimensional laser-induced thermal ablation modeling with integrated melt flow and vapor dynamics," *Journal of Laser Applications*, vol. 29, no. 2, p. 022212, 2017. [Online]. Available: https://doi.org/10.2351/1.4983825

10. A. Einstein, "Zur Quantentheorie der Strahlung," *Physikalische Zeitschrift*, vol. 18, pp. 121–128, Jan 1917.

11. T. H. MAIMAN, "Stimulated optical radiation in ruby," *Nature*, vol. 187, no. 4736, pp. 493–494, 1960. [Online]. Available: https://doi.org/10.1038/187493a0

12. J. Marczak, "Surface cleaning of artwork by UV, VIS, and IR pulse laser radiation," in *Laser Techniques and Systems in Art Conservation*, R. Salimbeni, Ed., vol. 4402, International Society for Optics and Photonics. SPIE, 2001, pp. 202 – 209. [Online]. Available: https://doi.org/10.1117/12.445663

13. S. Siano and R. Salimbeni, "Advances in laser cleaning of artwork and objects of historical interest: The optimized pulse duration approach," *Accounts of Chemical Research*, vol. 43, no. 6, pp. 739–750, 06 2010. [Online]. Available: https://doi.org/10.1021/ar900190f

14. R. Kaufmann and R. Hibst, "Pulsed erbium:yag laser ablation in cutaneous surgery," *Lasers in Surgery and Medicine*, vol. 19, no. 3, pp. 324–330, 1996. [Online]. Available: https://onlinelibrary.wiley.com/doi/abs/10.1002/%28SICI%291096-9101%281996%2919%3A3%3C324%3A%3AAID-LSM7%3E3.0.CO%3B2-U

15. A. Vogel and V. Venugopalan, "Mechanisms of pulsed laser ablation of biological tissues," *Chemical Reviews*, vol. 103, no. 2, pp. 577–644, 02 2003. [Online]. Available: https://doi.org/10.1021/cr010379n

16. J. Meister, R. Franzen, K. Gavenis, M. Zaum, S. Stanzel, N. Gutknecht, and B. Schmidt-Rohlfing, "Ablation of articular cartilage with an erbium:yag laser: An ex vivo study using porcine models under real conditions—ablation measurement and histological examination," *Lasers in Surgery and Medicine*, vol. 41, no. 9, pp. 674–685, 2009. [Online]. Available: https://onlinelibrary.wiley.com/doi/abs/10.1002/lsm.20848

17. X. Liu, D. Du, and G. Mourou, "Laser ablation and micromachining with ultrashort laser pulses," *IEEE Journal of Quantum Electronics*, vol. 33, no. 10, pp. 1706–1716, 1997.

18. A. Ojeda-G-P, C. W. Schneider, M. Döbeli, T. Lippert, and A. Wokaun, "Plasma plume dynamics, rebound, and recoating of the ablation target in pulsed laser deposition," *Journal of Applied Physics*, vol. 121, no. 13, p. 135306, 2017. [Online]. Available: https://doi.org/10.1063/1.4979780

19. J. D. Jackson, *Classical Electrodynamics, 3rd Edition*, 3rd ed. Wiley, 1998.

20. T. Smausz, B. Kondász, T. Gera, T. Ajtai, N. Utry, M. Pintér, G. Kiss-Albert, J. Budai, Z. Bozóki, G. Szabó, and B. Hopp, "Determination of uv–visible–nir

absorption coefficient of graphite bulk using direct and indirect methods," *Applied Physics A*, vol. 123, no. 10, p. 633, Sept 2017.

21. N. Bloembergen, "Fundamentals of laser-solid interactions," *AIP Conference Proceedings*, vol. 50, no. 1, pp. 1–9, 1979. [Online]. Available: https://aip.scitation.org/doi/abs/10.1063/1.31659

22. (2020). [Online]. Available: https://www.lesker.com/newweb/deposition_materials/depositionmaterials_sputtertargets_1.cfm?pgid=car1

23. A. Butland and R. Maddison, "The specific heat of graphite: An evaluation of measurements," *Journal of Nuclear Materials*, vol. 49, no. 1, pp. 45 – 56, 1973.

24. W. Bauer, "Laser heating of graphite and pulsed laser ablation of titanium and aluminum," Ph.D. dissertation, Air Force Institute of Technology, August 2017.

25. A. A. Ionin, S. I. Kudryashov, and L. V. Seleznev, "Near-critical phase explosion promoting breakdown plasma ignition during laser ablation of graphite," *Phys. Rev. E*, vol. 82, p. 016404, Jul 2010.

26. G. Glockler, "The heat of sublimation of graphite and the composition of carbon vapor," *The Journal of Chemical Physics*, vol. 22, no. 2, pp. 159–161, December 1954.

27. J. Abrahamson, "Graphite sublimation temperatures, carbon arcs and crystallite erosion," *Carbon*, vol. 12, no. 2, pp. 111 – 141, 1974.

28. S. S. Harilal, G. V. Miloshevsky, P. K. Diwakar, N. L. LaHaye, and A. Hassanein, "Experimental and computational study of complex shockwave dynamics in laser ablation plumes in argon atmosphere," *Physics of Plasmas*, vol. 19, no. 8, p. 083504, 2012.

29. W. Bauer, G. P. Perram, and T. Haugan, "Comparison of plume dynamics for laser ablated metals: Al and Ti," *Journal of Applied Physics*, vol. 123, no. 9, p. 095304, 2018. [Online]. Available: https://doi.org/10.1063/1.5011028

30. R. F. Wood, J. N. Leboeuf, D. B. Geohegan, A. A. Puretzky, and K. R. Chen, "Dynamics of plume propagation and splitting during pulsed-laser ablation of si in he and ar," *Physical Review B*, vol. 58, no. 3, pp. 1533–1543, July 1998.

31. D. B. Geohegan and A. A. Puretzky, "Dynamics of laser ablation plume penetration through low pressure background gases," *Applied Physics Letters*, vol. 67, no. 2, pp. 197–199, 1995. [Online]. Available: https://doi.org/10.1063/1.114665

32. P. F. Bernath, *Spectra of Atoms and Molecules*, 3rd ed. Oxford University Press, 2016.

33. G. Herzberg, *Spectra of Diatomic Molecules*, 2nd ed. New York: Litton, 1950.

34. J. S. A. Brooke, "Line lists including intensities for diatomic molecules of astronomical interest and remote sensing measurements of greenhouse gases," Ph.D. dissertation, University of York, September 2014.

35. G. M. Fuge, M. N. R. Ashfold, and S. J. Henley, "Studies of the plume emission during the femtosecond and nanosecond ablation of graphite in nitrogen," *Journal of Applied Physics*, vol. 99, no. 1, p. 014309, 2006. [Online]. Available: https://doi.org/10.1063/1.2158500

36. S. S. Harilal, R. C. Issac, C. V. Bindhu, V. P. N. Nampoori, and C. P. G. Vallabhan, "Temporal and spatial evolution of C_2 in laser induced plasma from graphite target," *Journal of Applied Physics*, vol. 80, no. 6, pp. 3561–3565, 1996. [Online]. Available: https://doi.org/10.1063/1.363229

84

37. ——, "Optical emission studies of species in laser-produced plasma from carbon," *Journal of Physics D: Applied Physics*, vol. 30, no. 12, pp. 1703–1709, Jun 1997. [Online]. Available: https://doi.org/10.1088%2F0022-3727%2F30%2F12%2F003

38. R. Thareja, R. Dwivedi, and K. Ebihara, "Interaction of ambient nitrogen gas and laser ablated carbon plume: Formation of CN," *Nuclear Instruments and Methods in Physics Research Section B: Beam Interactions with Materials and Atoms*, vol. 192, no. 3, pp. 301–310, 2002. [Online]. Available: http://www.sciencedirect.com/science/article/pii/S0168583X02004767

39. W. Swan, "On the prismatic spectra of the flames of compounds of carbon and hydrogen," *Transactions of the Royal Society of Edinburgh*, vol. 21, no. 3, pp. 411–429, 1857.

40. J. S. Brooke, P. F. Bernath, T. W. Schmidt, and G. B. Bacskay, "Line strengths and updated molecular constants for the C_2 swan system," *Journal of Quantitative Spectroscopy and Radiative Transfer*, vol. 124, pp. 11 – 20, 2013. [Online]. Available: http://www.sciencedirect.com/science/article/pii/S0022407313000800

41. D. L. Lambert and A. C. Danks, "High-resolution spectra of C2 Swan bands from comet West 1976 VI," *The Astrophysical Journal*, vol. 268, pp. 428–446, May 1983.

42. A. Schadee, "An upper limit of the swan band intensity in a sunspot spectrum," *Solar Physics*, vol. 15, no. 2, pp. 345–348, 1970. [Online]. Available: https://doi.org/10.1007/BF00151839

43. B. P. Hema, G. Pandey, and D. L. Lambert, "THE GALACTIC r CORONAE BOREALIS STARS: THE c2swan BANDS, THE CARBON PROBLEM, AND

THE12c/13c RATIO," *The Astrophysical Journal*, vol. 747, no. 2, p. 102, feb 2012. [Online]. Available: https://doi.org/10.1088%2F0004-637x%2F747%2F2%2F102

44. H. Izumiura, "Circumstellar C_2 Swan band in optical carbon stars," *Astronomical Herald*, vol. 96, no. 6, pp. 328–339, Jun 2003.

45. P. F. Bernath, "Molecular astronomy of cool stars and sub-stellar objects," *International Reviews in Physical Chemistry*, vol. 28, no. 4, pp. 681–709, 2009. [Online]. Available: https://doi.org/10.1080/01442350903292442

46. S. Arepalli, P. Nikolaev, W. Holmes, and C. D. Scott, "Diagnostics of laser-produced plume under carbon nanotube growth conditions," *Applied Physics A*, vol. 70, no. 2, pp. 125–133, 2000. [Online]. Available: https://doi.org/10.1007/s003390050024

47. S. Acquaviva and M. L. D. Giorgi, "High-resolution investigations of c2and CN optical emissions in laser-induced plasmas during graphite ablation," *Journal of Physics B: Atomic, Molecular and Optical Physics*, vol. 35, no. 4, pp. 795–806, feb 2002. [Online]. Available: https://doi.org/10.1088%2F0953-4075%2F35%2F4%2F304

48. R. G. W. Norrish, G. Porter, and B. A. Thrush, "Studies of the explosive combustion of hydrocarbons by kinetic spectroscopy i. free radical absorption spectra in acetylene combustion," *Proceedings of the Royal Society A*, vol. 216, no. 1125, pp. 165–183, January 1953.

49. G. P. Smith, C. Park, J. Schneiderman, and J. Luque, "C2 swan band laser-induced fluorescence and chemiluminescence in low-pressure hydrocarbon flames," *Combustion and Flame*, vol. 141, no. 1, pp. 66 – 77, 2005. [Online]. Available: http://www.sciencedirect.com/science/article/pii/S0010218005000064

50. S. Keshav, Y. G. Utkin, M. Bao, A. Rich, J. W. Rich, and I. V. Adamovich, "Studies of chemi-ionization and chemiluminescence in supersonic flows of combustion products," *Journal of Thermophysics and Heat Transfer*, vol. 22, no. 2, pp. 157–167, 2008. [Online]. Available: https://doi.org/10.2514/1.30822

51. A. Tanabashi, T. Hirao, T. Amano, and P. Bernath, "The swan system of C_2: A global analysis of fourier transform emission spectra," *The Astrophysical Journal Supplement Series*, vol. 169, no. 2, pp. 472–484, April 2007.

52. J. S. A. Brooke, R. S. Ram, C. M. Western, G. Li, D. W. Schwenke, and P. F. Bernath, "Einstein a coefficients and oscillator strengths for the $A^2\Pi - X^2\Sigma^+$(red) and $B^2\Sigma^+ - X^2\Sigma^+$(violet) systems and rovibrational transitions in the $X^2\Sigma^+$ state of CN," *The Astrophysical Journal Supplement Series*, vol. 210, no. 2, p. 23, jan 2014. [Online]. Available: https://doi.org/10.1088%2F0067-0049%2F210%2F2%2F23

53. H. S. Park, S. H. Nam, and S. M. Park, "Time-resolved optical emission studies on the laser ablation of a graphite target: The effects of ambient gases," *Journal of Applied Physics*, vol. 97, no. 11, p. 113103, 2005. [Online]. Available: https://doi.org/10.1063/1.1925336

54. C. Vivien, J. Hermann, A. Perrone, C. Boulmer-Leborgne, and A. Luches, "A study of molecule formation during laser ablation of graphite in low-pressure nitrogen," *Journal of Physics D: Applied Physics*, vol. 31, no. 10, pp. 1263–1272, may 1998. [Online]. Available: https://doi.org/10.1088%2F0022-3727%2F31%2F10%2F019

55. S. Wee and S. M. Park, "Reactive laser ablation of graphite in a nitrogen atmosphere: optical emission studies," *Optics Communications*,

vol. 165, no. 4, pp. 199 – 205, 1999. [Online]. Available: http://www.sciencedirect.com/science/article/pii/S0030401899002175

56. W. Bauer, C. Fox, R. Gosse, and G. Perram, "Visible emission from C_2 and CN during cw laser-irradiated graphite," *Optical Engineering*, vol. 56, no. 1, pp. 1 – 10 – 10, 2016. [Online]. Available: https://doi.org/10.1117/1.OE.56.1.011017

57. C. Sneden, "The nitrogen abundance of the very metal-poor star HD 122563." *The Astrophysical Journal*, vol. 184, p. 839, Sep 1973.

58. C. Sneden and D. L. Lambert, "Isotopic Abundance Ratios for Carbon and Nitrogen in Nova Herculis 1934," *Monthly Notices of the Royal Astronomical Society*, vol. 170, no. 3, pp. 533–540, 03 1975. [Online]. Available: https://doi.org/10.1093/mnras/170.3.533

59. C. Sneden, S. Lucatello, R. S. Ram, J. S. A. Brooke, and P. Bernath, "LINE LISTS FOR THE $A^2\Pi$-$X^2\Sigma^+$(RED) AND $B^2\Sigma^+$-$X^2\Sigma$ (VIOLET) SYSTEMS OF CN,$^{13}c^{14}n$, AND $^{12}c^{15}n$, AND APPLICATION TO ASTRONOMICAL SPECTRA," *The Astrophysical Journal Supplement Series*, vol. 214, no. 2, p. 26, oct 2014. [Online]. Available: https://doi.org/10.1088%2F0067-0049%2F214%2F2%2F26

60. S. Leach, "Cn spectroscopy and cosmic background radiation measurements," *Canadian Journal of Chemistry*, vol. 82, no. 6, pp. 730–739, 2004. [Online]. Available: https://doi.org/10.1139/v04-036

61. ——, "Why cobe and cn spectroscopy cosmic background radiation temperature measurements differ, and a remedy," *Monthly Notices of the Royal Astronomical Society*, vol. 421, no. 2, pp. 1325–1330, 2012. [Online]. Available: https://onlinelibrary.wiley.com/doi/abs/10.1111/j.1365-2966.2011.20390.x

88

62. H. F. Schaefer and T. G. Heil, "Electronic structures and potential energy curves for the low-lying states of the cn radical," *The Journal of Chemical Physics*, vol. 54, no. 6, pp. 2573–2580, 1971. [Online]. Available: https://doi.org/10.1063/1.1675214

63. E. E. Whiting and R. W. Nicholls, "Reinvestigation of Rotational-Line Intensity Factors in Diatomic Spectra," *The Astrophysical Journal Supplement Series*, vol. 27, p. 1, Jan 1974.

64. C. M. Western, "PGOPHER: A program for simulating rotational, vibrational and electronic spectra," *Journal of Quantitative Spectroscopy and Radiative Transfer*, vol. 186, pp. 221 – 242, 2017.

65. J. H. Callomon and A. C. Gilby, "New observations on the Swan bands of C_2," *Canadian Journal of Physics*, vol. 41, p. 995, Jan 1963.

66. K. Saito, T. Sakka, and Y. H. Ogata, "Rotational spectra and temperature evaluation of C_2 molecules produced by pulsed laser irradiation to a graphite–water interface," *Journal of Applied Physics*, vol. 94, no. 9, pp. 5530–5536, 2003. [Online]. Available: https://doi.org/10.1063/1.1614431

67. J. R. Taylor, *An Introduction to Error Analysis: The Study of Uncertainties in physical measurements*, 2nd ed. Sausalito, CA: University Science Books, 1997.

REPORT DOCUMENTATION PAGE

Form Approved
OMB No. 0704-0188

1. REPORT DATE *(DD-MM-YYYY)*	2. REPORT TYPE	3. DATES COVERED *(From - To)*
03/26/2020	Master's Thesis	Aug 2018-Mar 2020

4. TITLE AND SUBTITLE

CN and C2 Spectroscopy on the Pulsed Ablation of Graphite in the Visible Spectrum

5a. CONTRACT NUMBER

5b. GRANT NUMBER

5c. PROGRAM ELEMENT NUMBER

6. AUTHOR(S)

Pierce, Brandon A, 2d Lt, USAF

5d. PROJECT NUMBER

5e. TASK NUMBER

5f. WORK UNIT NUMBER

7. PERFORMING ORGANIZATION NAME(S) AND ADDRESS(ES)

Air Force Institute of Technology
Graduate School of Engineering and Management (AFIT/EN)
2950 Hobson Way
Wright-Patterson AFB OH 45433-7765

8. PERFORMING ORGANIZATION REPORT NUMBER

AFIT-ENP-MS-20-M-111

9. SPONSORING/MONITORING AGENCY NAME(S) AND ADDRESS(ES)

Air Force Research Lab, Aerospace Systems
1950 5th St Bldg 18
Wright Patterson AFB, OH 45433

10. SPONSOR/MONITOR'S ACRONYM(S)

AFRL/RQQM

11. SPONSOR/MONITOR'S REPORT NUMBER(S)

12. DISTRIBUTION/AVAILABILITY STATEMENT

Distribution Statement A. Approved for Public Release; Distribution Unlimited

13. SUPPLEMENTARY NOTES

This work is declared a work of the U.S. Government and is not subject to copyright protection in the United States.

14. ABSTRACT

An experimental study was conducted on the nanosecond pulsed laser ablation of graphite using a KrF laser at a fluence of 3.8 J/cm^2 in Air, Ar, He, and N2. Optical emissions spectroscopy revealed the C2 Swan sequences and the CN Violet sequences. A spectroscopic model was developed to extract the molecular rotational and vibrational temperatures of each excited species for t=0.5-10 microseconds after laser irradiation. The rovibrational temperatures were found to vary with background gas for the CN Violet; however, only the vibrational temperature varied between He and the other background gases for C2 Swan. The rotational and vibrational temperatures were not in equilibrium for both the C2 Swan and CN Violet.

15. SUBJECT TERMS

Optical emissions spectroscopy, laser, pulsed ablation, molecular nitrogen, molecular carbon.

16. SECURITY CLASSIFICATION OF:			17. LIMITATION OF ABSTRACT	18. NUMBER OF PAGES	19a. NAME OF RESPONSIBLE PERSON
a. REPORT	b. ABSTRACT	c. THIS PAGE			Glen Perram
U	U	U	UU	102	19b. TELEPHONE NUMBER *(Include area code)* (937)255-3636x4504

Standard Form 298 (Rev. 8/98)
Prescribed by ANSI Std. Z39.18
www.manaraa.com